2016

Fault Diagnosis and Fault-Tolerant Control of Quadrotor UAVs

Remus C. Avram
Wright State University

FAULT DIAGNOSIS AND FAULT-TOLERANT CONTROL OF QUADROTOR UAVS

A dissertation submitted in partial fulfillment of the
requirements for the degree of
Doctor of Philosophy

By

REMUS CĂLIN AVRAM
B.S., University of Texas at San Antonio, USA, 2009
M.S., Wright State University, USA, 2011

2016
Wright State University

WRIGHT STATE UNIVERSITY

GRADUATE SCHOOL

April 29, 2016

I HEREBY RECOMMEND THAT THE DISSERTATION PREPARED UNDER MY SUPERVISION BY REMUS C AVRAM, ENTITLED FAULT DIAGNOSIS AND FAULT-TOLERANT CONTROL OF QUADROTOR UAVS BE ACCEPTED IN PARTIAL FULFILLMENT OF THE REQUIREMENTS FOR THE DEGREE OF Doctor of Philosophy.

Xiaodong Zhang, Ph.D.
Dissertation Director

Frank W. Ciarallo, Ph.D.
Director, Ph.D. in
Engineering Program

Robert E. W. Fyffe, Ph.D.
Vice President for Research and
Dean of the Graduate School

Committee on
Final Examination

Xiaodong Zhang, Ph.D.

Kuldip Rattan, Ph.D.

Marian Kazimierczuk, Ph. D.

Jonathan Muse, Ph. D.

Xuefu Zhou, Ph.D.

ABSTRACT

Avram, Remus Călin Ph.D., Engineering Ph.D. program, Wright State University, 2016, Fault Diagnosis and Fault-Tolerant Control of Quadrotor UAVs.

Quadrotors represent a special class of Unmanned Aerial Vehicles (UAVs) and have attracted significant attention in recent years due to their potential in various military and civilian applications. However, due to their intrinsic fabrication process and component damage, quadrotors are prone to various type of faults. This dissertation presents the design, analysis, and experimental implementation of fault diagnosis, fault-tolerant control, and controller verification methods to achieve safety assurance and trusted autonomy of quadrotor UAVs. First, the issue of sensor faults is investigated under two different scenarios: (1) the case when all Euler angles are available for measurement; (2) the case when roll and pitch angles are not measurable and need to be estimated. Nonlinear adaptive estimators are designed to provide possible simultaneous accelerometer and gyroscope fault detection, isolation, and bias estimation. Next, the issue of fault-tolerant control of quadrotor UAV in the presence of actuator faults is considered. First, the design of an integrated fault diagnosis and accommodation scheme is investigated. Nonlinear adaptive thresholds are designed to improve the robustness of the fault detection and isolation algorithm. The fault diagnostic information is used for accommodating the effect of the faults. Second, a nonlinear adaptive fault-tolerant altitude and attitude controller is developed to automatically stabilize and recover tracking performance of the quadrotor, even in the presence of possible multiple simultaneous actuator faults. Compared with the first approach, the adaptive control framework is able to automatically accommodate the effects of actuator faults without the need of a fault diagnosis mechanism. Finally, a run-time assurance architecture is investigated for the verification and validation of the adaptive fault-tolerant altitude attitude controller. The algorithms are presented with a rigorous framework aimed at characterizing their performance properties. The above algorithms are implemented and evaluated using a

real-time indoor quadrotor test environment. Experimental flight test results are shown to illustrate the effectiveness of the proposed methods.

TABLE OF CONTENTS

Page

LIST OF FIGURES

ACKNOWLEDGEMENTS

First and foremost, I would like to express my deepest gratitude to my advisor Dr. Xiaodong Zhang. I am truly humbled and forever thankful for your constant guidance, encouragement, for believing in me, and for introducing me to the wonderful field of fault diagnosis.

I wish to thank Dr. Jonathan Muse for his valuable and insightful thoughts. Your guidance has not only accelerated my research process, but has provided me with a deeper overall understanding and appreciation for control systems.

My sincere thanks also go to my dissertation committee members: Dr. Kuldip Rattan, Dr. Marian Kazimierczuk, Dr. Xuefu Zhou. Thank you for your time and most valuable feedback.

I am forever grateful for my parents, who have incessantly inspired me to aim for higher goals. Vă mulțumesc și vă iubesc!

Last, but not least, I would like to thank my beautiful, forever patient wife. None of this would have been possible without your love, kindness and comfort. Thank you!

I. INTRODUCTION

Unmanned Aerial Vehicles (UAVs) have attracted significant attentions in recent years due to their potentials in various military and civilian applications, including security patrol, search and rescue in hazardous environment, surveillance and classification, attack and rendezvous [1]. In addition, compared with manned systems, the reductions in operations and support costs for unmanned vehicles offer the advantage for life cycle cost savings [2]. The potential capabilities offered by unmanned vehicles have been well recognized and continue to expand. For instance, as reported in Teal Group's 2013 market study [3], Unmanned Aerial Vehicles continue to be the most dynamic growth sector of the world aerospace industry this decade, and the UAV spending will more than double over the next decade from current worldwide UAV expenditures of $5.2 billion annually to $11.6 billion, totaling just over $89 billion in the next ten years.

In manned systems, the human operator functions as the central integrator of the on-board systems to achieve their operational capabilities. Due to the requirement of autonomous operations without a human operator, autonomous control of UAVs is much more challenging and UAVs currently suffer significantly more mishaps when compared to their manned counterparts [2, 4]. Repeatedly failed missions detract from the willingness to use unmanned systems. As acknowledged by The Office of the Secretary of Defense in its UAVs Roadmap [2, 4], before the acceptance and use of UAVs can be expected to expand, advances must occur in the general areas of reliability, survivability, and autonomy. In order to enhance the reliability, survivability and autonomy of UAVs, advanced intelligent control and health management technologies are required, which will enable UAVs to have the capabilities of state awareness and self-adaptation.

Inspired by the above challenges, this research aims towards the design, analysis and experimental implementation of fault diagnosis, fault-tolerant control, and controller verification methods to achieve safety assurance and trusted autonomy of quadrotor UAVs. First, the issue of sensor faults is investigated under two different scenarios: (1) the case when all Euler angles are available for measurement; (2) the case when roll and pitch angles are not measurable and need to be estimated. Next, the issue of fault-tolerant control of quadrotor UAVs with actuator faults is considered. Two approaches for fault-tolerant attitude tracking are developed. First, the integration of an actuator fault diagnosis scheme with a fault accommodation algorithm is investigated.

The fault diagnostic information is used to ensure fault-tolerance to actuator faults. Second, a nonlinear adaptive fault-tolerant altitude and attitude controller is developed to automatically stabilize and recover tracking performance of the quadrotor. The adaptive control method is designed to handle possible multiple simultaneous actuator faults without the need of a fault diagnosis mechanism. Finally, a run-time assurance architecture is investigated for the verification and validation of the adaptive fault-tolerant controller. The algorithms are presented with a rigorous analytical framework aimed at characterizing their performance properties. The above algorithms are implemented and evaluated using a real-time indoor quadrotor test environment. Experimental flight test results are shown to illustrate the effectiveness of the proposed methods. The remainder of this dissertation is organized as follows:

- **Chapter 2** includes a brief overview of model-based fault diagnosis and fault-tolerant control methods, recent developments of these methods for quadrotor platforms, and the research motivation highlighting the contribution of this dissertation.

- **Chapter 3** provides an overview of the quadrotor mathematical model and the real-time experimental architecture setup.

- **Chapter 4** describes the sensor fault diagnosis method when all Euler angles are available for measurement. Sensor faults are modeled as biases in the accelerometer and gyroscope measurements. A nonlinear fault diagnosis scheme is developed to detect, isolate and estimate the possible simultaneous occurrence of such faults.

- In **Chapter 5**, we extend the results in Chapter 4, by relaxing the assumption on roll and pitch measurement. Based on the sliding-mode technique, a new roll and pitch angle estimation method is designed. Using the estimated roll and pitch angles, a diagnostic scheme is developed for detecting, isolating and estimating possible simultaneous accelerometer and gyroscope faults.

- **Chapter 6** presents the systematic design of a fault detection, isolation, and accommodation algorithm for quadrotor actuator faults using nonlinear adaptive estimation techniques. Adaptive thresholds for fault detection and isolation are systematically designed to enhance the robustness and fault sensitivity of the diagnostic algorithm. Additionally, after fault isolation, the fault parameter estimate

generated by the matched adaptive isolation estimator is used for accommodating the effect of the fault.

- In **Chapter 7**, the design of a nonlinear altitude and attitude adaptive fault-tolerant controller which does not need a fault detection and isolation mechanism is described. The adaptation in the control law arises due to the unknown fault magnitudes. Based on nonlinear adaptive backstepping technique, the fault-tolerant control algorithm guarantees asymptotic convergence of the altitude and attitude tracking error even in the presence of possible multiple actuator faults and modeling uncertainties.

- **Chapter 8** describes the the design of a run-time assurance (RTA) algorithm for the adaptive fault-tolerant controller presented in the Chapter 7. The objective is to monitor and detect software faults and potential malfunctions in the adaptive controller.

- **Chapter 9** includes some concluding remarks and some discussion of possible future research directions.

II. MODEL-BASED FAULT DIAGNOSIS AND FAULT-TOLERANT CONTROL

This section introduces general concepts of fault diagnosis (FD) and fault-tolerant control (FTC). Furthermore, a literature review of state of the art FD and FTC methods with application to quadrotor UAVs is presented, highlighting some of the research challenges and open topics. Based on these discussion, the research objectives and contribution of this dissertation are presented.

GENERAL OVERVIEW OF MODEL-BASED FD AND FTC METHODS

Definition [5]: A **fault** is an unpermitted deviation of at least one characteristic property of a variable from an acceptable behavior.

Fault diagnosis and fault-tolerant control are crucial components for the safe operation of most engineering applications. Based on their intrinsic components properties and fabrication process, electro-mechanical systems are always prone to faults. The unsupervised occurrence of a fault could lead to undesired performance, loss of controllability and even catastrophic outcomes. As a consequence, early information about fault occurrence, its location, and magnitude plays an integral role in the overall control and stability of such systems.

In *hardware redundant* fault diagnosis approaches, the occurrence and possibly the location of a fault can be determined at the expense of additional sensors, actuators or other components. Obviously, this method has severe drawbacks due to increased component cost and additional space needed to accommodate redundant hardware. This is especially true in the case of unmanned air vehicle systems, which are constrained with limited payload. In order to overcome these issues and fueled by the advances in computing technology, model-based fault diagnosis methods have been developed, contributing significantly to the growth of more intelligent and cost effective diagnosis methods [5–7].

Figure 2.1 shows a general architecture of fault diagnosis system using the model-based approach. Model-based fault diagnosis is typically comprised of two processes:

1.) *Residual Generation:* residuals are generated by taking the difference between the system's actual measurements and its estimation obtained from a mathematical model.

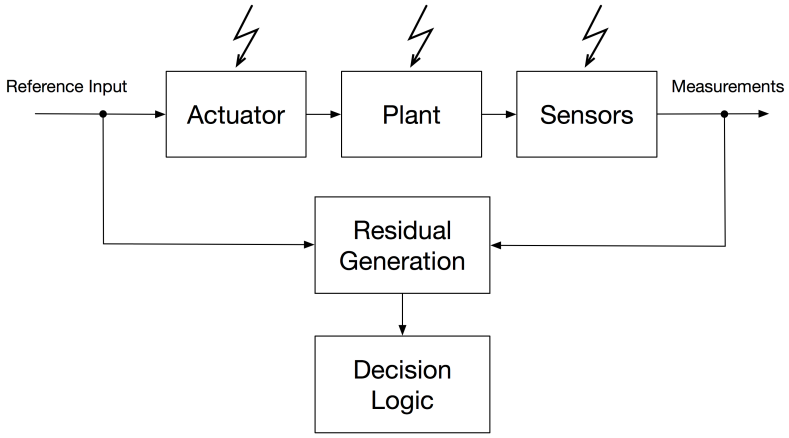

Figure 2.1: General Model-Based Fault Diagnosis Architecture.

2.) *Decision Logic:* the residuals are analyzed against appropriately designed thresholds within a decision scheme with the purpose of generating fault information, such as occurrence, location or magnitude.

Generally speaking, faults can be classified in the following three categories:

i) *sensor faults* corrupt the system measurements, causing a deviation between actual and sensed input/output variables,

ii) *actuator faults* represent discrepancies between commanded input and actual input to the system,

iii) *process/component faults* are physical failures of the system components which lead to changes in the normal system dynamics.

The fault diagnosis procedure consists of three main tasks: (i) fault detection indicates the occurrence of a fault in a system; (ii) fault isolation localizes and identifies the type of fault; (iii) fault identification provides an estimation of the fault magnitude.

Once a fault has been diagnosed (detected, isolated and identified) it is highly desirable to use this information in order to maintain/recover the safe operation of the system after fault occurrence. To this end, advanced control systems aim to achieve fault tolerance and compensate for the effects of the faults in the system. Typically, fault-tolerant control systems are divided into two categories: (i) passive fault-tolerant control, which relies on the robustness of the control law with fixed parameters to maintain system performance in the presence of the fault; (ii) active fault-tolerant control, which

consists of adjusting controller signals based on fault information provided by a fault diagnosis system.

LITERATURE REVIEW OF FDI AND FTC WITH APPLICATION TO QUADROTOR UAVS

In recent years the use of quadrotors has grown substantially, both in military and civilian applications. When subjected to sensor or actuator faults, quadrotors can possibly not only fail to complete a given task, but also become a hazard to their inherent environment. Therefore, exceptional attention must be paid when dealing with faults in such systems.

Quadrotors belong to a smaller class of hovering unmanned air vehicles. Unlike traditional helicopters, fixed pitch blades are used to generate lift. Quadrotors are structurally less complex than helicopters, while preserving vertical take-off and landing (VTOL) capabilities. Additionally, when compared to fixed wing UAVs, quadrotors are not constrained by the need of large flight areas, which makes them ideal candidates for indoor flight and research projects.

Quadrotors are often equipped with low-cost and lightweight micro-electro-mechanical systems (MEMS) inertial measurement units (IMU) including 3-axis gyroscope, accelerometer, and magnetometer. These sensors play an essential role in most quadrotor navigation and control applications. However, as discussed in [8], the mechanical components of MEMS tend to break down in a catastrophic manner, while the electronic elements often undergo a gradual degradation process (for instance, the values of micro-resistors may change slowly). Therefore, IMU measurements of are susceptible to bias faults as a result of component damage/degradation, temperature variation, excessive vibration, etc. The detection and estimation of these sensor faults plays an important role in the safe operations of quadrotors [9–11].

Quadrotors are equipped with four propellers, mounted on the shafts of four brushless DC motors, respectively. The spinning of the rotors generates the required thrust to maintain the quadrotor airborne. Additionally, the quadrotor attitude is controlled by systematically varying the rotor velocities which generate moment forces acting on the body frame. However, the actuating motor-propeller system is prone to faults due to component degradation or damage to the motors, propellers, etc. The occurrence of

such actuator faults could lead to undesirable effects on the tracking performance and stability of the closed-loop control system [10].

Most fault diagnosis methods with application to quadrotor UAVs deal exclusively with actuator faults, and research results on quadrotor sensor fault detection and isolation (FDI) are still limited [10]. Following the well-known architectural framework of Generalized Observer Scheme (GOS) [6], several researchers have developed interesting quadrotor sensor FDI methods using various observer or estimator techniques, including robust linear parameter varying (LPV) observer [9], set membership based estimation [12], nonlinear identity observer [13], and reduced-order nonlinear observers [14], etc. The GOS architecture consists of a bank of diagnostic observers or estimators, where each observer uses the measurements from all sensors except one. Since GOS-based sensor fault diagnosis methods is designed based on the assumption of single fault occurrence, the case of multiple simultaneous sensor faults were not considered. In [11], a Thau observer is employed based on full attitude measurement, for the detection of accelerometer bias. The work of [15, 16] assumes that the quadrotor behaves in a quasi-static manner, that is the translational acceleration is zero. Based on this assumption the detection of gyroscope, accelerometer and magnetometer faults is designed. Additionally, interesting results have also been obtained using Kalman filter (KF) based methods for simultaneous estimation of quadrotor vehicle state and sensor bias (see, for instance, methods using the extended KF [17, 18], observer Kalman filer identification (OKID) technique [19], and the unscented KF [20]). However, a stability analysis for extended KF or unscented KF applied to parameter estimation of nonlinear systems is very difficult, and the extra system state variables introduced to represent the unknown sensor fault parameters make it more difficult to satisfy the observability condition with limited sensor measurements.

Various methods for attitude stabilization or tracking of quadrotor UAVs have been presented, including PD^2 control structure [21], backstepping technique [22], disturbance rejection control strategy [23], and adaptive control [24]. These control schemes are designed by assuming the absence of faults in the quadrotor system. Actuator faults pose a greater threat to the overall control and stability of quadrotor UAV systems. A partial loss of efficiency in one or more of the rotors results in the immediate loss of thrust and torque generated by the faulty rotor. This can significantly degrade the quadrotor

performance, and if unattended can quickly destabilize the quadrotor resulting in an imminent crash. Fault-tolerant control can be designed based on either an integrated fault diagnosis and accommodation architecture or an adaptive control framework that automatically adapts to fault effects without the need of a fault diagnosis mechanism. Hence, actuator fault diagnosis and fault-tolerant control has received much attention.

Early fault detection and isolation (FDI) can potentially avoid the development of more serious faults. Detailed fault information acquired by a fault diagnosis procedure is very valuable to condition-based maintenance, redundancy management, and FTC. Most of the existing quadrotor actuator fault diagnosis methods are evaluated using simulation results [10]. For instance, an interesting actuator fault reconstruction method is developed in [25] using a sliding mode observer. It is assumed that the perturbations from hover flight are small to obtain a linear relationship between Euler angle rates and body angular rates. Systematic quadrotor actuator FDI methods presented with experimental results are still limited. Some exciting experimental results have been obtained using a two-stage Kalman filter [26], an adaptive Thau observer [27], and sliding mode techniques [28]. However, these FDI methods are developed either based on a linearized model [26] or by assuming a linear relationship between Euler angle rates and body angular rates [27, 28]. The experimental results were obtained while the quadrotor was kept hovering at a stable position. Additionally, the FDI thresholds used in [26–28] are fixed constants chosen manually. Moreover, the important issue of integrating FDI with FTC was not considered in [27, 28].

Alternatively, advanced adaptive control systems have also attracted significant attention because of the potential to achieve fault-tolerance without the need of a fault detection and isolation mechanism. Several adaptive FTC methods for accommodating quadrotor actuator faults without using a fault detection and isolation component have been reported in the literature. In [29, 30], model reference adaptive control designs based on a *linearized* quadrotor model at the hovering condition are presented with interesting experimental flight test results. Additionally, an adaptive attitude tracking controller was developed in [31] using a unit quaternion representation and indirect adaptive control techniques, which is evaluated using only simulation results. Systematic adaptive FTC design (without a fault diagnosis mechanism) that is directly based on the intrinsic *nonlinearity* of quadrotor dynamics and tested with real-time experimental

results is still very limited.

RESEARCH MOTIVATION

The fault diagnosis and fault-tolerant control methods with application to quadrotors described above are very interesting and represent for the most part the current state of the art. This dissertation aims to improve and expand current results of fault diagnosis for quadrotor UAVs by specifically targeting the following areas of interest: *(1) sensor fault diagnosis, (2) actuator fault diagnosis and quadrotor fault-tolerant control, (3) quadrotor controller integrity monitoring.* Additionally, real-time experimental results are shown to illustrate the effectiveness of the proposed algorithms.

SENSOR FAULT DIAGNOSIS

Most of the sensor fault diagnosis results listed in the previous Section are presented in a simulation environment and/or are based on simplified quadrotor dynamics. Additionally, reported sensor faults diagnosis results typically focus on the diagnosis of a single fault, and simultaneous accelermoter and gyroscope faults are not considered.

In this research, a nonlinear method for detecting, isolating, and estimating possible simultaneous sensor bias faults in accelerometer and gyroscope measurements of quadrotor UAVs is presented. Based on the quadrotor dynamics and sensor models under consideration, the effects of sensor faults are represented as virtual actuator faults in the quadrotor state equation. Two nonlinear diagnostic estimators are designed to provide structured residuals for fault detection and isolation. Additionally, after the fault is detected and isolated, a nonlinear adaptive estimation scheme is employed for estimating the unknown fault magnitude. The stability and parameter convergence properties of the adaptive estimation scheme are analyzed in the presence of sensor measurement noise.

In Chapter 5, the critical assumption that roll and pitch angles are measurable is removed and a new sensor fault diagnosis scheme is designed. Based on sliding-mode observer techniques, a robust estimation of the quadrotor roll and pitch angles is obtained by only using accelerometer measurements. Then, a diagnostic scheme is developed for detecting, isolating, and estimating sensor bias faults in the gyroscope and accelerometer measurements. Structured residuals are generated, allowing the detection

and isolation of multiple simultaneous IMU sensor faults under consideration. After the faults are detected and isolated, two nonlinear estimators are employed to provide an estimate of the unknown fault magnitude. The stability and estimation performance properties of the nonlinear estimators are established.

ACTUATOR FAULT DIAGNOSIS AND FAULT-TOLERANT CONTROL

Actuator fault diagnosis and fault-tolerant control designed based on the intrinsic nonlinearity of quadrotor dynamics and demonstrated with real-time experimental results are still very limited and most of the fault-tolerant methods with application to quadrotor UAVs reported in literature do not consider the presence of modeling uncertainties during the design and analysis process. In this dissertation, we present the design, analysis, and experimental results of quadrotor actuator fault diagnosis and fault-tolerant control by using nonlinear adaptive techniques.

In Chapter 6 the systematic design and real-time experimental results of a fault detection, isolation, estimation and accommodation algorithm for quadrotor actuator faults using nonlinear adaptive estimation techniques is presented. Adaptive thresholds for fault detection and isolation are designed to enhance the robustness and fault sensitivity of the diagnostic algorithm. Additionally, after fault isolation, the fault parameter estimate generated by the matched adaptive isolation estimator is used for accommodating the effect of the fault. Then, Chapter 7 presents the design, analysis and implementation of a new nonlinear robust adaptive fault-tolerant altitude and attitude controller for quadrotor UAVs subject to actuator faults without the need of a FDI component. The control algorithm guarantees asymptotic convergence of the altitude and attitude tracking error even in the presence of possible multiple actuator faults and modeling uncertainties. The stability of the quadrotor altitude and attitude system is shown using Lyapunov synthesis.

QUADROTOR ADAPTIVE CONTROLLER INTEGRITY MONITORING

Although various advanced fault-tolerant control methods for quadrotors have been proposed, few studies have investigated the issue of controller verification. Before such adaptive control systems can be adopted for use in safety-critical aerospace applications, it must be certified that the adaptive controller meets certain reliability and safety

requirements. For instance, adaptive control systems, such as the ones used in fault-tolerant control designs are also prone to controller malfunctions due to software faults and/or unanticipated hardware failures that could lead to violation of assumptions made during the design and analysis process [32]. Thus, validation and verification (V&V) of the adaptive fault-tolerant control scheme must be rigorously analyzed, in order to achieve safety assurance and trusted autonomy.

Based on Lyapunov stability criterion, an online controller integrity monitoring method is developed to detect software faults in the advanced adaptive controller. The general method presented in [33] is tailored and extended for the adaptive fault-tolerant controller developed in Chapter 7. Adaptive thresholds for software fault detection are derived, ensuring the robustness with respect to fault parameter approximation error. The fault detectability of the controller integrity monitoring algorithm is rigorously established.

III. QUADROTOR MODEL AND EXPERIMENTAL PLATFORM

QUADROTOR DYNAMICS

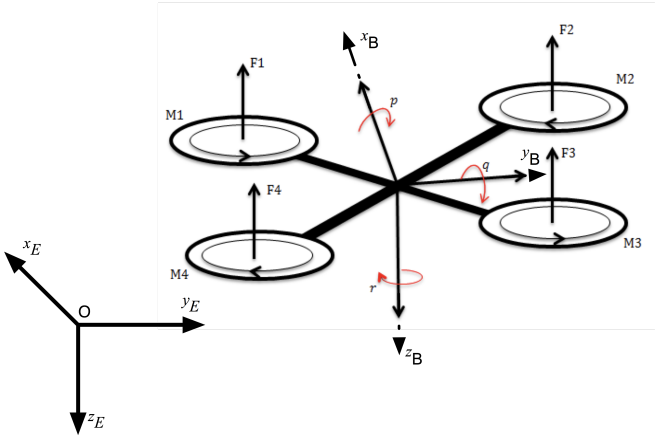

Figure 3.1: Quadrotor model in "X" configuration. $\mathcal{O}(x_E, y_E, z_E)$ represents the inertial frame and $\mathcal{O}(x_B, y_B, z_B)$ represents the body frame.

Figure 3.1 shows a simplified model of the quadrotor along with the assumed body and inertial frames. As can be seen, the quadrotor motors and propellers are configured such that rotors $M1$ and $M3$ rotate counter-clockwise, and rotors $M2$ and $M4$ rotate clockwise, when viewed from the top. Each rotor is located at a distance d from the quadrotor center of mass and produces a force F_s $(s = 1, .., 4)$ along the negative z direction relative to the body frame. Additionally, due to the spinning of the rotors, each rotor also generates a counter torque (τ_s) acting on the quadrotor body. In this research, the thrust and torque generated by the rotors are considered to be directly proportional to the square velocity of the rotors [10, 34]. Specifically, the relationship between the forces F_s and the reaction torques τ_s generated by each rotor and the rotor angular velocity is given by:

$$F_s = b_F {\Omega_s}^2 \tag{3.1}$$

$$\tau_s = -k \operatorname{sgn}(\Omega_s) {\Omega_s}^2 , \tag{3.2}$$

where b_F and k represent rotor thrust and torque constants, respectively, and $\operatorname{sgn}(\cdot)$ represents the signum function. Thus, based on the quadrotor configuration shown in Figure 3.1 and by using (3.1)-(3.2), the total thrust and moments acting on the quadrotor

body can be expressed as:

$$\begin{bmatrix} U \\ \tau_\phi \\ \tau_\theta \\ \tau_\psi \end{bmatrix} = M \begin{bmatrix} \Omega_1^2 \\ \Omega_2^2 \\ \Omega_3^2 \\ \Omega_4^2 \end{bmatrix}, \tag{3.3}$$

where the vector $[\Omega_1^2, \Omega_2^2, \Omega_3^2, \Omega_4^2]^T$ represents the commanded rotor velocities, and M represents the mapping matrix relating thrust and torques to rotor angular velocities [34]. Specifically, the mapping matrix is given by:

$$M = \begin{bmatrix} b_F & b_F & b_F & b_F \\ b_F a & -b_F a & -b_F a & b_F a \\ b_F a & b_F a & -b_F a & -b_F a \\ k & -k & k & -k \end{bmatrix}, \tag{3.4}$$

where $a = d/\sqrt{2}$, and d is the distance from the center of mass of each rotor to the center of mass of the quadrotor.

Several works focus on quadrotor modeling (see for example [35] and [36]). More recently, [34,37] have aimed for higher modeling accuracy by including drag force, Coriolis effects, blade flapping effects etc. Accurate modeling plays an important role in quadrotor control, especially in the case of aggressive maneuvers, tight group formations, etc. However, when the quadrotor is in a non-aggressive maneuver state, these effects become very small in comparison to gravitational pull and thrust generated by the rotors. The dynamic model used in this research considers the gravity, thrust generated by the rotors and drag forces acting on the quadrotor body.

The quadrotor nominal system dynamics derived from the Newton-Euler equations of motion are given by:

$$\dot{p}_E = v_E \tag{3.5}$$

$$\dot{v}_E = \frac{1}{m} R_{EB}(\eta) \left(\begin{bmatrix} 0 \\ 0 \\ -U \end{bmatrix} - c_{\mathbf{d}} v_B \right) + \begin{bmatrix} 0 \\ 0 \\ g \end{bmatrix} \tag{3.6}$$

$$\dot{\eta} = R_\eta(\phi, \theta)\omega \tag{3.7}$$

$$\dot{\omega} = \begin{bmatrix} \frac{J_y - J_z}{J_x} qr \\ \frac{J_z - J_x}{J_y} pr \\ \frac{J_x - J_y}{J_z} pq \end{bmatrix} + \begin{bmatrix} \frac{1}{J_x}\tau_\phi \\ \frac{1}{J_y}\tau_\theta \\ \frac{1}{J_z}\tau_\psi \end{bmatrix} \tag{3.8}$$

where the system state variables are $p_E \in \mathbb{R}^3$, $v_E \in \mathbb{R}^3$, $\eta \triangleq [\phi, \theta, \psi]^T$, and $\omega \triangleq [p\,, q\,, r]^T$, representing the inertial position, inertial velocity, Euler angles, and angular rates, respectively, and the system inputs include the thrust U, the rolling torque τ_ϕ, the pitching torque τ_θ, and the yawing torque τ_ψ. The rotation matrix R_{EB} in (3.6) is defined based on a standard *3-2-1* rotation sequence as

$$R_{EB}(\eta) = \begin{bmatrix} c\theta c\psi & s\phi s\theta c\psi - c\phi s\psi & c\phi s\theta c\psi + s\phi s\psi \\ c\theta s\psi & s\phi s\theta s\psi + c\phi c\psi & c\phi s\theta s\psi - s\phi c\psi \\ -s\theta & s\phi c\theta & c\phi c\theta \end{bmatrix} \tag{3.9}$$

where $s\cdot$ and $c\cdot$ are shorthand notations for the $\sin(\cdot)$ and $\cos(\cdot)$ functions, respectively. Additionally, the rotation matrix $R_\eta(\phi, \theta)$ in (3.7), relating angular rates to Euler angle rates, is given by:

$$R_\eta(\phi, \theta) = \begin{bmatrix} 1 & \sin\phi\tan\theta & \cos\phi\tan\theta \\ 0 & \cos\phi & -\sin\phi \\ 0 & \sin\phi\sec\theta & \cos\phi\sec\theta \end{bmatrix}. \tag{3.10}$$

The term $c_{\mathbf{d}} v_B$ in (3.6) represents the drag force acting on the vehicle frame, with $c_{\mathbf{d}}$ being the drag force coefficient and v_B representing the velocity of the quadrotor relative to the body frame. The remaining model parameters in (3.5) - (3.8) are the mass of the quadrotor m, the gravitational acceleration g, and the quadrotor moments of inertia about the body x-, y- and z-axis represented by J_x, J_y and J_z, respectively. The vehicle velocity v_E described in (3.6) is expressed relative to the inertial frame. The relationship between the inertial velocity v_E and the body velocity v_B is given by

$$v_E = R_{EB} v_B\,. \tag{3.11}$$

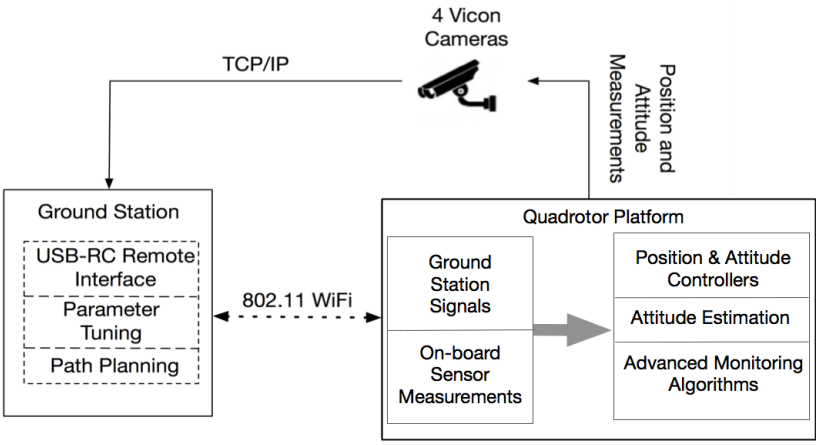

Figure 3.2: Experimental System Architecture Setup

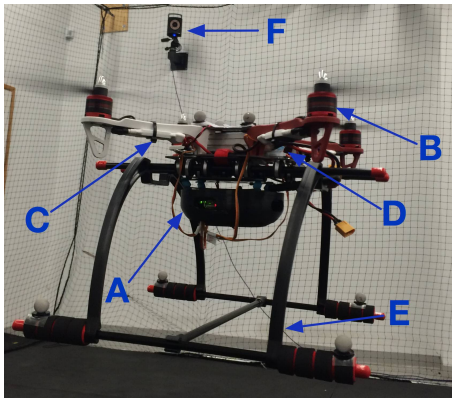

Figure 3.3: Experimental quadrotor platform in the Unmanned Air Vehicles Laboratory at Wright State University, Dayton OH.

EXPERIMENTAL PLATFORM

A block diagram of the real-time experimental system setup is shown in Figure 3.2 and is comprised of three main components: *(1) quadrotor platform*, which is built in-house with off the shelf components, *(2) Vicon motion capture system*, and *(3) ground station computer*. During flight tests, quadrotor position and attitude information is obtained from the motion capture camera system. The position and Euler angle measurements are collected every 10ms and relayed from a Vicon dedicated PC via TCP/IP connection to the ground station computer. The quadrotor is equipped with the Qbrain embedded control module from Quanser Inc. The control module consist of a HiQ acquisition card providing real-time IMU measurements, and a Gumstix DuoVero microcontroller running the real-time control software supporting up to 1kHz execution cycles. An IEEE802.11 connection between the ground station PC and the Gumstix allows for fast and reliable wireless data transmission and on-line parameter tuning. The

algorithms presented in the subsequent chapters are developed in Matlab/Simulink and execute on-board while the quadrotor is in flight.

Figure 3.3 shows the quadrotor while in flight, labeling the main components: Qbrain embedded control module (A), 4 propeller attached to four brushless DC motors mounted on a custom frame (B), four electronic speed controllers (C) regulating the rotors angular velocity based on the PWM signals generated by the on-board controller, a 3-cell 2000mAh, 12V battery (D), and a safety landing gear (E) added to provide improved protection of the control module during landing. Additionally, one of the Vicon cameras (F) can also be seen in the background.

IV. QUADROTOR SENSOR FAULT DIAGNOSIS WITH MEASURED ROLL & PITCH ANGLES

INTRODUCTION

In this chapter, a nonlinear method for detecting, isolating, and estimating sensor bias faults in accelerometer and gyroscope measurements of quadrotor UAVs is presented. The stability and convergence properties of the adaptive fault parameter scheme is also analyzed. Based on the fact that the accelerometer and gyroscope measure the specific forces/angular rates acting on the UAV body, the quadrotor dynamics are represented in terms of IMU measurements. Specifically, the measurements provided by the accelerometer are expressed as inputs in the quadrotor translational dynamics, and the measurements provided by the gyroscope are expressed as inputs in the quadrotor rotational dynamics. Thus, the measurements provided by the IMU sensors are represented as virtual actuators in the quadrotor dynamics, and the effects of IMU sensor biases are treated as virtual actuator faults. Two robust diagnostic estimators are designed to provide structured fault detection and isolation (FDI) residuals enabling the detection and isolation of simultaneous gyroscope and accelerometer sensor faults. In addition, by utilizing nonlinear adaptive estimation techniques [38, 39], adaptive estimators are employed to provide an estimate of the unknown sensor bias. The stability and parameter convergence properties of the adaptive estimation scheme are analyzed in the presence of sensor measurement noise. The sensor fault diagnosis method is implemented using a real-time indoor quadrotor test environment. Real-time experimental results are shown to illustrate the effectiveness of the diagnostic method.

PROBLEM FORMULATION

Recall the quadrotor nominal system dynamics:

$$\dot{p}_E = v_E \tag{4.1}$$

$$\dot{v}_E = \frac{1}{m} R_{EB}(\eta) \left(\begin{bmatrix} 0 \\ 0 \\ -U \end{bmatrix} - c_{\mathbf{d}} v_B \right) + \begin{bmatrix} 0 \\ 0 \\ g \end{bmatrix} \tag{4.2}$$

$$\dot{\eta} = \begin{bmatrix} 1 & \sin\phi\tan\theta & \cos\phi\tan\theta \\ 0 & \cos\phi & -\sin\phi \\ 0 & \sin\phi\sec\theta & \cos\phi\sec\theta \end{bmatrix} \omega \tag{4.3}$$

$$\dot{\omega} = \begin{bmatrix} \frac{J_y - J_z}{J_x} qr \\ \frac{J_z - J_x}{J_y} pr \\ \frac{J_x - J_y}{J_z} pq \end{bmatrix} + \begin{bmatrix} \frac{1}{J_x}\tau_\phi \\ \frac{1}{J_y}\tau_\theta \\ \frac{1}{J_z}\tau_\psi \end{bmatrix}, \tag{4.4}$$

where all the states and parameters in (4.1)-(4.4), have been defined in Chapter 3. As in [11, 18, 40], it is assumed that Euler angles measurements are available. For instance, these measurements can be generated by a camera-based motion capture system, a technology commonly employed for indoor UAV flight [18, 29, 41, 42].

MEMS sensors, such as accelerometers and gyroscopes, measure forces and moments acting in the body frame. By considering IMU measurements susceptibility to bias faults, in this research, the accelerometer and gyroscope sensor measurements are assumed to be given by:

$$y_a(t) = a(t) + \beta_a(t - t_a)b_a + n_a(t) \tag{4.5}$$

$$y_\omega(t) = \omega(t) + \beta_\omega(t - t_\omega)b_\omega + n_\omega(t) \tag{4.6}$$

where $y_a(t) \in \mathbb{R}^3$ is the accelerometer measurement, $y_\omega(t) \in \mathbb{R}^3$ is the gyroscope measurement, $b_a \in \mathbb{R}^3$ and $b_\omega \in \mathbb{R}^3$ represent sensor bias faults in accelerometer and gyroscope measurements, respectively, the terms $n_a(t)$ and $n_\omega(t)$ represent the measurement noise, and:

$$a(t) = \frac{1}{m}\left(\begin{bmatrix} 0 \\ 0 \\ -U \end{bmatrix} - c_{\mathbf{d}} v_B(t)\right). \tag{4.7}$$

represents the nominal acceleration measurement without bias and noise. Additionally, $\beta_a(\cdot)$ and $\beta_\omega(\cdot)$ are fault time profile functions with unknown fault occurrence times t_a and t_ω, respectively. In this research, they are modeled as step functions given by:

$$\beta_a(t - t_a) = \begin{cases} 0\,, & \text{when } t < t_a \\ 1\,, & \text{when } t \geq t_a \end{cases}$$

$$\beta_\omega(t - t_\omega) = \begin{cases} 0\,, & \text{when } t < t_\omega \\ 1\,, & \text{when } t \geq t_\omega \end{cases}$$

Additionally, it is assumed that the position measurements in the Earth frame are available. Hence, the system model is augmented by the following output equation:

$$y_p(t) = p_E(t) + d_p(t) \tag{4.8}$$

where $d_p(t)$ represents zero mean position measurement noise.

Assumption 4.1. The sensor biases b_a and b_ω in (4.5) and (4.6) are assumed to be constant and bounded.

Assumption 4.2. The sensor measurement noises, denoted by $n_a(t)$, $n_\omega(t)$ and $d_p(t)$ in (4.5), (4.6), and (4.8), respectively, are assumed to be bounded zero mean signals. That is:

$$\mathbb{E}(n_a) = 0, \qquad \mathbb{E}(n_\omega) = 0, \qquad \mathbb{E}(d_p) = 0,$$

where $\mathbb{E}$ represents the expectation operator.

Remark 4.1. It is worth noting that, in practical applications, after the occurrence of an IMU sensor bias, its magnitude may be time-varying and grow slowly over time. However, the change in the bias is often small over a short time duration [43]. Therefore, the bias may be assumed to be constant on the short time duration under consideration.

The objective of this chapter focuses on the design, analysis, and experimental demonstration of a robust fault detection, isolation, and estimation scheme for sensor bias faults in accelerometer and gyroscope measurements described by (4.5) and (4.6).

FAULT DETECTION AND ISOLATION METHOD

This section presents the proposed method for detecting and isolating sensor faults in accelerometer and gyroscope measurements. Substituting the sensor model given by

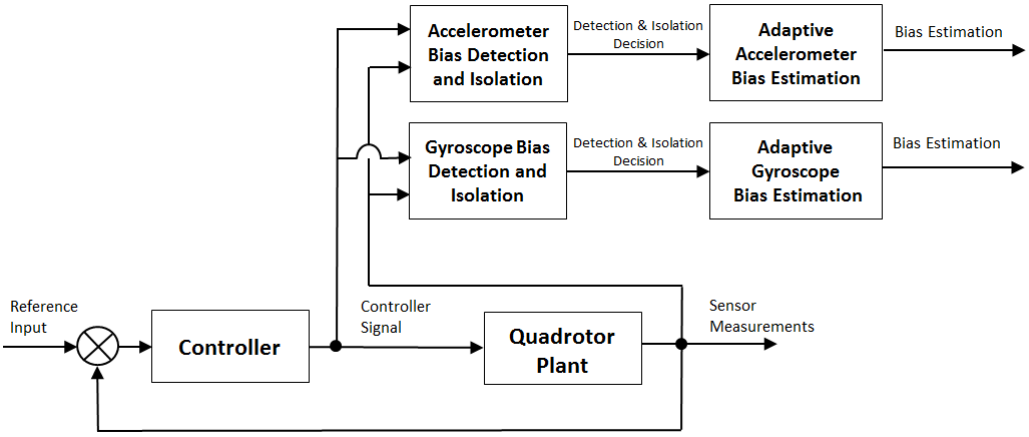

Figure 4.1: Sensor fault diagnosis architecture.

(4.5) - (4.6) into the systems dynamics (4.1) - (4.4), we obtain:

$$\dot{p}_E = v_E \tag{4.9}$$

$$\dot{v}_E = R_{EB}(\eta)y_a + \begin{bmatrix} 0 \\ 0 \\ g \end{bmatrix} - R_{EB}(\eta)\beta_a b_a - R_{EB}n_a \tag{4.10}$$

$$\dot{\eta} = R_\eta(\phi,\theta)y_\omega - R_\eta(\phi,\theta)\beta_\omega b_\omega - R_\eta(\phi,\theta)n_\omega \tag{4.11}$$

$$\dot{\omega} = \begin{bmatrix} \frac{J_y - J_z}{J_x}(y_q - \beta_\omega b_q - d_q)(y_r - \beta_\omega b_r - d_r) \\ \frac{J_z - J_x}{J_y}(y_r - \beta_\omega b_r - d_r)(y_p - \beta_\omega b_p - d_p) \\ \frac{J_x - J_y}{J_z}(y_p - \beta_\omega b_p - d_p)(y_q - \beta_\omega b_q - d_q) \end{bmatrix} + \begin{bmatrix} \frac{1}{J_x}\tau_\phi \\ \frac{1}{J_y}\tau_\theta \\ \frac{1}{J_z}\tau_\psi \end{bmatrix}. \tag{4.12}$$

As can be seen from (4.9) - (4.12), a bias in accelerometer measurements only appears in the position and velocity dynamics. On the other hand, a bias in gyroscope measurements only appears in the Euler angles and angular rate dynamics. Based on this observation, the effect of a bias in either sensor measurements can be treated as a virtual actuator fault. In addition, due to the decoupling of the two sensor faults in the quadrotor state equations, it follows naturally to also divide the fault diagnosis tasks of these two types of sensor faults. The proposed fault diagnosis architecture is shown in Figure 4.1. As can be seen, under normal operating conditions, two FDI estimators monitor the system for detecting and isolating fault occurrences in accelerometer and gyroscope measurements. Once a fault is detected and isolated, the corresponding nonlinear adaptive estimator is activated for sensor bias estimation.

GYROSCOPE FAULT DIAGNOSTIC ESTIMATOR

Based on (4.11), the fault diagnostic estimator for the gyroscope bias can be designed as follows:

$$\dot{\hat{\eta}} = -\Lambda_1(\hat{\eta} - \eta) + R_\eta(\phi, \theta) y_\omega \,, \tag{4.13}$$

where $\hat{\eta} \in \mathbb{R}^3$ are the Euler angle estimates, and $\Lambda_1 \in \mathbb{R}^{3\times 3}$ is a positive-definite diagonal design matrix. Let the Euler angle estimation error be defined as:

$$\tilde{\eta} \triangleq \eta - \hat{\eta} \,. \tag{4.14}$$

Based on (4.11), (4.13) and (4.14), the dynamics of the attitude angle estimation error are given by:

$$\dot{\tilde{\eta}} = \dot{\eta} - \dot{\hat{\eta}} = -\Lambda_1 \tilde{\eta} - R_\eta(\phi, \theta)\beta_\omega b_\omega - R_\eta(\phi, \theta) n_\omega \,. \tag{4.15}$$

In the absence of a gyroscope fault (i.e. for $t < t_\omega$), the attitude angle estimation error is given by:

$$\begin{aligned} \tilde{\eta}(t) &= e^{-\Lambda_1(t-t_\omega)}\tilde{\eta}(0) - \int_0^t e^{-\Lambda_1(t-\tau)} R_\eta(\phi, \theta) n_\omega d\tau \\ &= r_\omega(t) + e_\omega(t) \end{aligned} \tag{4.16}$$

where $r_\omega(t) \triangleq e^{-\Lambda_1(t-t_\omega)}\tilde{\eta}(0)$ converges exponentially to zero, and

$$e_\omega(t) \triangleq -\int_0^t e^{-\Lambda_1(t-\tau)} R_\eta(\phi, \theta) n_\omega d\tau$$

represents an additive zero mean noise term generated by filtering the measurement noise n_ω through the following stable linear filter:

$$\dot{e}_\omega = -\Lambda_1 e_\omega - R_\eta(\phi, \theta) n_\omega \,.$$

Therefore, $\mathbb{E}(\tilde{\eta})$ converges exponentially to zero in the absence of faults. In addition, based on (4.15), it can be seen that the residual $\tilde{\eta}$ is only sensitive to gyroscope sensor bias b_ω. Thus, if $\mathbb{E}(\tilde{\eta})$ is significantly different from zero, it can be concluded that a fault in the gyroscope measurements has occurred.

ACCELEROMETER FAULT DIAGNOSTIC ESTIMATOR

The translational dynamics of the quadrotor described by (4.9) and (4.10) can be rewritten as follows:

$$\begin{aligned} \dot{x} &= Ax + f(\eta, y_a) + G_a(\eta)\beta_a b_a + D_a(\eta, t) \\ y &= Cx + d_p \end{aligned} \tag{4.17}$$

where $x = [p_E^T, v_E^T]^T$, $y = p_E$,

$$A = \begin{bmatrix} 0_{3\times3} & I_3 \\ 0_{3\times3} & 0_{3\times3} \end{bmatrix}, \quad G_a(\eta) = \begin{bmatrix} 0_{3\times3} \\ -R_{EB} \end{bmatrix},$$

$$f(\eta, y_a) = \begin{bmatrix} 0_{3\times1} \\ R_{EB}y_a + \begin{bmatrix} 0 \\ 0 \\ g \end{bmatrix} \end{bmatrix}, \quad D_a(\eta, t) = \begin{bmatrix} 0_{3\times1} \\ -R_{EB}n_a \end{bmatrix},$$

and $C = [I_3, 0_{3\times3}]$, where I_3 is a 3×3 identity matrix, $0_{3\times3}$ is a 3×3 matrix with all entries zeros, and $0_{3\times1}$ is a 3×1 zero vector. Based on (4.17), the following fault diagnostic observer is chosen:

$$\begin{aligned} \dot{\hat{x}} &= A\hat{x} + f(\eta, y_a) + L_1(y - \hat{y}) \\ \hat{y} &= C\hat{x} \end{aligned} \tag{4.18}$$

where $\hat{x} \in \mathbb{R}^6$ represents the inertial position and velocity estimation, $\hat{y} \in \mathbb{R}^3$ are the estimated position outputs, L_1 is a design matrix chosen such that the matrix $\bar{A}_1 \triangleq (A - L_1C)$ is asymptotically stable. Note that (A, C) is an observable pair.

Define the position estimation error as:

$$\tilde{y} \triangleq y - \hat{y}, \tag{4.19}$$

Using equations (4.17) - (4.18), the estimation error dynamics are given by:

$$\begin{aligned} \dot{\tilde{x}} &= \bar{A}_1\tilde{x} + G_a(\eta)\beta_a b_a + D_a(\eta, t) - L_1 d_p \\ \tilde{y} &= C\tilde{x} + d_p . \end{aligned} \tag{4.20}$$

In the absence of accelerometer bias (i.e. for $t < t_a$), the position estimation error is given by:

$$\begin{aligned}\tilde{y}(t) &= Ce^{\bar{A}_1(t-t_a)}\tilde{x}(0) + C\int_0^t e^{\bar{A}_1(t-\tau)}(D_a(\eta,\tau) - L_1 d_p)d\tau + d_p(t) \\ &= r_a(t) + e_a(t) + d_p(t)\,, \end{aligned} \tag{4.21}$$

where $r_a(t) \triangleq Ce^{\bar{A}_1(t-t_a)}\tilde{x}(0)$ converges exponentially to zero, and

$$e_a(t) \triangleq C\int_0^t e^{\bar{A}_1(t-\tau)}(D_a(\eta,\tau) - L_1 d_p)d\tau$$

represents an additive zero mean noise term generated by filtering $n_a(t)$ and $d_p(t)$ through the following stable linear filter:

$$\dot{e}_a = \bar{A}_1 e_a + \Big(D_a(\eta,t) - L_1 d_p(t)\Big)\,.$$

Clearly, $\mathbb{E}(\tilde{y})$ reaches zero exponentially in the absence of the accelerometer bias b_a. Furthermore, it can be seen from (4.20), the residual $\tilde{y}$ is only sensitive to the bias b_a. Therefore, if any component of $\mathbb{E}(\tilde{y})$ deviates significantly from zero, it can be concluded that a fault in the accelerometer sensor measurement has occurred.

FAULT DETECTION AND ISOLATION DECISION SCHEME

As described in previous Sections, the two fault diagnostic estimators are designed such that each of them is only sensitive to one type of sensor faults. Based on this observation, the residuals $\tilde{\eta}(t)$ and $\tilde{y}(t)$ generated by (4.16) and (4.21) can also be used as structured residuals for fault isolation. More specifically, the following fault detection and isolation decision scheme is formulated:

- In the absence of any faults, all components of $\mathbb{E}(\tilde{\eta})$ and $\mathbb{E}(\tilde{y})$ should be close to zero.
- If all components of $\mathbb{E}(\tilde{\eta})$ remain around zero, and at least one component of $\mathbb{E}(\tilde{y})$ is significantly different from zero, then it can be concluded that an accelerometer fault has occurred.
- If all components of $\mathbb{E}(\tilde{y})$ remain around zero, and at least one component of $\mathbb{E}(\tilde{\eta})$

is significantly different from zero, then it can be concluded that a gyroscope fault has occurred.

- If at least one component of $\mathbb{E}(\tilde{\eta})$ and at least one component of $\mathbb{E}(\tilde{y})$ are both significantly different from zero, then it can be concluded that both a gyroscope and an accelerometer sensor measurement fault has occurred.

The above FDI decision scheme is summarized in Table 1, where "0" represents residuals with zero mean, and "1" represents significantly non-zero residuals.

Table 4.1: Fault Isolation Decision Truth Table.

	No Fault	Gyro Bias	Accel Bias	Accel & Gyro Bias
$\mathbb{E}(\tilde{\eta})$	0	1	0	1
$\mathbb{E}(\tilde{y})$	0	0	1	1

FAULT ESTIMATION

As shown in Figure 4.1, once a sensor fault is detected and isolated, the corresponding nonlinear adaptive estimator is activated for estimating the unknown fault magnitude in the accelerometer and/or gyroscope measurements. In this section, the design of nonlinear adaptive estimators for sensor bias estimation is described.

ACCELEROMETER FAULT ESTIMATION

Based on (4.17), the adaptive observer for estimating the accelerometer bias magnitude is chosen as:

$$\dot{\hat{x}} = A\hat{x} + f(\eta, y_a) + L_2(y - \hat{y}) + G_a(\eta)\hat{b}_a + \Omega\dot{\hat{b}}_a \tag{4.22}$$

$$\dot{\Omega} = (A - L_2C)\Omega + G_a(\eta) \tag{4.23}$$

$$\hat{y} = C\hat{x}\,, \tag{4.24}$$

where $\hat{x}$ is the estimated position and velocity vector, $\hat{y}$ is the estimated position output, $\hat{b}_a$ is the estimated sensor bias, and L_2 is the observer gain matrix. The adaptation in the above adaptive estimator arises due to the unknown bias b_a. The adaptive law for

updating $\hat{b}_a$ is derived using Lyapunov synthesis approach [39, 44] and is given by:

$$\dot{\hat{b}}_a = \Gamma \Omega^T C^T \tilde{y}\,, \tag{4.25}$$

where $\Gamma > 0$ is a symmetric and positive-definite learning rate matrix, and $\tilde{y}_a \triangleq y_a - \hat{y}_a$ is the output estimation error. Let us also define the state estimation error as $\tilde{x} \triangleq x - \hat{x}$, and the parameter estimation error as $\tilde{b}_a \triangleq \hat{b}_a - b_a$. The stability and performance properties of the above adaptive scheme are described below.

Theorem 4.1 *Suppose that an accelerometer sensor bias fault occurs at $t_a \geq 0$ and is detected at some time $T_a > t_a$. Then, if there exists constants $\alpha_1 \geq \alpha_0 > 0$ and $T_0 > 0$, such that $\forall t > T_a$*

$$\alpha_1 I \geq \frac{1}{T_0} \int_t^{t+T_0} \Omega^T C^T C \Omega d\tau \geq \alpha_0 I\,, \tag{4.26}$$

the adaptive fault estimation scheme described by (4.22) - (4.25) guarantees that:

1. *all signals in the adaptive estimator remain bounded;*
2. *$\mathbb{E}(\tilde{x})$ and $\mathbb{E}(\tilde{b}_a)$ converge exponentially to zero.*

Proof. Based on (4.17) and (4.22), the dynamics governing the state estimation error dynamics are given by

$$\dot{\tilde{x}} = \bar{A}_2 \tilde{x} - G_a(\eta)\tilde{b}_a - \Omega \dot{\tilde{b}}_a + D_a(\eta, t) - L_2 d_p\,, \tag{4.27}$$

where $\bar{A}_2 \triangleq A - L_2 C$ and $\tilde{b}_a \triangleq \hat{b}_a - b_a$ is the parameter estimation error. By substituting $G_a(\eta) = \dot{\Omega} - (A - L_2 C)\Omega$ (see (4.23)) into (4.27), we have

$$\begin{aligned} \dot{\tilde{x}} &= \bar{A}_2 \tilde{x} - (\dot{\Omega} - \bar{A}_2 \Omega)\tilde{b}_a - \Omega \dot{\tilde{b}}_a + D_a(\eta, t) - L_2 d_p \\ &= \bar{A}_2(\tilde{x} + \Omega \tilde{b}_a) - \dot{\Omega}\tilde{b}_a - \Omega \dot{\tilde{b}}_a + D_a(\eta, t) - L_2 d_p\,. \end{aligned} \tag{4.28}$$

Note that, based on Asumption 1, we have $\dot{\tilde{b}}_a = \dot{\hat{b}}_a$. By defining $\bar{x} \triangleq \tilde{x} + \Omega \tilde{b}_a$, the above equation can be rewritten as:

$$\dot{\bar{x}} = \bar{A}_2 \bar{x} + D(\eta, t) - L_2 d_p\,, \tag{4.29}$$

where $\bar{A}_2$ is asymptotically stable by design (note that the pair $(A\,, C)$ is observable

by design). By noting that the terms $D(\eta, t)$ and $L_2 d_p$ in (4.29) are bounded (see Assumption 2), it follows that $\bar{x}$ is also bounded. By using the adaptive parameter estimation algorithm (4.25) and $\tilde{y} = C(\bar{x} - \Omega\tilde{b}) + d_p$, we obtain

$$\begin{aligned}\dot{\tilde{b}}_a = &\quad \Gamma\Omega^T C^T \tilde{y} \\ &= -\Gamma\Omega^T C^T C\Omega\tilde{b}_a + \Gamma\Omega^T C^T C\bar{x} + \Gamma\Omega^T C^T d_p. \end{aligned} \tag{4.30}$$

Note the condition given by (4.26) provides the required persistent excitation condition for parameter convergence [45]. Thus, using this property in conjunction with Theorem 2.2 from [46], it follows that the homogeneous part of (4.30) is exponentially stable. In addition, as can be seen from (4.23), Ω is also bounded, which along with Assumption 2 implies that all signals in (4.30) are bounded. Because $\bar{x}$, Ω and $\tilde{b}_a$ are bounded, it then follows that $\tilde{x}$ is also bounded. This concludes the proof of the first part of the theorem.

By taking the expectation of (4.29) and by using $\mathbb{E}(n_a) = 0$ and $\mathbb{E}(d_p) = 0$, we have:

$$\frac{d}{dt}\Big(\mathbb{E}(\bar{x})\Big) = \bar{A}_2\mathbb{E}(\bar{x}) + \mathbb{E}\Big(D_a(\eta, t) - L_2 d_p\Big) = \bar{A}_2\mathbb{E}(\bar{x})\,. \tag{4.31}$$

Clearly, $\mathbb{E}(\bar{x})$ converges to zero exponentially because of the stability properties of $\bar{A}_2$. By taking the expectation of (4.30), we have

$$\begin{aligned}\frac{d}{dt}\Big(\mathbb{E}(\tilde{b}_a)\Big) &= -\Gamma\Omega^T C^T C\Omega\mathbb{E}(\tilde{b}_a) + \Gamma\Omega^T C^T C\mathbb{E}(\bar{x}) \\ &\quad + \Gamma\Omega^T C^T\mathbb{E}(d_p) \\ &= -\Gamma\Omega^T C^T C\Omega\mathbb{E}(\tilde{b}_a)\,. \end{aligned} \tag{4.32}$$

Thus, based on the persistent of excitation condition (4.26), it follows from (4.32) that $\mathbb{E}(\tilde{b}_a)$ converges to zero exponentially. Finally, by applying the above results to the definition of $\bar{x}$, the second part of the theorem can be concluded. □

GYROSCOPE FAULT ESTIMATION

Based on (4.11), after the occurrence of a gyroscope bias fault is detected and isolated, the following adaptive estimator is designed in order to estimate the unknown

sensor bias:

$$\dot{\hat{\eta}} = -\Lambda_2(\hat{\eta} - \eta) + R_\eta(\phi, \theta) y_\omega - R_\eta(\phi, \theta)\hat{b}_\omega \tag{4.33}$$

$$\dot{\hat{b}}_\omega = \quad \Gamma R_\eta(\phi, \theta)^T(\hat{\eta} - \eta) \tag{4.34}$$

where $\hat{\eta}$ is the Euler angle estimate, $\hat{b}_\omega$ represents the estimation of the sensor bias, Λ and Γ are positive definite design matrices. The adaptive law given by (4.33) is derived using Lyapunov synthesis approach [45]. In addition, in order to ensure parameter convergence, $R_\eta(\phi, \theta)$ will need to satisfy the persistence of excitation condition [45], that is:

$$\alpha_1 I_3 \geq \frac{1}{T_0} \int_t^{t+T_0} R_\eta(\phi, \theta)^T R_\eta(\phi, \theta) d\tau \geq \alpha_0 I_3 \,, \tag{4.35}$$

for some constants $\alpha_1 \geq \alpha_0 > 0$ and $T_0 > 0$, and for all $t \geq T_\omega$, where T_ω is the gyroscope fault detection time and I_3 is the 3×3 identity matrix. Let us define the attitude angle estimation error as $\tilde{\eta} \triangleq \eta - \hat{\eta}$ and the bias estimation error as $\tilde{b}_\omega \triangleq \hat{b}_\omega - b_\omega$. The stability and learning performance of the adaptive estimation scheme (4.33) - (4.34) is given below.

Theorem 4.2 *Suppose that a gyroscope sensor bias fault occurs at time $t_\omega \geq 0$ and is detected at some time $T_\omega > t_\omega$. Then, if the PE condition given by (4.35) is satisfied, the adaptive scheme described by (4.33) - (4.34) guarantees that $\mathbb{E}(\tilde{\eta})$ and $\mathbb{E}(\tilde{b}_\omega)$ converge to zero exponentially.*

Proof. The state and parameter estimation error dynamics are given by

$$\dot{\tilde{\eta}} = -\Lambda_2 \tilde{\eta} + R_\eta(\phi, \theta)\tilde{b}_\omega - R_\eta(\phi, \theta) n_\omega \tag{4.36}$$

$$\dot{\tilde{b}}_\omega = -\Gamma R_\eta(\phi, \theta)^T \tilde{\eta} \,. \tag{4.37}$$

Because n_ω is bounded (see Assumption 2), it can be easily shown that all signals involved in (4.33) - (4.34) are bounded by considering $R_\eta(\phi, \theta) n_\omega$ as a bounded disturbance term. Additionally, by taking the expectation of (4.36) and (4.37), and by making use

of Assumption 2, we obtain

$$\frac{d\mathbb{E}(\tilde{\eta})}{dt} = -\Lambda_2 \mathbb{E}(\tilde{\eta}) + R_\eta(\phi,\theta)\mathbb{E}(\tilde{b}_\omega) \tag{4.38}$$

$$\frac{d\mathbb{E}(\tilde{b}_\omega)}{dt} = -\Gamma R_\eta(\phi,\theta)^T \mathbb{E}(\tilde{\eta})\,. \tag{4.39}$$

Defining $\epsilon_1 \triangleq \mathbb{E}(\tilde{\eta})$ and $\epsilon_2 \triangleq \mathbb{E}(\tilde{b}_\omega)$, we can rewrite equations (4.38) - (4.39) into the following compact form:

$$\begin{bmatrix} \dot{\epsilon}_1 \\ \dot{\epsilon}_2 \end{bmatrix} = \begin{bmatrix} -\Lambda_2 & R_\eta(\phi,\theta) \\ -\Gamma R_\eta(\phi,\theta)^T & O_{3\times 3} \end{bmatrix} \begin{bmatrix} \epsilon_1 \\ \epsilon_2 \end{bmatrix} \tag{4.40}$$

where $O_{3\times 3}$ is a 3×3 zero matrix. By following similar reasoning logics as given in the proof of Theorem 5.2.2 and Lemma 5.6.3 in [45], it can be shown that $(\epsilon_1\,, \epsilon_2) = (0\,, 0)$ is exponentially stable, hence, concluding the proof. □

Remark 4.2. It is worth noting that in practical applications, which do not require the quadrotor to perform aggressive maneuvers, the quadrotor pitch angle typically satisfies $|\theta| < 90°$. Therefore, for typical quadrotor flight, the matrix $R_\eta(\phi,\theta)$ is always full rank (see (3.10)) and the PE condition given by (4.35) is always satisfied.

EXPERIMENTAL RESULTS

In this section, real-time experimental results using an indoor quadrotor test environment are described to illustrate the effectiveness of the sensor fault diagnosis algorithm. A block diagram of the experimental system setup is shown in Figure 3.2. During flight tests, quadrotor position and attitude information is obtained from the Vicon motion capture camera system. Position measurements are corrupted with normal noise with standard deviation of 0.25m. Additionally, position measurements are down sampled to 1Hz, in order to further simulate real-world applications. The fault diagnosis method executes on-board and is evaluated in real-time during autonomous flight of a quadrotor built in-house with off-the-shelf components. As previously shown, the fault diagnosis technique employed in this approach is independent of the structure of the controller. Therefore, for brevity of presentation, the discussion on controller design is purposely omitted.

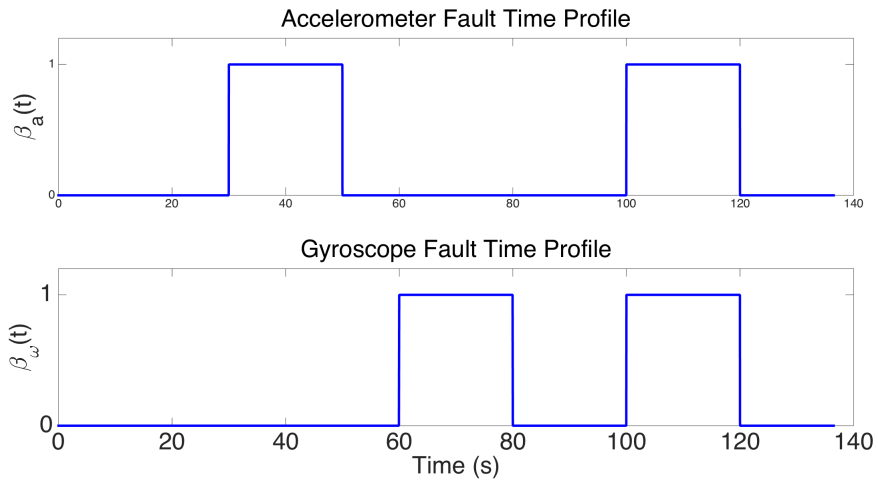

Figure 4.2: Sensor fault time profile

In order to evaluate the proposed diagnosis method sensor measurements are artificially corrupted by injecting a constant bias into the accelerometer and gyroscope measurements, respectively, while the quadrotor is airborne. Figure 4.2 shows the fault time profile of the two types of sensor faults under consideration. As can be seen, an accelerometer fault is introduced at time $t = 30s$ until $t = 50s$. Between time $t = 60s$ and time $t = 80s$, a gyroscope bias is injected into the sensor measurements. Additionally, in order to evaluate the performance of the FDIE algorithm in the presence of multiple faults, accelerometer and gyroscope faults are simultaneously injected at time $t = 100s$. Flight data is processed on-line, and real-time sensor fault diagnostic decision is generated by the diagnostic algorithm. In the following sections, the fault diagnosis results are detailed.

CASE OF ACCELEROMETER BIAS

The case of an accelerometer measurement bias fault is illustrated in this section. At time $t = 30s$, a constant bias $b_a = [0.15, 0.2, 0.75]^T m/s^2$, is injected into the accelerometer measurements. Figure 4.3 shows the residuals generated by the two diagnostic estimators described by (4.13) and (4.18), respectively. In order to enhance the diagnostic decision based on the FDI logic given by Table 1, the two-sided cumulative sum (CUSUM) test is applied to process the diagnostic residuals [47]. Figure 4.4 shows the statistic property generated by the CUSUM test. A fixed threshold is chosen for the detection and isolation of sensor faults. As can be seen, shortly after the occurrence of the fault, at least one component of the test statistic corresponding to the residuals

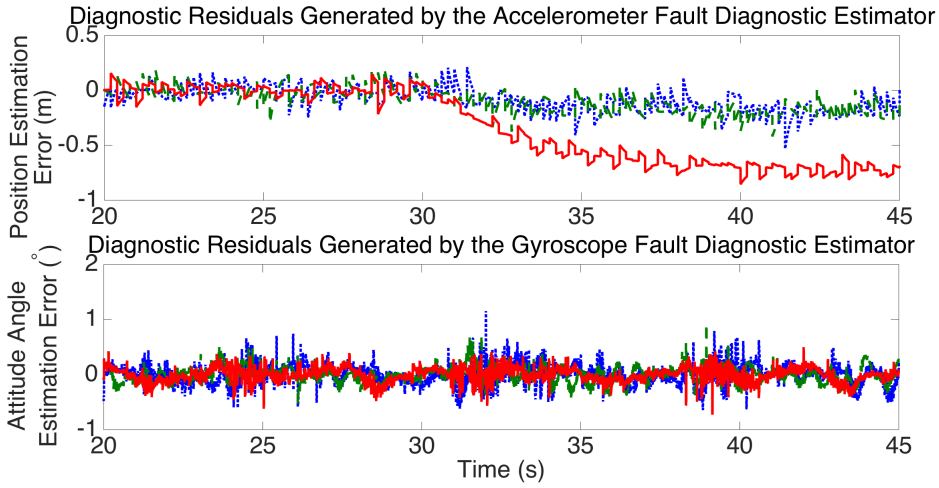

Figure 4.3: Raw diagnostic residuals: accelerometer bias fault

generated by the accelerometer diagnostic estimator exceeds the detection threshold, indicating the occurence of a fault in the accelerometer sensor. On the other hand, all components of the test statistic corresponding to the gyroscope bias remain well below the detection threshold. Based on the detection and isolation logic given in Table 1, it can be concluded that a fault has occurred in the accelerometer measurement.

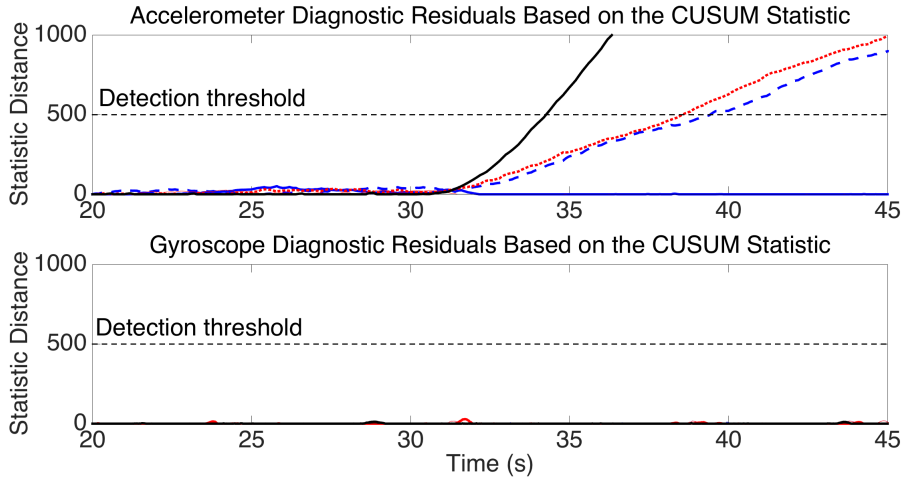

Figure 4.4: Diagnostic residual generated by CUSUM: accelerometer bias fault.

In addition, Figure 4.5 shows the estimation of the bias in the accelerometer for each axis, respectively. As can be seen, the estimate of accelerometer converges closely to the actual value.

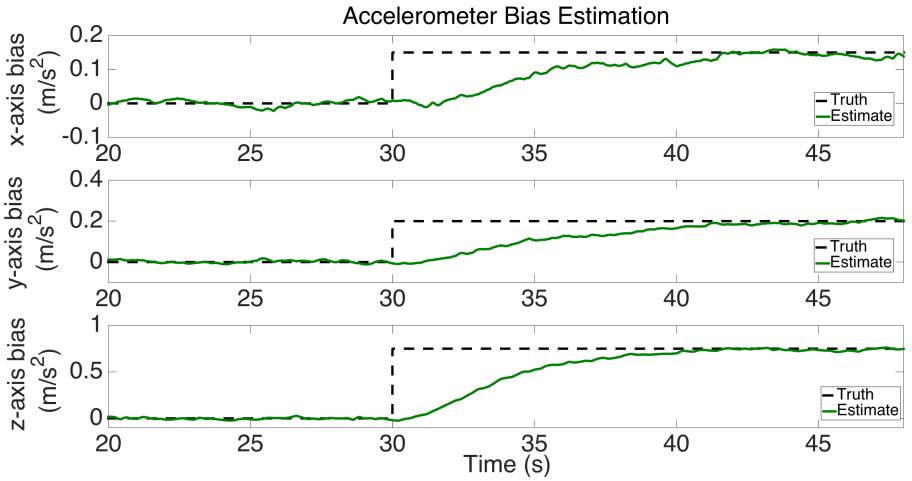

Figure 4.5: Accelerometer bias estimation.

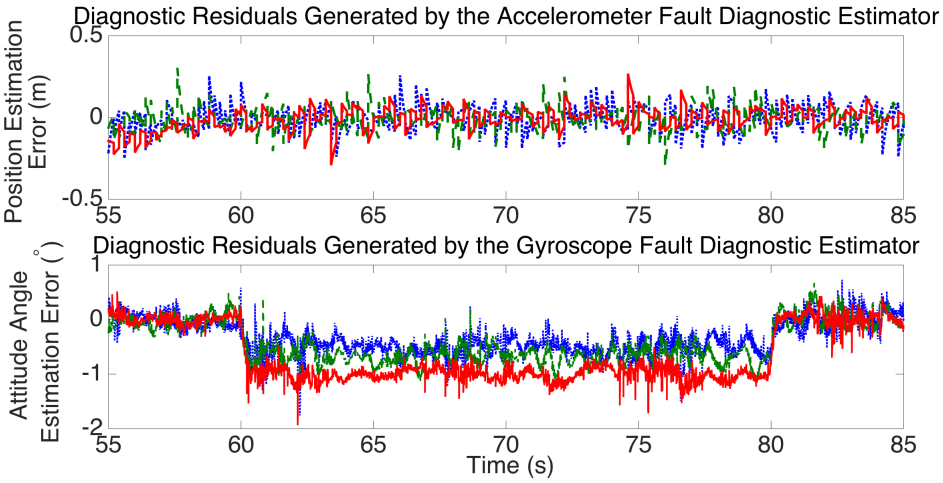

Figure 4.6: Raw diagnostic residuals: gyroscope bias fault

CASE OF GYROSCOPE BIAS

A gyroscope bias with $b_\omega = [5, -7, -10]^T$ $^\circ/s$ is injected into the sensor measurements at time $t = 60s$. Figure 4.6 shows the raw diagnostic residuals generated by (4.13) and (4.18), respectively. The results of the CUSUM test are shown in Figure 4.7. As can be seen, at least one component of the test statistic corresponding to the gyroscope sensor fault exceeds the detection threshold shortly after fault occurrence. On the other hand, all components of the test statistic corresponding to the accelerometer fault remain well below the detection threshold. Thus, it can be concluded that a fault has occurred in the gyroscope measurement.

In addition, Figure 4.8 shows the estimation of the bias in the gyroscope for each axis, respectively. As can be seen, after a short time, the estimate of gyroscope bias is

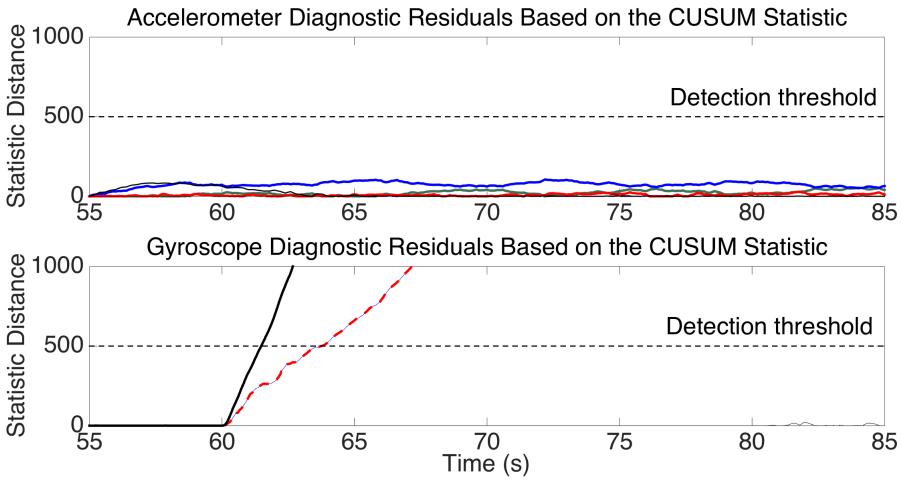

Figure 4.7: Diagnostic residual generated by CUSUM: gyroscope bias fault.

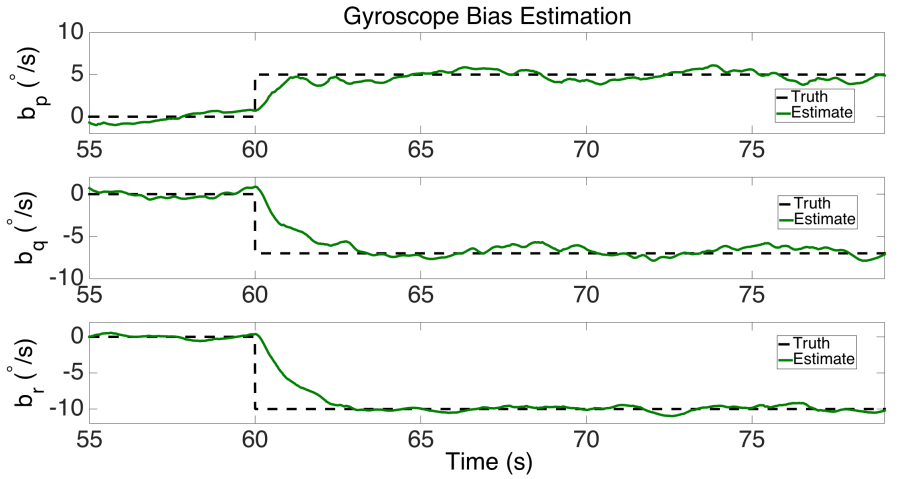

Figure 4.8: Gyroscope bias estimation.

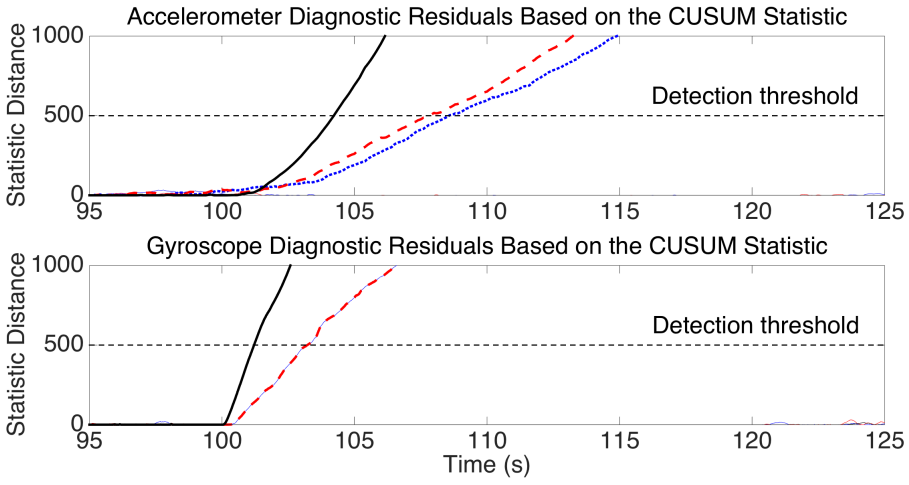

Figure 4.9: Diagnostic residual generated by CUSUM: simultaneous sensor faults.

reasonably close to its actual value.

CASE OF SIMULTANEOUS FAULTS

The case of simultaneous accelerometer and gyroscope faults is also considered. Specifically, at time $t = 100s$, biases $b_a = [0.15,\ 0.2,\ 0.75]^T m/s^2$ and $b_\omega = [5,\ -7,\ -10]^T$ $^\circ/s$ are injected into accelerometer and gyroscope measurements, respectively. Figure 4.9 shows the statistic property generated by the CUSUM test. As can be seen, shortly after the occurrence of the faults, the test statistics corresponding to both diagnostic estimators, exceed their respective detection thresholds. Therefore, it can be concluded that faults have occurred in both accelerometer and gyroscope measurements. Furthermore, Figure 4.10 and Figure 4.11 show the estimation of the accelerometer and gyroscope biases, respectively. As can be seen, estimation results are satisfactory.

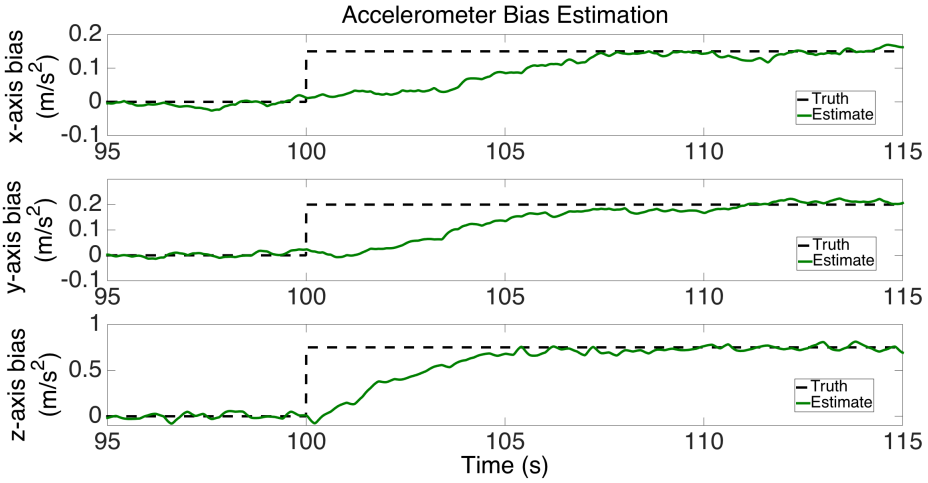

Figure 4.10: Accelerometer bias estimation in the simultaneous fault occurrence scenario.

CONCLUSION

In this chapter, the design, analysis, and real-time experimental results of a nonlinear fault diagnostic method for sensor bias faults in accelerometer and gyroscope measurements of quadrotor UAVs is presented. Based on the idea that accelerometer and gyroscope measurements coincide with translational forces and rotational and moments acting on the UAV body frame, respectively, two FDI estimators are designed to generate structured residuals for fault detection and isolation. In addition, nonlinear adaptive estimation schemes are developed to provide an estimate of the sensor bias.

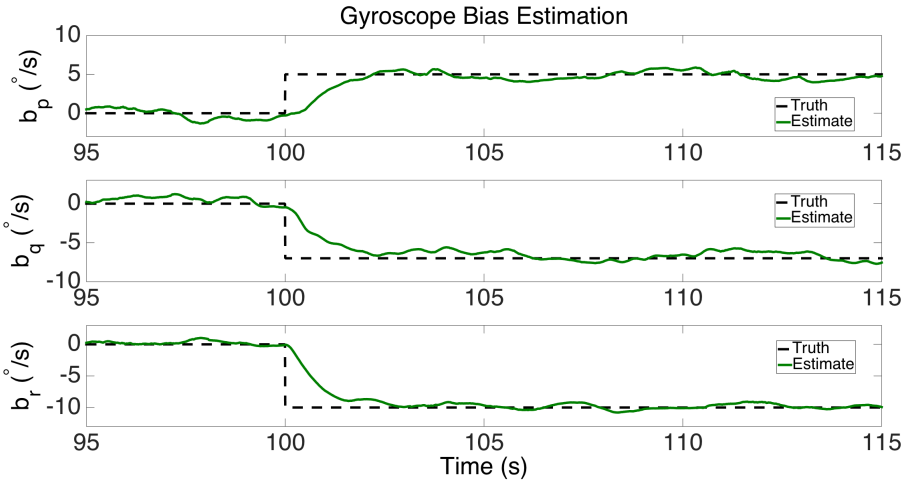

Figure 4.11: Gyroscope bias estimation in the simultaneous fault occurrence scenario.

The proposed diagnostic method is implemented on a quadrotor UAV test environment and demonstrated during real-time autonomous flight.

V. QUADROTOR SENSOR FAULT DIAGNOSIS WITH ESTIMATED ROLL & PITCH ANGLES

INTRODUCTION

In the previous chapter, a sensor fault diagnosis method for gyroscope and accelerometer faults of quadrotor UAVs was developed based on a critical assumption that roll and pitch angles are available for measurement. In real-world practical applications, the roll and pitch angles are often not directly measured and have to be estimated using on-board IMU signals that are prone to sensor faults. Results from the previous chapter are signficantly extended by developing a sensor fault diagnosis scheme without this critical assumption and demonstrating its effectiveness through experimental results obtained using a real-time quadrotor test environment. The presented sensor fault diagnosis method consists of the following three main components: 1) *a quadrotor roll and pitch angles estimator* designed using a general sliding-mode observer (SMO) methodology [48]. The attitude estimation algorithm uses only accelerometer measurements and is not affected by gyroscope sensor faults; 2) *a fault detection and isolation scheme* for detecting and isolating multiple simultaneous gyroscope and accelerometer sensor bias faults; 3) *two nonlinear fault parameter estimators* for providing an estimate of the unknown sensor bias magnitude, which are activated after the faulty sensor measurements are detected and isolated.

The main contributions of this chapter are the design, analysis, and experimental demonstration of a sensor fault diagnosis scheme for detecting, isolating, and estimating multiple simultaneous sensor bias faults in the gyroscope and accelerometer measurements of quadrotor UAVs in the absence of attitude angle measurements. Based on the quadrotor dynamics and sensor models under consideration, the effects of sensor faults are represented as virtual faults in the quadrotor state equation. Structured residuals are designed, allowing the detection and isolation of multiple simultaneous sensor faults under consideration. The stability and estimation performance properties of the presented nonlinear estimation algorithms, including the SMO-based quadrotor attitude estimator and the nonlinear fault magnitude estimators, are established using the Lyapunov synthesis method. In order to evaluate the fault diagnosis scheme, sensor bias faults are injected into the accelerometer and gyroscope measurements while the quadrotor is airborne. Angle estimation and sensor diagnosis results are obtained in real-time using

the quadrotor flight test environment. The experimental results for evaluating the fault diagnosis scheme are shown to illustrate its effectiveness.

PROBLEM FORMULATION

NOMINAL SYSTEM MODEL AND MODELING UNCERTAINTY

Recall the quadrotor nominal system dynamics:

$$\dot{p}_E = v_E \tag{5.1}$$

$$\dot{v}_E = \frac{1}{m} R_{EB}(\eta) \left(\begin{bmatrix} 0 \\ 0 \\ -U \end{bmatrix} - c_{\mathbf{d}} v_B \right) + \begin{bmatrix} 0 \\ 0 \\ g \end{bmatrix} \tag{5.2}$$

$$\dot{\eta} = R_\eta(\phi, \theta)\omega \tag{5.3}$$

$$\dot{\omega} = \begin{bmatrix} \frac{J_y - J_z}{J_x} qr \\ \frac{J_z - J_x}{J_y} pr \\ \frac{J_x - J_y}{J_z} pq \end{bmatrix} + \begin{bmatrix} \frac{1}{J_x}\tau_\phi \\ \frac{1}{J_y}\tau_\theta \\ \frac{1}{J_z}\tau_\psi \end{bmatrix} \tag{5.4}$$

where the system states and parameters have been defined in Chapter 3.

The vehicle velocity v_E described in (5.2) is expressed relative to the inertial frame. Alternatively, as in [10, 11, 17], by assuming that the Coriolis effect is small enough to be negligible, the quadrotor translational velocity dynamics relative to the body frame are

$$\begin{bmatrix} \dot{v}_u \\ \dot{v}_v \\ \dot{v}_w \end{bmatrix} = \frac{1}{m} \left(\begin{bmatrix} 0 \\ 0 \\ -U \end{bmatrix} - c_{\mathbf{d}} v_B \right) + \begin{bmatrix} -g \sin\theta \\ g \sin\phi \cos\theta \\ g \cos\phi \cos\theta \end{bmatrix} \tag{5.5}$$

where $v_B \triangleq [v_u,\, v_v,\, v_w]^T$ represents the velocities along the body $x-$, $y-$ and $z-$directions.

The quadrotor nominal model described by (5.1)-(5.4) assumes the absence of modeling uncertainty. In practical quadrotor applications, the system input variables, including the thrust U in (5.2) and rotational torques (i.e., τ_ϕ, τ_θ, and τ_ψ) in (5.4), are not measured and have to be estimated. It is often assumed that the thrust and torque produced by a propeller is proportional to the square of the motor angular velocity [10]. However, for most practical quadrotor applications, the motor velocities are not measured and need to be estimated based on the battery voltage and the pulse

width modulation (PWM) commands sent to the motors. Thus, errors in the motor velocity estimation, thrust and torque coefficients, along with the natural degradation of the propelling system and the battery, can cause uncertainties in the estimation of thrust and torques. Based on these observations, the nominal system model (5.1)-(5.4) is augmented to include modeling uncertainties arising from thrust and torque estimation. Specifically, we consider

$$\dot{p}_E = v_E \tag{5.6}$$

$$\dot{v}_E = \frac{1}{m} R_{EB}(\eta) \left(\begin{bmatrix} 0 \\ 0 \\ -U + \varrho_U \end{bmatrix} - c_{\mathbf{d}} v_B \right) + \begin{bmatrix} 0 \\ 0 \\ g \end{bmatrix} \tag{5.7}$$

$$\dot{\eta} = R_\eta(\phi, \theta)\omega \tag{5.8}$$

$$\dot{\omega} = \begin{bmatrix} \frac{J_y - J_z}{J_x} qr \\ \frac{J_z - J_x}{J_y} pr \\ \frac{J_x - J_y}{J_z} pq \end{bmatrix} + \begin{bmatrix} \frac{1}{J_x}\tau_\phi \\ \frac{1}{J_y}\tau_\theta \\ \frac{1}{J_z}\tau_\psi \end{bmatrix} + \begin{bmatrix} \varrho_\omega^1 \\ \varrho_\omega^2 \\ \varrho_\omega^3 \end{bmatrix} \tag{5.9}$$

where ϱ_U, ϱ_ω^1, ϱ_ω^2, and ϱ_ω^3 represent the modeling uncertainties as a result of the inaccuracy in thrust and torque estimation, respectively.

Assumption 5.1. The modeling uncertainties ϱ_U, ϱ_ω^1, ϱ_ω^2, and ϱ_ω^3 in (5.6) - (5.9) are time-varying and unknown, but assumed to be bounded by some known functions, i.e.:

$$|\varrho_U(t)| \leq \bar{\varrho}_U(\varphi, v_b, t),$$
$$|\varrho_\omega^1(t)| \leq \bar{\varrho}_\omega^1(\varphi, v_b, t),$$
$$|\varrho_\omega^2(t)| \leq \bar{\varrho}_\omega^2(\varphi, v_b, t),$$
$$|\varrho_\omega^3(t)| \leq \bar{\varrho}_\omega^3(\varphi, v_b, t),$$

where φ and v_b represent the motors' PWM signals and the battery voltage, respectively.

Remark 5.1: Assumption 5.1 characterizes the class of modeling uncertainties under consideration. The bounds on the modeling uncertainties are needed for deriving adaptive FDI threshold to distinguish between the effects of faults and modeling uncertainties [49].

SENSOR FAULT MODEL

The quadrotor accelerometer and gyroscope MEMS sensors, measuring forces and moments acting in the body frame, are susceptible to bias faults as a result of component damage, degradation, and temperature variations, etc. In this research, the following accelerometer and gyroscope sensor models are considered:

$$y_a(t) = a(t) \; + \; \beta_a(t - t_a) b_a \; = \; a(t) + \beta_a(t - t_a) \begin{bmatrix} b_u \\ b_v \\ b_w \end{bmatrix} \tag{5.10}$$

$$y_\omega(t) = \omega(t) + \beta_\omega(t - t_\omega) b_\omega \; = \; \begin{bmatrix} p \\ q \\ r \end{bmatrix} + \beta_\omega(t - t_\omega) \begin{bmatrix} b_p \\ b_q \\ b_r \end{bmatrix} \tag{5.11}$$

where $y_a(t) \in \mathbb{R}^3$ and $a(t) \in \mathbb{R}^3$ are the actual and healthy accelerometer measurements, respectively, $y_\omega(t) \in \mathbb{R}^3$ and $\omega(t)$ (see (5.4)) are the actual and healthy gyroscope measurements, respectively, and $b_a \stackrel{\triangle}{=} [b_u, b_v, b_w]^T$ and $b_\omega \stackrel{\triangle}{=} [b_p, b_q, b_r]^T$ represent the sensor bias faults in the three axis accelerometer and gyroscope measurements, respectively. Note that the healthy accelerometer measurement is given by (see (5.7))

$$a(t) = \frac{1}{m} \left(\begin{bmatrix} 0 \\ 0 \\ -U + \varrho_U(t) \end{bmatrix} - c_{\mathbf{d}} v_B(t) \right). \tag{5.12}$$

Additionally, $\beta_a(\cdot)$ and $\beta_\omega(\cdot)$ are fault time profile functions with unknown fault occurrence times t_a and t_ω, respectively. In this research, they are assumed to be step functions given by

$$\beta_a(t - t_a) = \begin{cases} 0 \, , & \text{when } t < t_a \\ 1 \, , & \text{when } t \geq t_a \end{cases} \tag{5.13}$$

$$\beta_\omega(t - t_\omega) = \begin{cases} 0 \, , & \text{when } t < t_\omega \\ 1 \, , & \text{when } t \geq t_\omega \, . \end{cases} \tag{5.14}$$

As in the previous chapter, the following assumption is made regarding the sensor faults:

Assumption 5.2. Each component of the unknown sensor biases b_a and b_w described by (5.10) and (5.11) is assumed to be constant and bounded, i.e.,

$$|b_u| \leq \bar{b}_u, \quad |b_v| \leq \bar{b}_v, \quad |b_w| \leq \bar{b}_w \tag{5.15}$$

$$|b_p| \leq \bar{b}_p, \quad |b_q| \leq \bar{b}_q, \quad |b_r| \leq \bar{b}_r \ . \tag{5.16}$$

Remark 5.2: It is worth noting that, in practical applications, after the occurrence of an accelerometer or gyroscope sensor bias fault, its magnitude may grow slowly over time. However, the change in the bias magnitude is often small over a short time period [43]. Therefore, the bias may be assumed to be constant during the short time period under consideration.

In addition, the position in the Earth frame and the yaw angle are considered to be available for measurement. Hence, the output equation for the quadrotor system model (5.6) - (5.9) is:

$$y(t) = [y_a^T(t),\, y_\omega^T(t),\, p_E^T(t),\, \psi(t)]^T. \tag{5.17}$$

Remark 5.3: The position measurements p_E in (5.17) can be obtained by a GPS unit in the case of out-door flight or by a camera-based motion capture system in the case of in-door flight. The yaw angle ψ can be obtained from an auxiliary device (e.g. magnetometer), independently of accelerometer and gyroscope measurements.

The objective of this research is to detect and isolate the possible occurrence of multiple simultaneous accelerometer and gyroscope sensor faults and to provide an estimate of the unknown fault magnitude for the nonlinear uncertain quadrotor system described by (5.6) - (5.9), (5.10), (5.11), and (5.17). It is worth noting that, most of the quadrotor sensor FDI results reported in literature are based on the assumption of single fault occurrence [9, 12–14]. In this research, the case of possible multiple simultaneous faults in all six components of the accelerometer and gyroscope measurements are considered (i.e., b_p, b_q, b_r, b_u, b_v, and b_w). Additionally, unlike in [9, 11, 14, 20, 50], the roll and pitch angles are not assumed to be measured in this research, which makes the sensor fault diagnosis problem even more challenging.

FAULT DIAGNOSIS ARCHITECTURE

As shown in Figure 5.1, the proposed senor fault diagnosis architecture consists of three main components: (1) roll and pitch angles estimation; (2) fault detection and isolation; (3) estimation of unknown fault magnitude. The controller signal, sensor measurements, and estimated roll and pitch angles serve as inputs to the fault detection, isolation, and estimation algorithms. Under normal operating conditions, two FDI estimators monitor the quadrotor system for detecting and isolating faults in the accelerometer and gyroscope measurements. Once a sensor fault is detected and isolated, the corresponding nonlinear adaptive estimator is activated for estimating the unknown sensor bias. The estimated sensor bias provided by the diagnostic algorithm can possibly be used to enhance the fault-tolerance capability of the closed-loop flight control system. In the following sections, we detail the algorithms for attitude estimation, fault detection and isolation, and fault magnitude estimation.

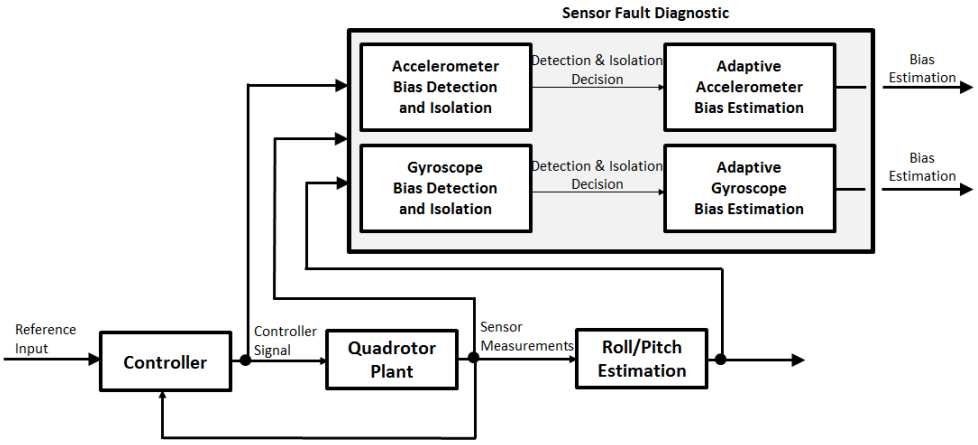

Figure 5.1: Fault diagnosis architecture.

ESTIMATION OF ROLL AND PITCH ANGLES

Attitude angles play an important role in the control of small UAVs. In practical applications, due to limited payload and prohibitive environmental conditions, UAV attitude angles are often not directly measured, and need to be estimated from related sensor measurements. In this section, we present an algorithm for estimating quadrotor roll and pitch angles by using a sliding-mode observer based general methodology for unknown input estimation [48].

Let y_u and y_v be the translational acceleration measurements of the quadrotor in the body frame $x-$ and $y-$ directions, respectively. Then, by using (5.10) and (5.12), we have

$$\begin{aligned} y_u &= -\frac{c_{\mathbf{d}}}{m} v_u + \beta_a b_u \\ y_v &= -\frac{c_{\mathbf{d}}}{m} v_v + \beta_a b_v \,. \end{aligned} \tag{5.18}$$

By taking the time derivative of y_u and y_v in (5.18) and using (5.5), we obtain

$$\begin{aligned} \dot{y}_u &= -\frac{c_{\mathbf{d}}}{m} \left(-\frac{c_{\mathbf{d}}}{m} v_u - g \sin\theta \right) \\ &= -\frac{c_{\mathbf{d}}}{m} y_u + \frac{c_{\mathbf{d}} g}{m} \sin\theta + \frac{c_{\mathbf{d}}}{m} \beta_a b_u \,, \end{aligned} \tag{5.19}$$

and

$$\begin{aligned} \dot{y}_v &= -\frac{c_{\mathbf{d}}}{m} \left(-\frac{c_{\mathbf{d}}}{m} v_v + g \sin\phi \cos\theta \right) \\ &= -\frac{c_{\mathbf{d}}}{m} y_v - \frac{c_{\mathbf{d}} g}{m} \sin\phi \cos\theta + \frac{c_{\mathbf{d}}}{m} \beta_a b_v \,. \end{aligned} \tag{5.20}$$

It can be seen that the sinusoidal terms appearing in (5.19) and (5.20) can possibly be treated as unknown inputs to the system dynamics and estimated online. In this research, by applying the sliding-mode observer technique presented in [48] for unknown input estimation, the following estimators are chosen as:

$$\dot{\hat{y}}_u = -\sigma(\hat{y}_u - y_u) - \frac{c_{\mathbf{d}}}{m} y_u + \zeta_u \tag{5.21}$$

$$\dot{\hat{y}}_v = -\sigma(\hat{y}_v - y_v) - \frac{c_{\mathbf{d}}}{m} y_v + \zeta_v \,, \tag{5.22}$$

where $\hat{y}_u$ and $\hat{y}_v$ are the estimates for y_u and y_v, respectively, σ is a positive design constant, ζ_u and ζ_v are the nonlinear injection signals [48]. Let us define the acceleration estimation errors as $\tilde{y}_u \triangleq y_u - \hat{y}_u$ and $\tilde{y}_v \triangleq y_v - \hat{y}_v$, respectively. Then, the nonlinear injection signals are designed as

$$\zeta_u = \rho_u \operatorname{sgn}(\tilde{y}_u) \tag{5.23}$$

$$\zeta_v = \rho_v \operatorname{sgn}(\tilde{y}_v) \,, \tag{5.24}$$

where $\operatorname{sgn}(\cdot)$ represents the signum function, and the design constants ρ_u and ρ_v are

chosen to satisfy

$$\rho_u \geq \left| \frac{c_{\mathbf{d}} g}{m} \left(\sin\theta + \frac{b_u}{g} \right) \right| + \xi_u \tag{5.25}$$

$$\rho_v \geq \left| \frac{c_{\mathbf{d}} g}{m} \left(-\sin\phi\cos\theta + \frac{b_v}{g} \right) \right| + \xi_v \,, \tag{5.26}$$

with ξ_u and ξ_v being some small positive constants. By using (5.19)-(5.22), it can be shown the acceleration estimation error dynamics is given by

$$\dot{\tilde{y}}_u = -\sigma \tilde{y}_u + \frac{c_{\mathbf{d}} g}{m} \sin\theta + \frac{c_{\mathbf{d}}}{m} \beta_a b_u - \zeta_u \tag{5.27}$$

$$\dot{\tilde{y}}_v = -\sigma \tilde{y}_v - \frac{c_{\mathbf{d}} g}{m} \sin\phi\cos\theta + \frac{c_{\mathbf{d}}}{m} \beta_a b_v - \zeta_v. \tag{5.28}$$

Next, we analyze the estimation error $\tilde{y}_u$ described by (5.27). Note that the estimation error $\tilde{y}_v$ in (5.28) is independent of $\tilde{y}_u$ and can be analyzed in an analogous manner. Specifically, let $V = \frac{1}{2}\tilde{y}_u^2$ be a Lyapunov function candidate. By using (5.23), the time derivative of V along the solution of (5.27) satisfies

$$\begin{aligned} \dot{V} &= -\sigma \tilde{y}_u^2 + \tilde{y}_u \left(\frac{c_{\mathbf{d}} g}{m} \sin\theta + \frac{c_{\mathbf{d}}}{m} \beta_a b_u - \zeta_u \right) \\ &\leq \tilde{y}_u \left(\frac{c_{\mathbf{d}} g}{m} \sin\theta + \frac{c_{\mathbf{d}}}{m} \beta_a b_u \right) - \tilde{y}_u \zeta_u \qquad (5.29) \\ &\leq |\tilde{y}_u| \left| \frac{c_{\mathbf{d}} g}{m} \sin\theta + \frac{c_{\mathbf{d}}}{m} \beta_a b_u \right| - \tilde{y}_u \rho_u \operatorname{sgn}(\tilde{y}_u) \,. \qquad (5.30) \end{aligned}$$

Using $|\tilde{y}_u| = \tilde{y}_u \operatorname{sgn}(\tilde{y}_u)$, we obtain

$$\dot{V} \leq -|\tilde{y}_u| \left(\rho_u - \left| \frac{c_{\mathbf{d}} g}{m} \sin\theta + \frac{c_{\mathbf{d}}}{m} \beta_a b_u \right| \right) .$$

By choosing ρ_u such that (5.25) is satisfied, it follows that:

$$\dot{V} \leq -\xi_u |\tilde{y}_u| \leq -\xi_u \sqrt{2V} \,. \tag{5.31}$$

Note that (5.31) provides the reachability condition for the sliding motion [51]. During the sliding motion, due to the finite switching frequency of the signal ζ_u in (5.23), we have $\tilde{y}_u \approx 0$ and $\dot{\tilde{y}}_u \approx 0$. Therefore, from (5.27), by assuming the variation of the pitch

angle θ is much slower than the switching frequency of the signal ζ_u, we obtain:

$$0 \approx \frac{c_{\mathbf{d}} g}{m} \sin\theta + \frac{c_{\mathbf{d}}}{m} \beta_a b_u - \zeta_{ueq} \,, \tag{5.32}$$

where ζ_{ueq} is the equivalent output error injection signal required to maintain the sliding motion and represents the average behavior of the discontinuous component ζ_u defined in (5.23). As described in [51], the equivalent output error injection signal ζ_{ueq} can be recovered by the use of a low pass filter :

$$\zeta_{ueq} \approx \frac{\delta}{s+\delta} \rho_u \,, \tag{5.33}$$

where δ is a positive design constant. Thus, the unknown sinusoidal term in (5.32) can be estimated as:

$$\sin\theta \approx \frac{m}{c_{\mathbf{d}} g} \zeta_{ueq} - \frac{\beta_a b_u}{g} \,. \tag{5.34}$$

By applying a similar reasoning logic to (5.20), (5.22), (5.24) and (5.26), the sinusoidal term in (5.28) can be estimated as

$$\sin\phi\cos\theta \approx -\frac{m}{c_{\mathbf{d}} g} \zeta_{veq} + \frac{\beta_a b_v}{g} \,, \tag{5.35}$$

where the equivalent output error injection signal ζ_{veq} is obtained by low pass filtering the discontinuous signal ζ_v given by (5.24) [51]. Therefore, by using (5.34) and (5.35), in the absence of accelerometer faults (i.e. $b_u = 0$ and $b_v = 0$ for $0 \leq t < t_a$), an estimation of roll and pitch angles can be generated by

$$\hat{\theta} \approx \sin^{-1}\left(\frac{m}{c_{\mathbf{d}} g} \zeta_{ueq}\right) \tag{5.36}$$

$$\hat{\phi} \approx \sin^{-1}\left(-\frac{m}{c_{\mathbf{d}} g \cos\hat{\theta}} \zeta_{veq}\right) \,. \tag{5.37}$$

Based on the above analysis, it can be seen that, in the absence of accelerometer faults, roll and pitch angle estimations $\hat{\theta}$ and $\hat{\phi}$ converge closely to their actual values in some finite time $t_s > 0$.

Remark 5.4: The problem of quadrotor attitude angle estimation has been extensively investigated in literature. Many existing methods require the use of gyroscope measurements and/or translational position measurements. The algorithm presented in this

research is independent of these measurements and the associated sensor faults. Specifically, it only uses the acceleration signals in the body $x-$ and $y-$ directions. Note that it is very difficult to apply a Kalman filter based method for simultaneous estimation of quadrotor attitude and sensor bias by only using acceleration signals, because the extra system states, introduced to represent the three components of the unknown accelerometer sensor bias, make it very difficult to satisfy the observability condition, unless more sensor measurements are added.

Remark 5.5: As shown in the analysis given above, the roll and pitch angle estimates $\hat{\theta}$ and $\hat{\phi}$ converge to their actual values in finite time, in the absence of accelerometer sensor faults. After the occurrence of such faults, as can be seen from (5.34) and (5.35), the effects of accelerometer measurement bias on attitude estimation are significantly reduced due to the division by the gravitational constant g (note that the sensor bias b_u and b_v are often much smaller than g). It is also worth noting that the thresholds for sensor FDI is designed based on the healthy system model, that is, it is guaranteed that the diagnostic residuals remain below the thresholds in the absence of faults, ensuring robustness of the FDI algorithm. After the occurrence of sensor faults, the diagnostic residuals will be affected and take significantly non-zero values, allowing successful FDI.

FAULT DETECTION AND ISOLATION

This section presents the FDI method for sensor faults in accelerometer and gyroscope measurements. Let us define the gyroscope measurement y_ω given in (5.11) as $y_\omega \triangleq [y_p,\ y_q,\ y_r]^T$. By substituting the sensor models (5.10)-(5.11) into the systems dynamics (5.6)-(5.9), we obtain

$$\dot{p}_E = v_E \tag{5.38}$$

$$\dot{v}_E = R_{EB}(\eta) y_a + \begin{bmatrix} 0 \\ 0 \\ g \end{bmatrix} - R_{EB}(\eta)\beta_a b_a \tag{5.39}$$

$$\dot{\eta} = R_\eta(\phi,\theta) y_\omega - R_\eta(\phi,\theta)\beta_\omega b_\omega \tag{5.40}$$

$$\dot{\omega} = \begin{bmatrix} \frac{J_y - J_z}{J_x}(y_q - \beta_\omega b_q)(y_r - \beta_\omega b_r) \\ \frac{J_z - J_x}{J_y}(y_r - \beta_\omega b_r)(y_p - \beta_\omega b_p) \\ \frac{J_x - J_y}{J_z}(y_p - \beta_\omega b_p)(y_q - \beta_\omega b_q) \end{bmatrix} + \begin{bmatrix} \frac{1}{J_x}\tau_\phi \\ \frac{1}{J_y}\tau_\theta \\ \frac{1}{J_z}\tau_\psi \end{bmatrix} + \begin{bmatrix} \varrho_\omega^1 \\ \varrho_\omega^2 \\ \varrho_\omega^3 \end{bmatrix}. \tag{5.41}$$

As can be seen from (5.38)-(5.41), the inertial position and velocity states (i.e., p_E and v_E) are only affected by the bias in accelerometer measurements, while the angular rates states are only affected by gyroscope measurements. Based on this observation, it follows naturally to also divide the fault diagnosis tasks for these two types of sensor faults.

ACCELEROMETER FAULT DIAGNOSTIC ESTIMATOR

The UAV position and inertial velocity dynamics given by (5.38) and (5.39) can be put into the following form:

$$\begin{aligned} \dot{x} &= Ax + f(\phi, \theta, \psi, y_a) + G_a(\eta)\beta_a b_a \\ y &= Cx\,, \end{aligned} \tag{5.42}$$

where $x = [p_E^T\,, v_E^T]^T$, $y = p_E$,

$$A = \begin{bmatrix} 0_{3\times3} & I_3 \\ 0_{3\times3} & 0_{3\times3} \end{bmatrix}, \quad f(\phi, \theta, \psi, y_a) = \begin{bmatrix} 0_{3\times1} \\ R_{EB}y_a + \begin{bmatrix} 0 \\ 0 \\ g \end{bmatrix} \end{bmatrix} \tag{5.43}$$

$G_a(\eta) = [0_{3\times3}\,, -R_{EB}^T]^T$, $C = [I_3,\, 0_{3\times3}]$, I_3 is a 3×3 identity matrix, $0_{3\times3}$ is a 3×3 matrix with all entries zero, and $0_{3\times1}$ is a 3×1 zero vector. The following fault diagnostic observer is chosen:

$$\begin{aligned} \dot{\hat{x}} &= A\hat{x} + f(\hat{\phi}, \hat{\theta}, \psi, y_a) + L_0(y - \hat{y}) \\ \hat{y} &= C\hat{x}\,, \end{aligned} \tag{5.44}$$

where $\hat{x} \in \mathbb{R}^6$ represents the position and inertial velocity estimation, $\hat{y} \in \mathbb{R}^3$ is the estimated position, $\hat{\phi}$ and $\hat{\theta}$ are the estimated roll and pitch angles generated by (5.36)-(5.37), and L_0 is a design matrix. Clearly (A, C) is an observable pair. Therefore, the matrix L_0 can always be designed such that the matrix $\bar{A} \triangleq A - L_0C$ is asymptotically

stable. Let us define the state estimation error as $\tilde{x} \triangleq x - \hat{x}$ and the quadrotor position estimation error as $\tilde{y}_p \triangleq y - \hat{y}$. From (5.42) and (5.44), it follows that

$$\begin{aligned} \dot{\tilde{x}} &= \bar{A}\tilde{x} + \Delta f \cdot y_a + G_a(\eta)\beta_a b_a \\ \tilde{y}_p &= C\tilde{x}\,, \end{aligned} \tag{5.45}$$

where the matrix

$$\Delta f \triangleq \begin{bmatrix} 0_{3\times 3} \\ R_{EB}(\phi,\theta,\psi) - R_{EB}(\hat{\phi},\hat{\theta},\psi) \end{bmatrix}.$$

As previously shown, in the absence of an accelerometer bias fault (i.e. for $0 \leq t < t_a$), the estimated roll and pitch angles converge to the true attitude angles in finite time, which implies that $\Delta f \to 0$ in finite time. Thus, a bound $\bar{f}$ can be found such that

$$|\Delta f| \leq \bar{f}(\hat{\phi},\, \hat{\theta}, \psi)\,. \tag{5.46}$$

By using (5.45), (5.46), and the triangular inequality, it can be shown that, in the absence of accelerometer bias, for $j = 1,\, 2,\, 3$, the $j-$th component of the output estimation error $\tilde{y}_p$ satisfies

$$\begin{aligned} |\tilde{y}_p^j| &\leq \left| C_j e^{\bar{A}t}\tilde{x}(0) + C_j \int_0^t e^{\bar{A}(t-\tau)}\Delta f\, y_a d\tau \right| \\ &\leq |C_j e^{\bar{A}t}||\tilde{x}(0)| + \int_0^t \left|C_j e^{\bar{A}(t-\tau)}\right| |\Delta f\, y_a| d\tau \\ &\leq k_a^j e^{-\lambda_a^j t}\bar{x}_0 + k_a^j \int_0^t e^{-\lambda_a^j(t-\tau)}\bar{f}(\hat{\phi},\, \hat{\theta},\psi)\,|y_a(\tau)|\,d\tau \end{aligned} \tag{5.47}$$

where C_j represents the $j-$th row of C, $\bar{x}(0), k_a^j$ and λ_a^j are positive constants chosen such that $|\tilde{x}(0)| \leq \bar{x}(0)$ and $|C_j e^{\bar{A}t}| \leq k_a^j e^{-\lambda_a^j t}$ (Note that since $\bar{A}$ is asymptotically stable, such constants k_a^j and λ_a^j always exist [45]).

Therefore, in the absence of an accelerometer bias fault, we have: for $j = 1,\, 2,\, 3$, $|\tilde{y}_p^j| \leq \mu_a^j(t)$, where the accelerometer FDI thresholds $\mu_a^j(t)$ are given by

$$\mu_a^j(t) \triangleq k_a^j e^{-\lambda_a^j t}\bar{x}_0 + k_a^j \int_0^t e^{-\lambda_a^j(t-\tau)}\bar{f}(\hat{\phi},\, \hat{\theta},\psi)\,|y_a(\tau)|\,d\tau\,. \tag{5.48}$$

In addition, as can be seen from (5.45), the diagnostic residual $\tilde{y}_p$ is only sensitive to accelerometer sensor fault b_a. Therefore, in the fault diagnosis procedure, if any com-

ponent of the position estimation error $\tilde{y}_p$ exceeds its corresponding threshold given by (5.48), it can be concluded that a fault in the accelerometer measurement has occurred.

Remark 5.6: Note that the bound $\mu_a^j(t)$ described by (5.48) represents an adaptive threshold, which has obvious advantage over a fixed threshold [6]. Additionally, the adaptive threshold $\mu_a^j(t)$ can be easily implemented using linear filtering techniques [49].

GYROSCOPE FAULT DIAGNOSTIC ESTIMATOR

By expanding the dynamics of the angular rates described by (5.41) and noting that $\beta_\omega = \beta_\omega^2$ (see (5.14)), we obtain

$$\begin{bmatrix} \dot{p} \\ \dot{q} \\ \dot{r} \end{bmatrix} = \bar{J} \begin{bmatrix} y_q y_r \\ y_r y_p \\ y_p y_q \end{bmatrix} + J^{-1} \begin{bmatrix} \tau_\phi \\ \tau_\theta \\ \tau_\psi \end{bmatrix} + \begin{bmatrix} \varrho_\omega^1 \\ \varrho_\omega^2 \\ \varrho_\omega^3 \end{bmatrix} + \bar{J}\beta_\omega \left(\begin{bmatrix} 0 & -y_r & -y_q \\ -y_r & 0 & -y_p \\ -y_q & -y_p & 0 \end{bmatrix} \begin{bmatrix} b_p \\ b_q \\ b_r \end{bmatrix} + \begin{bmatrix} b_q b_r \\ b_r b_p \\ b_p b_q \end{bmatrix} \right), \tag{5.49}$$

where $J = \text{diag}\{J_x\,, J_y\,, J_z\}$ is the moment of inertia matrix, and

$$\bar{J} = \text{diag}\left\{ \frac{J_y - J_z}{J_x}, \frac{J_z - J_x}{J_y}, \frac{J_x - J_y}{J_z} \right\}.$$

Based on (5.49), the gyroscope sensor bias diagnostic estimator is designed as

$$\dot{\hat{y}}_\omega = -\Psi \begin{bmatrix} \hat{y}_p - y_p \\ \hat{y}_q - y_q \\ \hat{y}_r - y_r \end{bmatrix} + \bar{J} \begin{bmatrix} y_q y_r \\ y_r y_p \\ y_p y_q \end{bmatrix} + J^{-1} \begin{bmatrix} \tau_\phi \\ \tau_\theta \\ \tau_\psi \end{bmatrix} \tag{5.50}$$

where $\hat{y}_\omega \triangleq [\hat{y}_p\,, \hat{y}_q\,, \hat{y}_r]^T$ represents an estimation of the gyroscope measurement y_ω given by (5.11), and $\Psi \triangleq \text{diag}\{\lambda_\omega^1,\, \lambda_\omega^2,\, \lambda_\omega^3\}$ is a diagonal positive definite design matrix.

Let the output estimation error be defined as $\tilde{y}_\omega = y_\omega - \hat{y}_\omega$. Then, based on (5.49) and (5.50), before the occurrence of a gyroscope senor fault (i.e. for $0 \leq t < t_\omega$), it follows that the gyroscope output estimation error dynamics satisfies

$$\dot{\tilde{y}}_\omega = -\Psi \tilde{y}_\omega + \begin{bmatrix} \varrho_\omega^1 \\ \varrho_\omega^2 \\ \varrho_\omega^3 \end{bmatrix}.$$

Therefore, based on Assumption 1, it can be easily shown that, for $j = 1, 2, 3$, the j-th component of the gyroscope output estimation error satisfies

$$|\tilde{y}_\omega^j| \leq \mu_\omega^j(t)\,, \tag{5.51}$$

where the threshold functions $\mu_\omega^j(t)$ is given by

$$\mu_\omega^j(t) \triangleq e^{-\lambda_\omega^j t}\bar{y}_{\omega 0}^j + \int_0^t e^{-\lambda_\omega^j(t-\tau)}\bar{\varrho}_\omega^j(\varphi, v_b, \tau)d\tau\,, \tag{5.52}$$

for some positive constants $\bar{y}_{\omega 0}^j$ satisfying $|\tilde{y}_\omega^j| \leq \bar{y}_{\omega 0}^j$. On the other hand, after the occurrence of a gyroscope sensor bias fault (i.e., for $t > t_\omega$), by using (5.49) and (5.50), it can be shown that the gyroscope output estimation error dynamics satisfies

$$\dot{\tilde{y}}_\omega = -\Psi\tilde{y}_\omega + \begin{bmatrix}\varrho_\omega^1\\ \varrho_\omega^2\\ \varrho_\omega^3\end{bmatrix} + \bar{J}\beta_\omega\left(\begin{bmatrix}0 & -y_r & -y_q\\ -y_r & 0 & -y_p\\ -y_q & -y_p & 0\end{bmatrix}\begin{bmatrix}b_p\\ b_q\\ b_r\end{bmatrix} + \begin{bmatrix}b_q b_r\\ b_r b_p\\ b_p b_q\end{bmatrix}\right). \tag{5.53}$$

As can be seen from (5.53), the residual $\tilde{y}_{\omega(t)}$ is only sensitive to the gyroscope bias b_ω.

From the above analysis, we conclude that each residual components $\tilde{y}_\omega^j(t)$ is guaranteed to remain below its threshold $\mu_\omega^j(t)$ in the absence of faults. Furthermore, in the fault diagnosis procedure, if at least one residual component $\tilde{y}_\omega^j(t)$ exceeds its threshold $\mu_\omega^j(t)$, it can be concluded that the gyroscope measurement is faulty.

FAULT DETECTION AND ISOLATION DECISION SCHEME

As described above, the diagnostic residuals $\tilde{y}_p$ (see (5.45)) and $\tilde{y}_\omega$ (see (5.53)) are only sensitive to accelerometer faults and gyroscope faults, respectively. Therefore, they can also be used as structured residuals for fault isolation. Specifically, we have the following FDI decision scheme:

- If all components of the residuals $\tilde{y}_p$ and $\tilde{y}_\omega$ remain below their thresholds, then the absence of faults is concluded.

- If all three components of the residual $\tilde{y}_\omega$ remain below their thresholds, and at least one component of the residual $\tilde{y}_p$ exceeds its corresponding threshold, then the occurrence of an accelerometer fault is determined.

- If all three components of the residual $\tilde{y}_p$ remain below their thresholds, and at least one component of the residual $\tilde{y}_\omega$ exceeds its threshold, then the occurrence of a gyroscope fault is determined.

- If both $\tilde{y}_p$ and $\tilde{y}_\omega$ have at least one component exceeding the corresponding thresholds, then we conclude that both gyroscope and accelerometer measurements are faulty.

SENSOR BIAS ESTIMATION

As shown in Figure 5.1, once a fault has been detected and isolated, the corresponding nonlinear bias estimator is activated to provide an estimation of the sensor fault, which can possibly be used for the purpose of fault accommodation and prognosis. In this section, we detail the design of nonlinear estimation schemes for sensor bias estimation. Note that the absence of roll and pitch angles measurements constitutes a significant departure from the previous results reported in [50], and the problem of sensor bias estimation becomes more challenging in this case.

ACCELEROMETER BIAS ESTIMATION

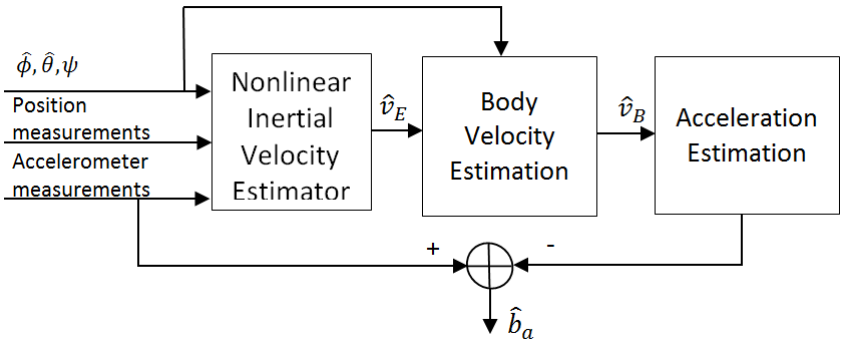

Figure 5.2: Accelerometer bias estimation.

As shown in Figure 5.2, the accelerometer bias estimation scheme consists of the following procedure:

i) Obtain the inertial velocity estimate $\hat{v}_E$.

ii) Obtain an estimate of the quadrotor velocity relative to the body frame, that is,

$$\hat{v}_B = R_{BE}(\hat{\phi}, \hat{\theta}, \psi)\hat{v}_E\,, \tag{5.54}$$

where $\hat{\phi}$ and $\hat{\theta}$ are the estimated roll and pitch angles provided by (5.37) and (5.36), respectively.

iii) By using (5.54) and the acceleration model given by (5.12), obtain an estimate of the acceleration acting on the quadrotor body, that is,

$$\hat{a} = \frac{1}{m}\left(\begin{bmatrix} 0 \\ 0 \\ -U \end{bmatrix} - c_{\mathbf{d}}\hat{v}_B\right). \tag{5.55}$$

iv) Use the accelerometer sensor measurement model (5.10) to obtain an estimate of the accelerometer bias as

$$\hat{b}_a = y_a - \hat{a}. \tag{5.56}$$

The details of the proposed algorithm are described below.

By using (5.6), (5.7), and the relationship between the inertial and body velocity $v_E = R_{EB}v_B$, we obtain

$$\dot{p}_E = v_E \tag{5.57}$$

$$\dot{v}_E = -\frac{c_{\mathbf{d}}}{m}v_E + \frac{1}{m}R_{EB}\begin{bmatrix} 0 \\ 0 \\ -U \end{bmatrix} + \begin{bmatrix} 0 \\ 0 \\ g \end{bmatrix} + \frac{1}{m}R_{EB}\begin{bmatrix} 0 \\ 0 \\ \varrho_U \end{bmatrix}. \tag{5.58}$$

The above equations can be put into the following state space form:

$$\begin{aligned} \dot{x} &= Ax + H(\phi,\theta,\psi) + N(\varrho_U,\phi,\theta,\psi) \\ y &= Cx \end{aligned} \tag{5.59}$$

where $x \triangleq [p_E^T, v_E^T]^T$ and $y \triangleq p_E$ represent the state and output vectors, respectively,

$$A = \begin{bmatrix} 0_{3\times3} & I_3 \\ 0_{3\times3} & -\frac{c_{\mathbf{d}}}{m}I_3 \end{bmatrix}, \quad N(\varrho_U,\phi,\theta,\psi) = \frac{\varrho_U}{m}\begin{bmatrix} 0_{3\times1} \\ R_{EB}^3 \end{bmatrix},$$

$$H(\phi,\theta,\psi) = \begin{bmatrix} 0_{3\times 1} \\ -\frac{U}{m}R^3_{EB} + \begin{bmatrix} 0 \\ 0 \\ g \end{bmatrix} \end{bmatrix},$$

$C = \begin{bmatrix} I_3 & 0_{3\times 3} \end{bmatrix}$, and R^3_{EB} is the third column of the rotation matrix R_{EB}. Clearly the pair (A, C) in (5.59) is observable. The following nonlinear observer is chosen for estimating the unknown inertial velocity:

$$\begin{aligned} \dot{\hat{x}} &= A\hat{x} + H(\hat{\phi},\hat{\theta},\psi) + L(y-\hat{y}) \\ \hat{y} &= C\hat{x}\,, \end{aligned} \tag{5.60}$$

where $\hat{x}$ and $\hat{y}$ represent the state estimation and output estimation, respectively, and L is a design matrix chosen such that the matrix $\bar{A} \triangleq A - LC$ is asymptotically stable. Letting $\tilde{x} \triangleq x - \hat{x}$ be the state estimation error, we have:

$$\dot{\tilde{x}} = \bar{A}\tilde{x} + \Delta H + N(\varrho_U,\phi,\theta,\psi)\,, \tag{5.61}$$

where

$$\begin{aligned} \Delta H &\triangleq H(\phi,\theta,\psi) - H(\hat{\phi},\hat{\theta},\psi) \\ &= -\frac{U}{m}\begin{bmatrix} 0_{3\times 1} \\ \tilde{R}^3_{EB}(\phi,\theta,\psi,\hat{\phi},\hat{\theta}) \end{bmatrix}, \end{aligned}$$

and $\tilde{R}^3_{EB} \triangleq R^3_{EB}(\phi,\theta,\psi) - R^3_{EB}(\hat{\phi},\hat{\theta},\psi)$. Since $\bar{A}$ in (5.61) is asymptotically stable by design, and ΔH and $N(\varrho_U,\phi,\theta,\psi)$ are bounded, it follows that $\tilde{x}$ is also bounded.

Let $T_a > t_a$ be the time instant when an accelerometer bias fault has been isolated by the FDI algorithm described in the previous Section. Therefore, for $t \geq T_a$, the inertial velocity estimation error $\tilde{v}_E \triangleq v_E - \hat{v}_E$ can be computed from (5.61) as

$$\tilde{v}_E(t) = C_1 e^{\bar{A}(t-T_a)}\tilde{x}(T_a) + C_1\int_{T_a}^{t} e^{\bar{A}(t-\tau)}\left(\Delta H + N\right)d\tau$$

where $\tilde{x}(T_a)$ is the state estimation error due to initial conditions, and $C_1 = [0_{3\times 3},\, I_3]$.

By using the triangular inequality, it then follows that

$$
\begin{aligned}
|\tilde{v}_E(t)| &\leq \int_{T_a}^{t} |C_1 e^{\bar{A}(t-\tau)}| \, (|\Delta H| + |N|) d\tau + |C_1 e^{\bar{A}(t-T_a)}| \, |\tilde{x}(T_a)| \\
&\leq \frac{\mu_0}{m} \int_{T_0}^{t} e^{-\beta_0 (t-\tau)} \left(U |\tilde{R}^3_{EB}| + \bar{\varrho}_U |R^3_{EB}| \right) d\tau + \mu_0 \, \bar{x}_a \, e^{-\beta_0 (t-T_a)}
\end{aligned} \tag{5.62}
$$

where μ_0 and β_0 are positive constants satisfying $|C_1 e^{\bar{A}t}| \leq \mu_0 e^{-\beta_0 t}$ (Note that since $\bar{A}$ is stable by design, such constants always exist [45]), and $\bar{x}_a$ is a bound on the initial state estimation error (i.e., $|\tilde{x}(T_a)| \leq \bar{x}_a$).

Let $\tilde{b}_a \triangleq b_a - \hat{b}_a$ be the accelerometer bias estimation error. Then, by using (5.10), (5.12) and (5.56), it can be shown that the bias estimation error is given by

$$
\begin{aligned}
\tilde{b}_a = (y_a - a) - \hat{b}_a &= \frac{c_{\mathbf{d}}}{m} (v_B - \hat{v}_B) - \begin{bmatrix} 0 \\ 0 \\ \frac{\varrho_U}{m} \end{bmatrix} \\
&= \frac{c_{\mathbf{d}}}{m} (R_{BE} v_E - \hat{R}_{BE} \hat{v}_E) - \begin{bmatrix} 0 \\ 0 \\ \frac{\varrho_U}{m} \end{bmatrix},
\end{aligned} \tag{5.63}
$$

where $R_{BE} = R^T_{EB}$, and $\hat{R}_{BE} \triangleq R_{BE}(\hat{\phi}, \hat{\theta}, \psi)$ represents the estimated body-to-Earth rotation matrix based on the estimated roll and pitch angles. By adding and subtracting $R_{BE} \hat{v}_E$ to (5.63) and by using Assumption 5.1, it can be shown that

$$
\begin{aligned}
|\tilde{b}_a| &\leq \frac{c_{\mathbf{d}}}{m} |R_{BE} v_E - \hat{R}_{BE} \hat{v}_E + R_{BE} \hat{v}_E - R_{BE} \hat{v}_E| + \frac{\bar{\varrho}_U}{m} \\
&\leq \frac{c_{\mathbf{d}}}{m} \|R_{BE}\| \, |\tilde{v}_E| + \frac{c_{\mathbf{d}}}{m} |\hat{v}_E| \, \|\Delta R_{BE}\| + \frac{\bar{\varrho}_U}{m}
\end{aligned} \tag{5.64}
$$

where $\Delta R_{BE} \triangleq R_{BE}(\phi, \theta, \psi) - R_{BE}(\hat{\phi}, \hat{\theta}, \psi)$.

Based on (5.62) and (5.64), the stability and estimation performance properties of the accelerometer bias estimation scheme can be summarized as follows:

Theorem 5.1 *In the presence of an accelerometer bias, the estimation scheme described by (5.54), (5.55), (5.56) and (5.60) guarantees that:*

(1) the state estimation error $\tilde{x}$ is bounded;

(2) the accelerometer bias estimation error satisfies

$$|\tilde{b}_a| \leq \frac{c_{\boldsymbol{d}}}{m}|\hat{v}_E|\,\|\Delta R_{BE}\| + \frac{\bar{\varrho}_U}{m} + \frac{c_{\boldsymbol{d}}}{m}\|R_{BE}\|\bar{v}_E$$

where

$$\bar{v}_E = \frac{\mu_0}{m}\int_{T_0}^{t} e^{-\beta_0(t-\tau)}\left(U|\tilde{R}^3_{EB}| + \bar{\varrho}_U|R^3_{EB}|\right)d\tau + \mu_0\,\bar{x}_a\,e^{-\beta_0(t-T_a)}\,.$$

Theorem 5.1 ensures the boundness of all signals in the estimation scheme. Additionally, it can be seen that the bias estimation performance is limited by various uncertainties entering the fault estimation problem, including the attitude angle estimation error represented by ΔR_{EB} and $\tilde{R}^3_{EB}$, the thrust estimation uncertainty $\bar{\varrho}_U$, and unknown initial conditions $\bar{x}_a$.

Remark 5.7: It is worth noting that the occurrence of an accelerometer bias will affect the accuracy of attitude angle estimation. However, as can be seen from (5.34) and (5.35), this effect is significantly reduced due to the division of the bias by the gravitational constant g. In addition, after a reasonable estimate of the sensor bias is obtained, it can possibly be used to to adjust the sensor measurement and improve the attitude angle estimation.

GYROSCOPE BIAS ESTIMATION

Once the occurrence of a gyroscope sensor fault is determined, an adaptive estimator is activated in order to estimate the bias in the gyroscope sensor. Specifically, based on (5.36)-(5.37) and (5.40), the following adaptive estimator is chosen:

$$\dot{\hat{\eta}}_e = -\Lambda(\hat{\eta}_e - \eta_e) + R_\eta(\hat{\phi},\hat{\theta})y_\omega - R_\eta(\hat{\phi},\hat{\theta})\hat{b}_\omega + \Omega\dot{\hat{b}}_\omega \tag{5.65}$$

$$\dot{\Omega} = -\Lambda\Omega - R_\eta(\hat{\phi},\hat{\theta}) \tag{5.66}$$

$$\dot{\hat{b}}_\omega = \Gamma\Omega^T(\eta_e - \hat{\eta}_e)\,, \tag{5.67}$$

where $\eta_e \triangleq [\hat{\phi}\,,\hat{\theta}\,,\psi]^T$, $\hat{\eta}_e$ represents an estimate of η_e, $\hat{b}_\omega$ is an estimate of the unknown b_ω, Λ and Γ are positive definite diagonal design matrices, and the filter (5.66) is needed to ensure the stability of the adaptive algorithm [38,39]. Note that, as described in the

previous Section, the presence of a gyroscope sensor fault does not affect the estimation of roll and pitch angles, that is, η_e converge to η in some finite time t_s. Without loss of generality, let $\Lambda = diag\{\lambda, \lambda, \lambda\}$, where $-\lambda < 0$ is the filter pole. The adaptive law (5.67) for updating the bias estimate $\hat{b}_\omega$ is derived using Lyapunov synthesis approach [45].

Suppose that a gyroscope sensor bias fault is detected and isolated at some time $T_\omega > t_\omega$. Let us define $\bar{T}_\omega \triangleq \max(T_\omega, t_s)$.The stability and estimation performance properties of the adaptive scheme given by (5.65) - (5.67) are described as follows:

Theorem 5.2 *In the presence of a gyroscope sensor bias, if there exist constants* $\alpha_0 > 0$, $T_0 > 0$ *and* $\alpha_1 > 0$, *such that* $\forall t \geq \bar{T}_\omega$,

$$\alpha_1 I \geq \frac{1}{T_0} \int_t^{t+T_0} \Omega^T \Omega d\tau \geq \alpha_0 I \,, \tag{5.68}$$

the adaptive estimation scheme described by (5.65) - (5.67) guarantees that:

1. *all the signals in the adaptive estimator remain bounded;*

2. *the gyroscope bias estimation error converges to zero.*

Proof. For $t \geq \bar{T}_\omega$, because the roll and pitch angle estimation error has converged to zero, we have $\eta_e = \eta$. Therefore, from (5.40), we obtain

$$\dot{\eta}_e = \dot{\eta} = R_\eta(\phi, \theta) y_\omega - R_\eta(\phi, \theta) b_\omega \,. \tag{5.69}$$

By defining $\tilde{\eta}_e \triangleq \eta_e - \hat{\eta}_e$ and using (5.69) and (5.65), the attitude estimation error dynamics are given by:

$$\dot{\tilde{\eta}}_e = -\Lambda \tilde{\eta}_e + (R_\eta(\phi, \theta) - R_\eta(\hat{\phi}, \hat{\theta})) y_\omega - R_\eta(\phi, \theta) b_\omega + R_\eta(\hat{\phi}, \hat{\theta}) \hat{b}_\omega - \Omega \dot{\hat{b}}_\omega. \tag{5.70}$$

Note that for $t \geq \bar{T}_\omega$, we have $R_\eta(\phi, \theta) = R_\eta(\hat{\phi}, \hat{\theta})$. Thus, (5.70) can be simplified as

$$\dot{\tilde{\eta}}_e = -\Lambda \tilde{\eta}_e + R_\eta(\hat{\phi}, \hat{\theta}) \tilde{b}_\omega - \Omega \dot{\hat{b}}_\omega \,, \tag{5.71}$$

where $\tilde{b}_\omega \triangleq \hat{b}_\omega - b_\omega$ represents the gyroscope bias estimation error. Substituting $R_\eta(\hat{\phi}, \hat{\theta}))$

$= -\dot{\Omega} - \Lambda\Omega$ (see (5.66)) into (5.71) and noting that $\dot{\hat{b}}_\omega = \dot{\tilde{b}}_\omega$, we obtain

$$\begin{aligned}\dot{\tilde{\eta}}_e &= -\Lambda\tilde{\eta}_e - \dot{\Omega}\tilde{b}_\omega - \Lambda\Omega\tilde{b}_\omega - \Omega\dot{\tilde{b}}_\omega \\ &= -\Lambda(\tilde{\eta}_e + \Omega\tilde{b}_\omega) - (\dot{\Omega}\tilde{b}_\omega + \Omega\dot{\tilde{b}}_\omega).\end{aligned}$$

By defining $\bar{\eta}_e \triangleq \tilde{\eta}_e + \Omega\tilde{b}_\omega$, the above equation can be rewritten as

$$\dot{\bar{\eta}}_e = -\Lambda\bar{\eta}_e. \tag{5.72}$$

Because Λ is stable by design, $\bar{\eta}_e$ exponentially converges to zero.

Next, we proceed to analyze the bias estimation error $\tilde{b}_\omega$. By using (5.67), the dynamics of the bias estimation error are given by

$$\begin{aligned}\dot{\tilde{b}}_\omega = \quad & \Gamma\Omega^T\tilde{\eta}_e = \Gamma\Omega^T(\bar{\eta}_e - \Omega\tilde{b}_\omega) \\ & = -\Gamma\Omega^T\Omega\tilde{b}_\omega + \Gamma\Omega^T\bar{\eta}_e.\end{aligned} \tag{5.73}$$

Note the condition given by (5.68) provides the required persistence of excitation condition for parameter convergence [45]. Using this property in conjunction with Theorem 2.2 from [46], it follows that the homogeneous equation

$$\dot{\tilde{b}}_\omega = -\Gamma\Omega^T\Omega\tilde{b}_\omega \tag{5.74}$$

is exponentially stable, which implies that there exist constants $\gamma > 0$ and $\alpha > 0$, such that the state transition matrix $\Phi(t, \bar{T}_\omega)$ of (5.74) satisfies

$$\|\Phi(t, \bar{T}_\omega)\| \leq \gamma e^{-\alpha(t-\bar{T}_\omega)}. \tag{5.75}$$

Recall that $\bar{\eta}_e$ exponentially converges to zero (see (5.72)). By using (5.73), (5.75), and the definition of $\bar{\eta}_e$, it can shown that $\tilde{b}_\omega$ and $\tilde{\eta}_e$ both converge to zero, and $\hat{\eta}_e$ is bounded, hence completing the proof. □

EXPERIMENTAL RESULTS

In this section, we present some real-time experimental results in order to illustrate the effectiveness of the proposed sensor fault diagnosis method. A block diagram of

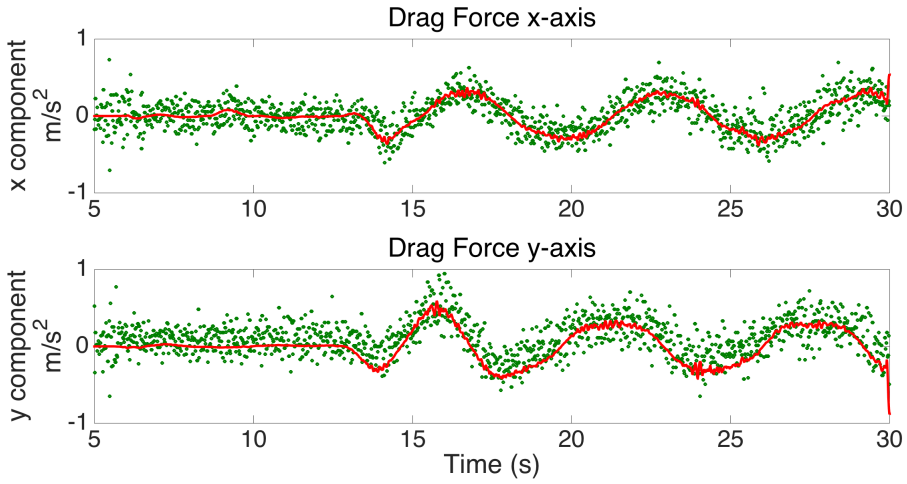

Figure 5.3: Quadrotor drag force modeling. x and y raw accelerometer measurements are depicted with green dots. The drag forces along x and y directions in (5.7) are shown in solid red line.

the indoor quadrotor flight test system is shown in Figure 3.2. During flight tests, quadrotor position and attitude measurements are obtained from the Vicon motion capture camera system. Note that Euler angles obtained from the Vicon system are only used as references during the algorithm evaluation process and are not used for fault diagnosis design. The real-time control and sensor fault diagnosis software executes on-boad on the Gumstix microcontroller, and accelerometer and gyroscope measurements are logged at 200Hz. As previously shown, the fault diagnosis method is independent of the structure of the controller. Therefore, for brevity, the discussion on the controller design is purposely omitted.

The quadrotor model used in the roll and pitch angle estimation method presented in this Chapter is based on the following two critical assumptions: (1) the drag force, denoted by the term $c_{\mathbf{d}} v_B$, appearing in (5.7) is proportional to the body linear velocity, and (2) the Coriolis terms in the body velocity dynamics are negligible. In reality, the drag force acting on the quadrotor body is proportional to the square of the vehicles linear velocity [35]. However, at low speeds and considering the relative small area of the quadrotor, the assumption made on the drag term in (5.7) holds well and has been adopted by many researchers (see for instance [41,52]). Figure 5.3 shows the comparison between the actual accelerometer measurements and the drag term $c_{\mathbf{d}} v_B$ in 5.12, for the x and y axes, respectively.

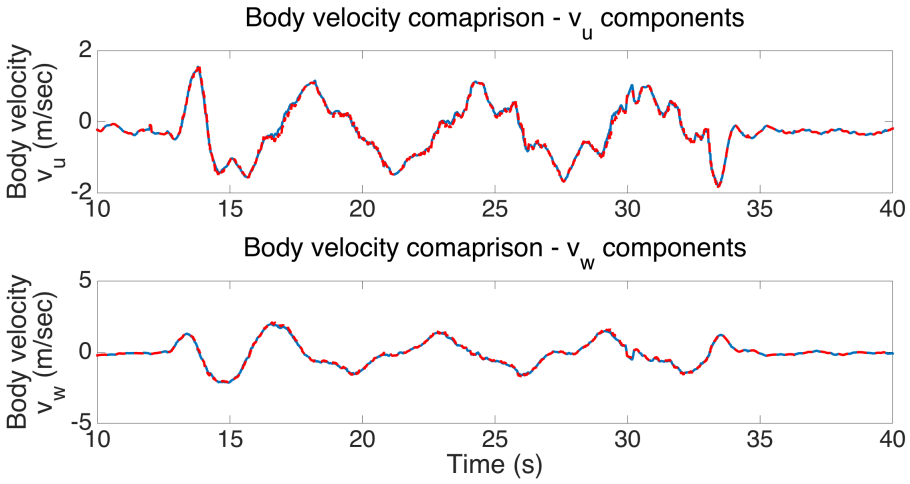

Figure 5.4: Coriolis effects on quadrotor body velocity dynamics: The signals on the right hand side of (5.5) (i.e. Coriolis effects are not included) are depicted in solid blue line and the signals on the right hand side of (5.76) (i.e. Coriolis effects are included) are depicted in solid blue line.

The quadrotor body velocity dynamics including the Coriolis effects are given by:

$$\begin{bmatrix} \dot{v}_u \\ \dot{v}_v \\ \dot{v}_w \end{bmatrix} = \frac{1}{m} \left(\begin{bmatrix} 0 \\ 0 \\ -U \end{bmatrix} - c_{\mathbf{d}} v_B \right) + \begin{bmatrix} -g \sin\theta \\ g \sin\phi \cos\theta \\ g \cos\phi \cos\theta \end{bmatrix} - \omega \times v_B \,. \tag{5.76}$$

The cross product appearing on the right hand side of (5.76) represents the Coriolis effect. Figure 5.4 shows the signals on the right hand side of (5.5) and (5.76) for x and y axes, respectively. As can be seen, the Coriolis effects are small enough, validating the assumption made in (5.5).

In order to evaluate the proposed fault diagnosis method, three different fault cases are considered: 1) accelerometer sensor fault, 2) gyroscope sensor fault, and 3) simultaneous accelerometer and gyroscope faults. The experimental evaluation of each of these sensor fault scenario is performed using the following procedure:

- The quadrotor is commanded to follow a pre-defined trajectory, while maintaining constant altitude and orientation.
- Sensor measurements are artificially corrupted by injecting a constant bias into accelerometer and gyroscope measurements, respectively, while the quadrotor is airborne.
- Quadrotor sensor measurements are processed on-line, and the on-board IMU sen-

sor fault diagnosis algorithm monitors the sensor measurements for fault detection.

- Once a sensor fault is detected, the quadrotor is commanded to hover at its current position, which facilitates the estimation of the sensor biases under consideration.
- Once an estimation of the sensor bias is obtained, the quadrotor resumes its predefined trajectory.

CASE OF ACCELEROMETER SENSOR FAULT

In this scenario, the quadrotor is commanded to follow a circular trajectory with a radius of 1 m. At the time of $t = 30$ s, a constant bias of $b_a = [0.4, -0.45, 1.2]^T m/s^2$ is injected into the accelerometer measurements (see (5.10)). The estimation of roll and pitch angles generated by (5.36) and (5.37) is shown in Figure 5.5. As can be seen, the estimated roll and pitch angles (in red and solid lines) closely track the true attitude angles (in blue and dashed lines) of the quadrotor (provided by the Vicon camera system), even in the presence of measurement bias. It is worth noting that the time delays, introduced by the sliding-mode observer and filtering of accelerometer measurements and observer outputs, have been taken into account in the algorithm implementation.

The FDI results are shown in Figure 5.6 and Figure 5.7. As can be seen form Figure 5.6, shortly after the occurrence of an accelerometer fault, at least one component of the accelerometer sensor diagnostic residual exceeds its corresponding threshold, indicating the detection of an accelerometer fault. Moreover, as can be seen from Figure 5.7, all three components of the gyroscope bias diagnostic residual always remain below their corresponding thresholds. Thus, based on the FDI decision logic described in this Chapter, the occurrence of an accelerometer sensor fault is determined. The accelerometer bias estimation generated by (5.56) is shown in Figure 5.8. As can be seen, after a short period of time, all three components of the estimated accelerometer bias (in solid blue lines) converge reasonably close to the true values (in green and dashed lines).

CASE OF GYROSCOPE SENSOR FAULT

In this scenario, the quadrotor is commanded to follow a set of way points. At the time of $t = 30$ s, a constant bias $b_\omega = [5, 7, 10]^T$ °/s is injected into the gyroscope

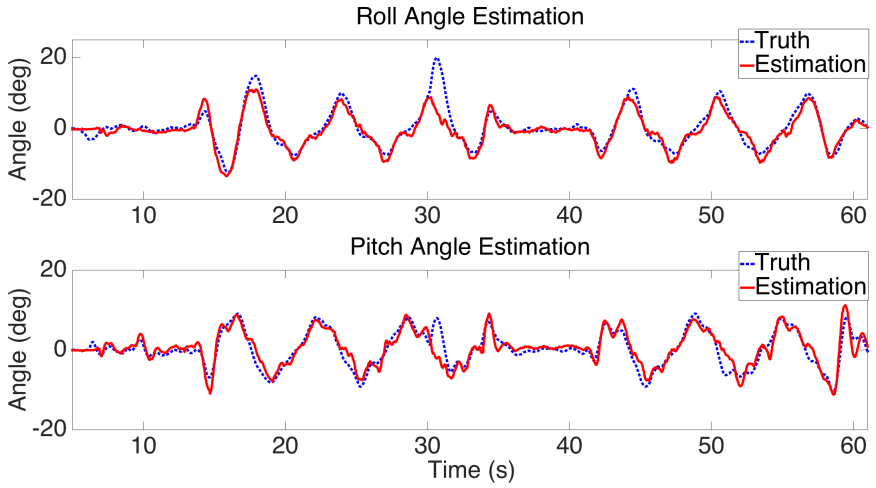

Figure 5.5: Roll and pitch angle estimation with accelerometer bias faults.

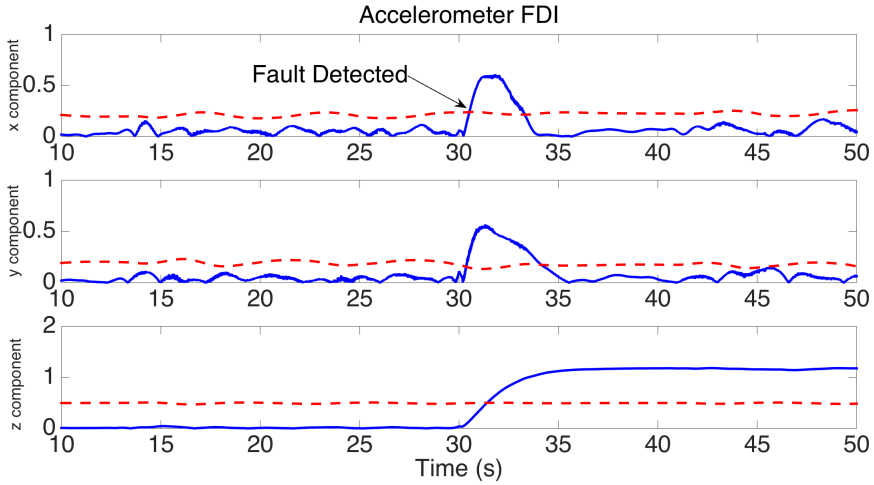

Figure 5.6: Accelerometer bias diagnostic residuals: accelerometer sensor fault.

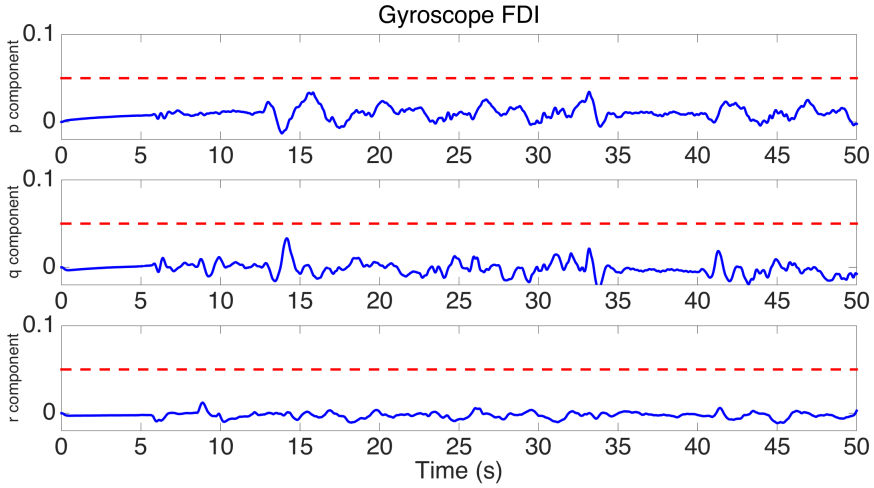

Figure 5.7: Gyroscope bias diagnostic residuals: accelerometer sensor fault.

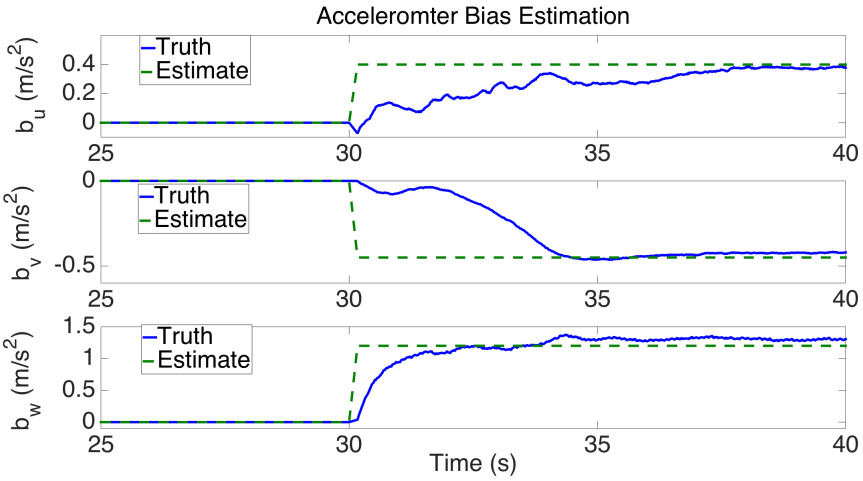

Figure 5.8: Accelerometer bias fault estimation.

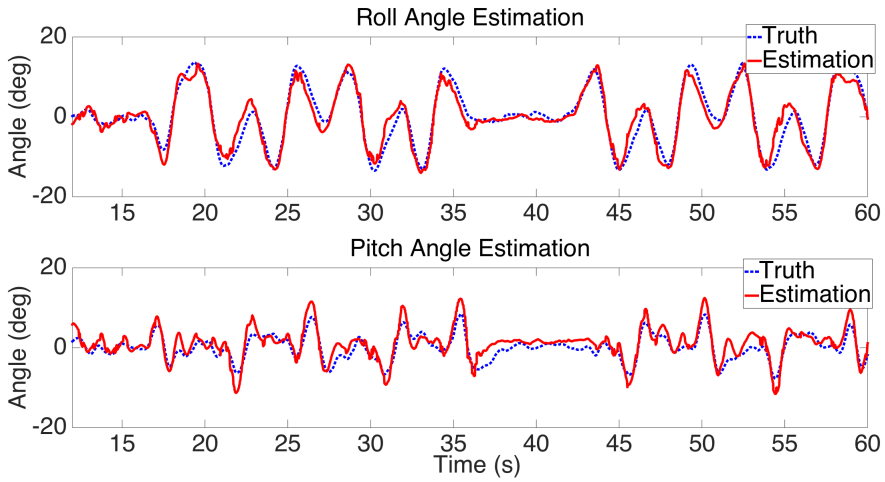

Figure 5.9: Roll and pitch angle estimation with gyroscope bias faults.

measurements (see 5.11)). The estimation of roll and pitch angles generated by the SMO algorithm is shown in Figure 5.9. As can be seen, the estimated roll and pitch angles (in solid red lines) closely track the true roll and pitch angles (in dashed blue lines), even in the presence of gyroscope biases.

The FDI results of gyroscope sensor fault are illustrated in Figure 5.10 and Figure 5.11, respectively. As can be seen, shortly after the occurrence of a gyroscope sensor fault, at least one component of the gyroscope diagnostic residual exceeds its corresponding detection threshold. Meanwhile, all three accelerometer diagnostic residuals always remain below the detection threshold. Therefore, the occurrence of a gyroscope sensor fault is concluded.

Additionally, as shown in Figure 5.12, after a short period of time, all three components of the estimated gyroscope bias converge reasonably close to the true values.

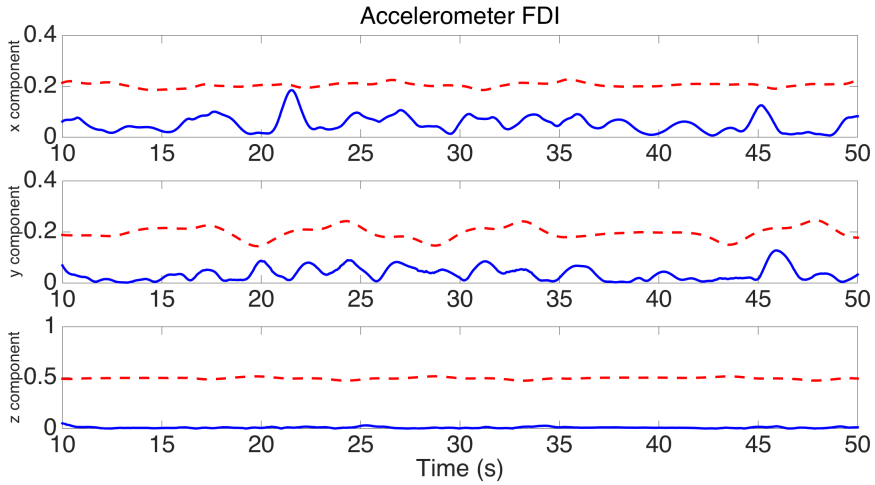

Figure 5.10: Accelerometer bias diagnostic residuals: gyroscope sensor fault.

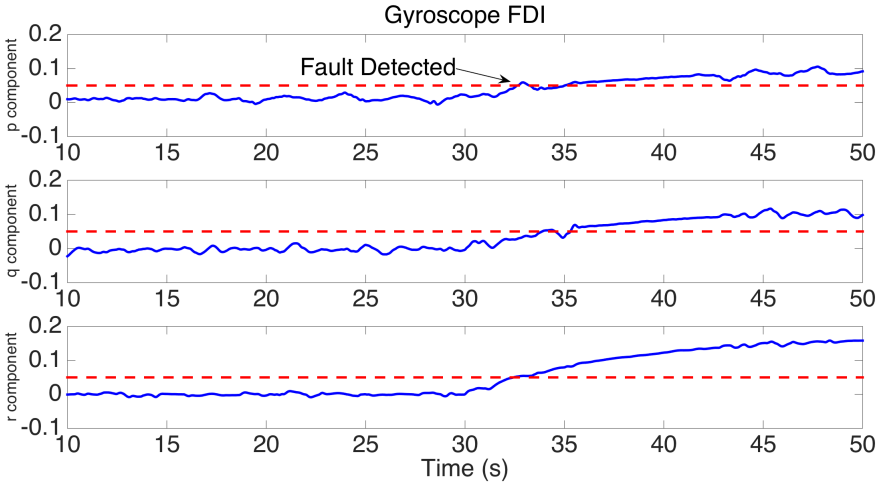

Figure 5.11: Gyroscope bias diagnostic residuals: gyroscope sensor fault.

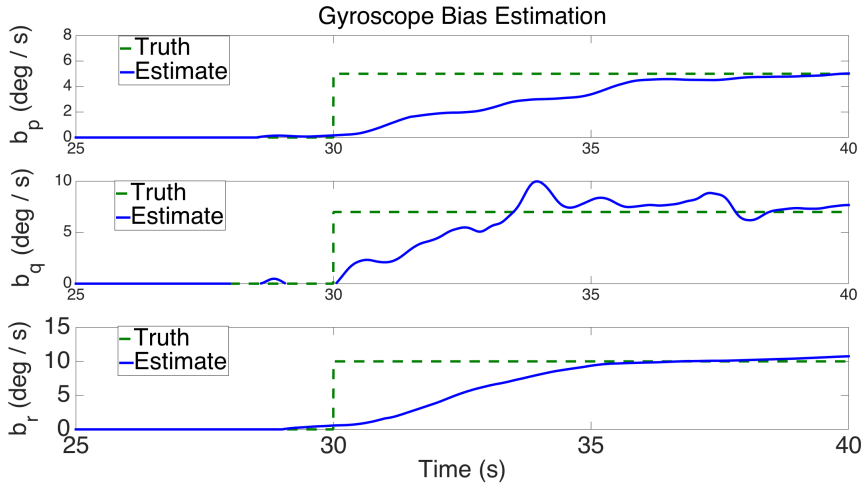

Figure 5.12: Gyroscope bias estimation.

CASE OF SIMULTANEOUS SENSOR FAULTS

In this case study, the quadrotor is commanded to follow a rectangular trajectory. At time $t = 30\,\text{s}$, simultaneous faults are injected into accelerometer and gyroscope measurements. The sensor fault magnitudes are $b_a = [0.55, -0.45, 1.2]^T\,\text{m/s}^2$ and $b_\omega = [5, 7, 9]^T\,^\circ/\text{s}$. The estimation of roll and pitch angles is shown in Figure 5.13. As can be seen, the estimated roll and pitch angles closely track the actual angles, except for a short duration at the time of fault occurrence.

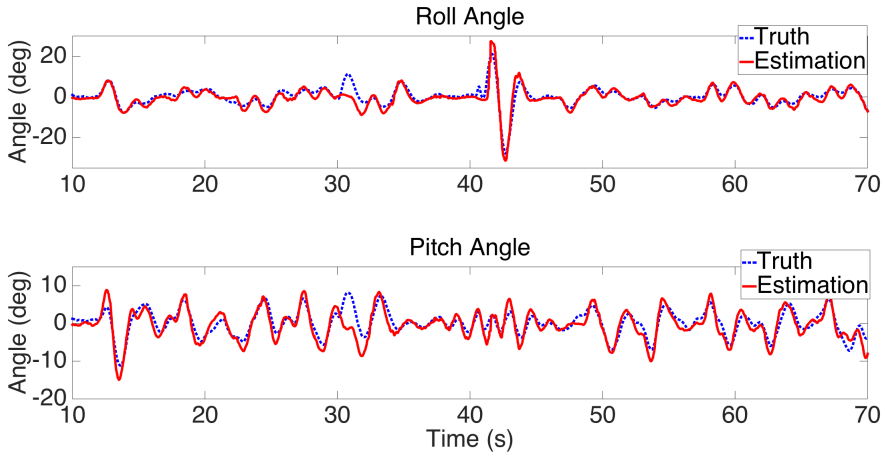

Figure 5.13: Roll and pitch angle estimation with simultaneous sensor faults.

The accelerometer and gyroscope FDI results are shown in Figure 5.14 and Figure 5.15, respectively. As can be seen from Figure 5.14, at least one component of the accelerometer diagnostic residual exceeds its corresponding threshold shortly after the occurrence of the fault. Meanwhile, as shown in Figure 5.15, a gyroscope fault is also detected, since at least one component of the gyroscope diagnostic exceeds its corresponding threshold.

Additionally, as can seen in Figure 5.16 and Figure 5.17, all components of the estimated accelerometer and gyroscope biases closely approach the true values.

EXPERIMENTAL FAULT ACCOMMODATION RESULTS

The IMU sensor fault diagnostic results can potentially be used by the real-time control system to enhance its fault-tolerance capability. Note that the sensor fault diagnosis method is independent of the controller structure. Thus, the diagnostic algorithm can be easily deployed and utilized as an additional software component in the overall

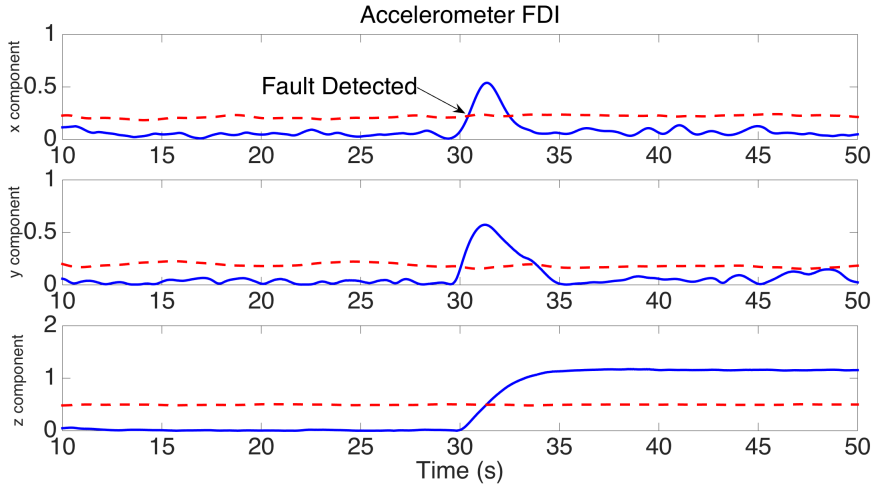

Figure 5.14: Accelerometer bias diagnostic residuals: simultaneous sensor faults.

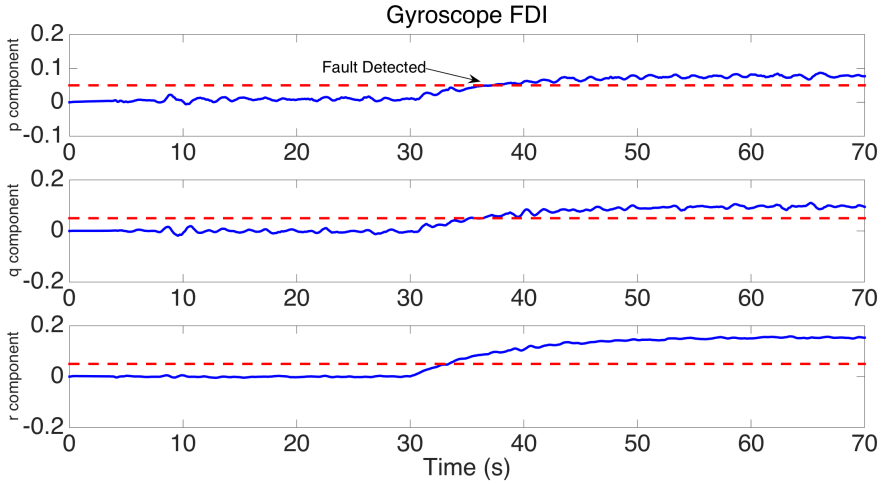

Figure 5.15: Gyroscope bias diagnostic residuals: simultaneous sensor faults.

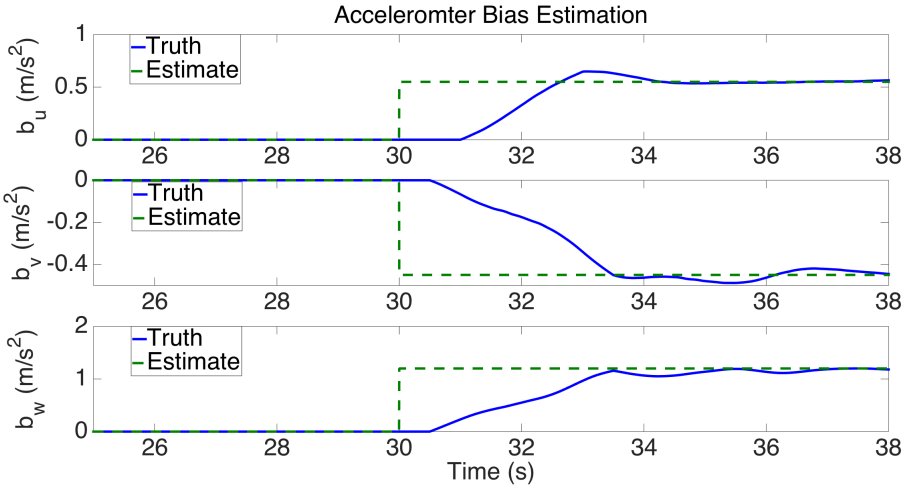

Figure 5.16: Accelerometer fault bias estimation in the case of simultaneous faults.

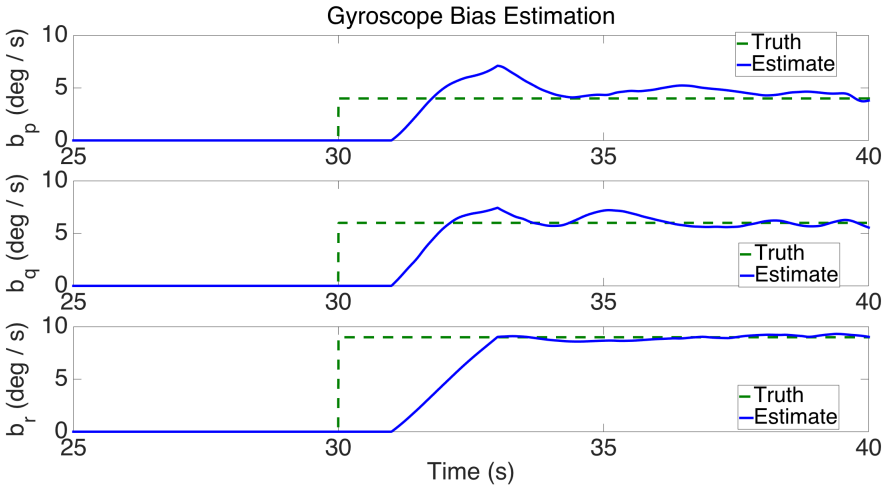

Figure 5.17: Gyroscope fault bias estimation in the case of simultaneous faults.

quadrotor control architecture. To obtain a better insight into the potential applications of the sensor fault diagnosis method, below we consider an application example of integrating the sensor diagnosis method with the real-time control system.

In practical quadrotor control applications, the roll and pitch angles are often not directly measured and need to be estimated from related sensor signals. One of the solutions that have been developed is to use the extended Kalman filter (EKF) to provide an estimate of the roll and pitch angles based on on-board accelerometer and gyroscope measurements (see, for instance, [53]). However, IMU sensor measurement biases can possibly degrade the attitude angle estimation generated by the EKF and the tracking performance of the overall quadrotor control system. The integration of an on-board IMU sensor fault diagnostic algorithm can help enhance the fault-tolerance of the real-time estimation and control system.

Figure 5.18 shows an application example of integrated IMU sensor FDIE with on-board EKF and quadrotor controller. Specifically, the sensor bias estimation provided by the fault diagnosis module is used as an input to the EKF in order to correct possible biases in gyroscope and accelerometer measurements. It is worth noting that, due to the filtering of excessive noise in the accelerometer measurements, the roll and pitch angle estimation generated by the SMO has a time delay and therefore not suitable to be used directly by the real-time controller. Once the sensor bias diagnostic information is obtained, it can be used to compensate for faulty IMU sensor measurements and improve the estimation performance of the EKF algorithm.

In order to illustrate the benefits of the integrated system architecture shown in

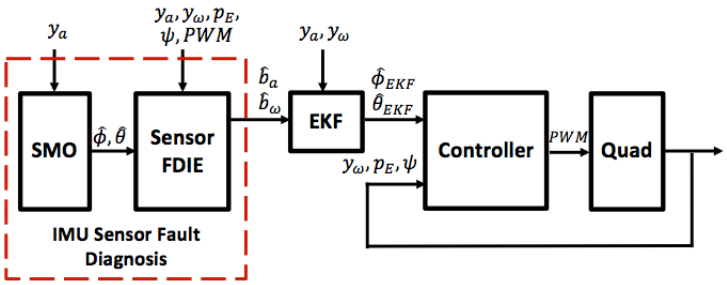

Figure 5.18: Integration of sensor FDIE with on-board EKF and controller.

Figure 5.18, we consider the case of simultaneous faults. Specifically, the following scenario is investigated experimentally: the quadrotor is commanded to follow a rectangular trajectory, while maintaining a constant altitude of 0.5 m and a constant orientation. At time $t = 30$ s, simultaneous faults are injected into accelerometer and gyroscope measurements. Once a fault is detected, the quadrotor is commanded to hover at its current position. When an estimate of the sensor biases is provided by the FDIE module, it is used as an input to the EKF to correct the gyroscope and accelerometer biases, and the quadrotor resumes its original flight trajectory.

Figure 5.19 shows the estimated roll and pitch angles generated by the EKF during the entire flight duration. As can be seen, before the occurrence of the sensor faults, the EKF is able to accurately estimate the actual roll and pitch angles of the quadrotor. Once the fault is injected (i.e. starting from $t = 30$ s), the estimation of roll and pitch angles generated by the EKF clearly degrades. At approximately $t = 40$ s, an estimate of the sensor biases is obtained and provided to the EKF. As can be seen, for $t > 40$ s, the EKF is able to recover its estimation performance, as a result of the corrected IMU sensor measurements.

Figure 5.20 shows the translational position tracking performance in the $x-$ and $y-$ directions during the entire flight duration. As can be seen, before the occurrence of faults, the quadrotor closely tracks the desired trajectory. However, between times $t = 30s$ and $t = 40s$, the position tracking performance clearly degrades as a result of IMU sensor faults. Note that the IMU sensor fault is detected at approximately $t = 31$ s. At that time, the quadrotor is commanded to hover at it's current position at approximately $[x, y] = [0.5, 0.15]$, until an estimation of sensor biases is obtained. However, as can be seen from Figure 5.20, the quadrotor clearly drifts away from the desired position as a result of degraded attitude angle estimation caused by accelerometer

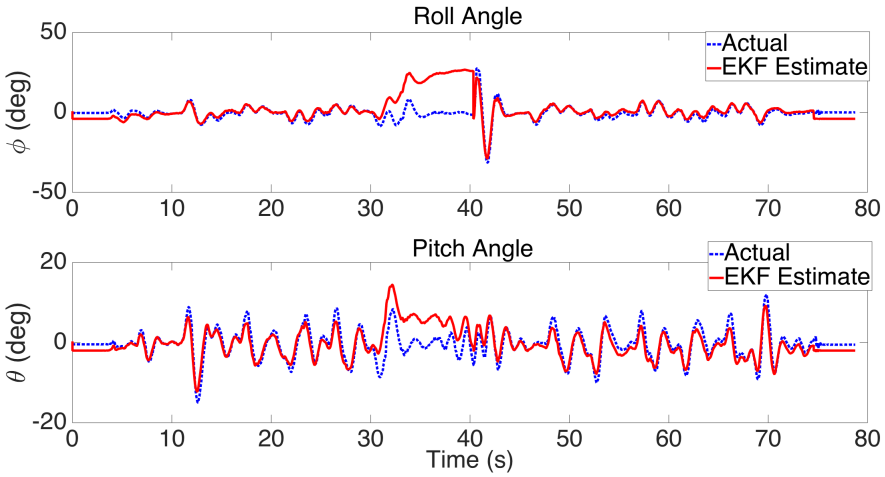

Figure 5.19: Real-time EKF roll/pitch angle estimation.

and gyroscope sensor faults. Moreover, after an estimation of IMU sensor biases is obtained and provided to the EKF (for $t > 40\,\text{s}$), it can be seen that the quadrotor is able to closely track the desired trajectory again, even in the presence of IMU sensor faults.

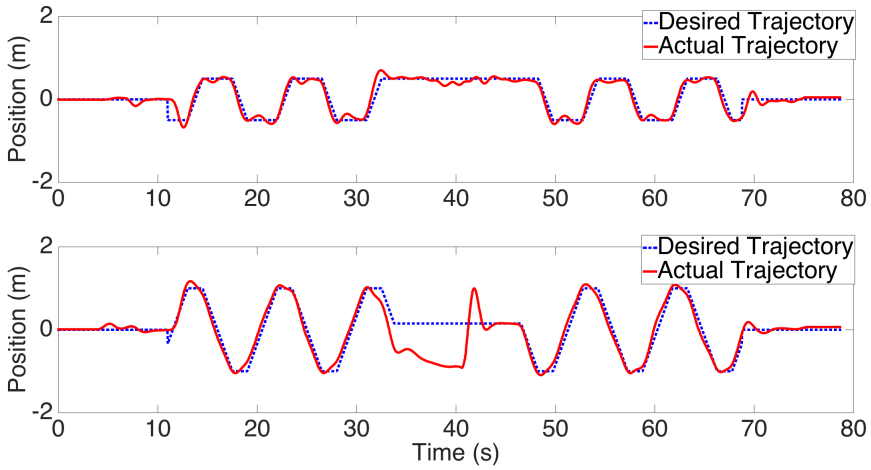

Figure 5.20: Translational position tracking performance (top: $x-$axis, bottom: $y-$axis).

CONCLUSION

In this chapter, we present the design, analysis, and experimental demonstration of a nonlinear fault detection, isolation, and estimation scheme for sensor bias faults in accelerometer and gyroscope measurements of quadrotor UAVs. Using estimated roll and pitch angles provided by a sliding-mode observer, structured residuals are generated

for detecting and isolating the sensor faults. In addition, nonlinear adaptive estimation algorithms are developed to provide an estimate of the unknown magnitude of the sensor bias. The effectiveness of the fault diagnosis method is demonstrated during real-time quadrotor autonomous flight.

VI. QUADROTOR ACTUATOR FAULT DIAGNOSIS AND ACCOMODATION

INTRODUCTION

In this chapter, a fully nonlinear framework for integrated quadrotor actuator fault diagnosis and FTC is formulated. A nonlinear adaptive estimation based FDI method is developed by applying the general methodology in [54]. Adaptive thresholds for fault detection and isolation are systematically designed to achieve enhanced robustness and fault sensitivity properties over fixed thresholds. Following the generalized observer scheme [6], the FDI architecture consists of a bank of adaptive fault isolation estimators (FIEs). Each FIE is designed based on the functional structure of a particular fault under consideration. The fault magnitude estimate provided by the matched adaptive FIE is used to accommodate the fault effect and maintain good position tracking performance even in the presence of faults. The fault diagnosis and accommodation scheme is implemented and demonstrated through real-time flight test with a circular reference trajectory.

PROBLEM FORMULATION

QUADROTOR DYNAMIC MODEL

Unlike IMU sensor faults, which typically evolve slowly over time, actuator faults such as a sudden damage to the propellers, have a significant impact on the overall quadrotor stability and control performance. As a consequence, more accurate models are needed in order to distinguish between the effects of the faults and unmodeled dynamics. The quadrotor dynamics considered in the subsequent chapters are described by:

$$\dot{p}_E = v_E \tag{6.1}$$

$$\dot{v}_E = \frac{1}{m} R_{EB}(\eta) \left(\begin{bmatrix} 0 \\ 0 \\ -U \end{bmatrix} - c_{\mathbf{d}} v_B \right) + \begin{bmatrix} 0 \\ 0 \\ g \end{bmatrix} + \xi_{v0}(x,t) + \xi_v(x,t) \tag{6.2}$$

$$\dot{\eta} = R_\eta(\phi, \theta)\omega \tag{6.3}$$

$$\dot{\omega} = \begin{bmatrix} \frac{J_y - J_z}{J_x} qr \\ \frac{J_z - J_x}{J_y} pr \\ \frac{J_x - J_y}{J_z} pq \end{bmatrix} + \begin{bmatrix} \frac{1}{J_x}\tau_\phi \\ \frac{1}{J_y}\tau_\theta \\ \frac{1}{J_z}\tau_\psi \end{bmatrix} + \xi_{\omega 0}(x,t) + \xi_\omega(x,t)\,, \tag{6.4}$$

Note, the quadrotor model in (6.1) - (6.4) represents a significant departure from the models used in the previous chapters due to the inclusion of additional terms. Specifically, the terms $\xi_{v0}(x,t)$ and $\xi_{\omega 0}(x,t)$ represent additional known nonlinearities (e.g. damping, gyroscopic effects, etc.) in the system dynamics, and $\xi_v(x,t)$ and $\xi_\omega(x,t)$ are the remaining modeling uncertainties in the translational and rotational dynamics, respectively, where $x \triangleq [p_E^T,\, v_E^T,\, \eta^T,\, \omega^T]^T$. The remaining states and parameters in (6.1) - (6.4) have been described in Chapter 3.

ACTUATOR FAULT MODEL

As shown in Figure 3.1, the motors and propellers are configured such that rotors $M1$ and $M3$ rotate counter-clockwise, and rotors $M2$ and $M4$ rotate clockwise. Each rotor is located at a distance d from the quadrotor center of mass and produces a force F_s $(s = 1, .., 4)$ along the negative z direction relative to the body frame. Additionally, due to the spinning of the rotors, a reaction torque τ_s is generated on the quadrotor body by each rotor.

As in [26,55], we consider actuator faults represented by partial loss of effectiveness (LOE) in the rotors. For instance, structural damage to a propeller or an unexpected change in the rotor physical parameters would result in a partial loss of thrust generated by the respective rotor. Specifically, the actuator faults under consideration are modeled as follows: for $s = 1, .., 4$,

$$\Omega_s^* = \alpha_s \Omega_s\,, \tag{6.5}$$

where Ω_s represents the commanded rotor angular velocity, Ω_s^* is the actual rotor angular velocity, and $\alpha_s \in (\bar{\alpha}, 1]$ is an unknown parameter characterizing the occurrence of a partial loss of effectiveness fault in rotor s. The case of $\alpha_s = 1$ represents a healthy rotor, and $\alpha_s < 1$ represents a faulty rotor with partial loss of effectiveness. Note that the constant $\bar{\alpha} > 0$ is a known lower bound needed to maintain the controllability of the quadrotor. For instance, in the extreme case of a complete failure (i.e., $\bar{\alpha} = 0$), the quadrotor orientation becomes uncontrollable.

In this research, the thrust and torque generated by the rotors are considered to be directly proportional to the square velocity of the rotors [10, 34]. Specifically, by considering the actuator fault models (6.5), the relationship between the forces F_s and the reaction torques τ_s generated by each rotor and the rotor angular velocity is given by:

$$F_s = (1 - \beta(t - T_s)\vartheta_s) b_F {\Omega_s}^2 \tag{6.6}$$

$$\tau_s = -(1 - \beta(t - T_s)\vartheta_s) k \, \mathrm{sgn}(\Omega_s) {\Omega_s}^2 \,, \tag{6.7}$$

where $\vartheta_s \triangleq 1 - \alpha_s^2$ represents the unknown fault parameter relative to the s-th rotor's square velocity. Specifically, $\vartheta_s = 0$ represents a healthy rotor, and $\vartheta_s \in (0, \bar{\vartheta})$ represents the case of a rotor experiencing a partial loss of effectiveness, where $\bar{\vartheta} \triangleq 1 - \bar{\alpha}^2$. The constants b_F and k represent rotor thrust and torque constants, respectively, and $\mathrm{sgn}(\cdot)$ represents the signum function. The fault time profile function $\beta(\cdot)$ is assumed to be a step function with unknown fault time occurrence T_s, that is:

$$\beta_s(t - T_s) = \begin{cases} 0 \,, & \text{if } t < T_s \\ 1 \,, & \text{if } t \geq T_s \,, \end{cases} \tag{6.8}$$

for $s = 1, .., 4$.

Thus, based on the quadrotor configuration shown in Figure 3.1 and by using (6.6)-(6.7), the total thrust and moments acting on the quadrotor body can be expressed as:

$$\begin{bmatrix} U \\ \tau_\phi \\ \tau_\theta \\ \tau_\psi \end{bmatrix} = M \left(I_4 - \beta(t - T_s)\vartheta_s \Lambda_s \right) \begin{bmatrix} \Omega_1^2 \\ \Omega_2^2 \\ \Omega_3^2 \\ \Omega_4^2 \end{bmatrix} \,, \tag{6.9}$$

where the vector $[\Omega_1^2, \, \Omega_2^2, \, \Omega_3^2, \, \Omega_4^2]^T$ represents the commanded rotor velocities, I_4 is the 4×4 identity matrix, and M represents the mapping matrix relating thrust and torques to rotor angular velocities [34] and is defined in (3.4). The actuator fault distribution matrix Λ_s characterizes the location of an actuator fault for $s = 1, .., 4$. Specifically, Λ_s is a 4×4 matrix with all entries zero, except for the sth position on the main diagonal. For instance, if a loss of effectiveness fault occurs in rotor $M1$, then $\Lambda_1 = \mathrm{diag}\{1, 0, 0, 0\}$.

In this chapter, we consider the occurrence of a single actuator fault at any time. The research objective focuses on the design and experimental demonstration of a robust fault detection, isolation, and accommodation scheme for quadrotor actuator faults described by (6.1)-(6.4) and (6.9) using adaptive estimation techniques. The following assumption is needed for the design and analysis of the FDI scheme:

Assumption 6.1: The unstructured modeling uncertainties $\xi_v(x,t)$ and $\xi_\omega(x,t)$ in (6.2) and (6.4), respectively, are unknown but assumed to be bounded by some known functions, i.e.,

$$|\xi_v(x,t)| \leq \bar{\xi}_v(x,t) \tag{6.10}$$

$$|\xi_\omega(x,t)| \leq \bar{\xi}_\omega(x,t) \tag{6.11}$$

for all $t \geq 0$.

Assumption 1 characterizes the class of modeling uncertainties under consideration. The bounds on the unstructured modeling uncertainties are needed in order to be able to derive adaptive thresholds to distinguish between the effects of faults and modeling uncertainty in the fault diagnosis procedure.

ACTUATOR FAULT DIAGNOSIS

The proposed actuator fault diagnosis and accommodation architecture is shown in Figure 6.1. As can be seen, it consists of the following main components: (1) a fault detection estimator (FDE) for determining fault occurrence; (2) a bank of four nonlinear adaptive FIEs for identifying the faulty rotor and providing an estimation of the unknown fault parameter. The controller signal and sensor measurements serve as inputs to the fault diagnosis module. Under normal operating conditions, the FDE monitors the system for detecting any faulty behaviors. Once an actuator fault is detected, the four FIEs are activated to isolate the faulty rotor. After fault isolation, the fault parameter estimate provided by the matched FIE is used for fault accommodation. The robustness and fault sensitivity properties of the scheme are enhanced by the use of appropriately designed adaptive thresholds for fault detection and isolation.

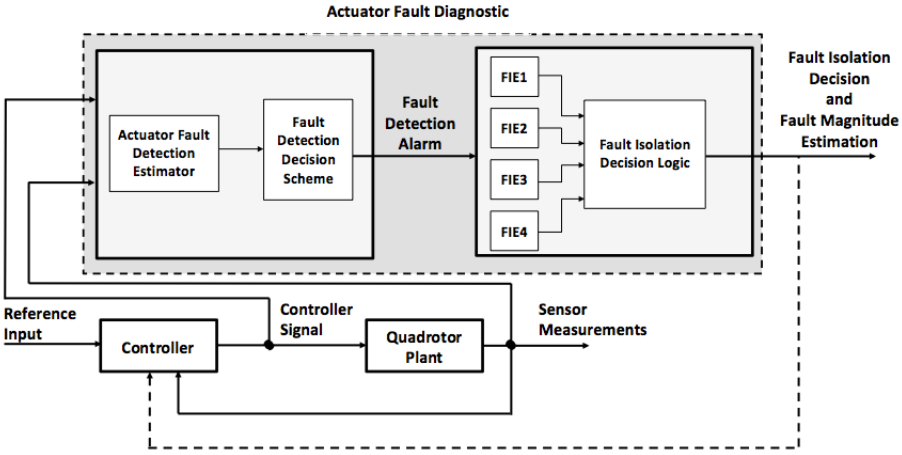

Figure 6.1: Actuator fault diagnosis and accommodation architecture

FAULT DETECTION

By substituting the thrust and torque model (6.9) into the quadrotor velocity and angular rate dynamics model given by (6.2) and (6.4), we obtain:

$$\begin{bmatrix} \dot{v}_z \\ \dot{p} \\ \dot{q} \\ \dot{r} \end{bmatrix} = \varphi(x,t) + GM(I_4 - \beta_s \vartheta_s \Lambda_s) \begin{bmatrix} \Omega_1^2 \\ \Omega_2^2 \\ \Omega_3^2 \\ \Omega_4^2 \end{bmatrix} + \xi(x,t), \tag{6.12}$$

where v_z represents the quadrotor inertial velocity along the $z-$direction (i.e. v_z is the third component of v_E), $G \triangleq \text{diag}\{-\frac{1}{m}\cos\phi\cos\theta,\ J_x^{-1},\ J_y^{-1},\ J_z^{-1}\}$, and the known nonlinearity $\varphi(x,t)$ is defined as:

$$\varphi(x,t) \triangleq \begin{bmatrix} -\frac{c_{\mathbf{d}}}{m} v_z + g \\ \frac{J_y - J_z}{J_x} qr \\ \frac{J_z - J_x}{J_y} pr \\ \frac{J_x - J_y}{J_z} pq \end{bmatrix} + \xi_0(x,t)\,. \tag{6.13}$$

The nonlinear terms $\xi_0(x,t)$ and $\xi(x,t)$ are given by:

$$\xi_0(x,t) \triangleq \begin{bmatrix} \xi_{z0}(x,t) \\ \xi_{\omega 0}(x,t) \end{bmatrix}, \quad \xi(x,t) \triangleq \begin{bmatrix} \xi_z(x,t) \\ \xi_\omega(x,t) \end{bmatrix}, \tag{6.14}$$

with $\xi_{z0}(x,t)$ and $\xi_z(x,t)$ being the third component of $\xi_{v0}(x,t)$ and $\xi_v(x,t)$ in (6.2), respectively. By using (6.12), the following nonlinear fault detection estimator is chosen:

$$\begin{bmatrix} \dot{\hat{v}}_z \\ \dot{\hat{p}} \\ \dot{\hat{q}} \\ \dot{\hat{r}} \end{bmatrix} = -L \begin{bmatrix} \hat{v}_z - v_z \\ \hat{p} - p \\ \hat{q} - q \\ \hat{r} - r \end{bmatrix} + \varphi(x,t) + GM \begin{bmatrix} \Omega_1^2 \\ \Omega_2^2 \\ \Omega_3^2 \\ \Omega_4^2 \end{bmatrix}, \tag{6.15}$$

where $[\hat{v}_z,\, \hat{p},\, \hat{q},\, \hat{r}]^T$ represents estimated inertial velocity and quadrotor angular rates, $L \triangleq \text{diag}\{l_j\}$, for $j = 1, .., 4$, is a positive definite design matrix. Let us define the state estimation error as:

$$\begin{bmatrix} \tilde{v}_z \\ \tilde{p} \\ \tilde{q} \\ \tilde{r} \end{bmatrix} \triangleq \begin{bmatrix} v_z - \hat{v}_z \\ p - \hat{p} \\ q - \hat{q} \\ r - \hat{r} \end{bmatrix}, \tag{6.16}$$

and let $\varepsilon(t) \triangleq [\tilde{v}_z,\, \tilde{p},\, \tilde{q},\, \tilde{r}]^T$. Then, based on (6.12) and (6.15), it follows that the state estimation error dynamics are given by:

$$\dot{\varepsilon}(t) = -L\varepsilon(t) - GM\beta_s\vartheta_s\Lambda_s\bar{\Omega} + \xi(x,t)\,, \tag{6.17}$$

where

$$\bar{\Omega} \triangleq [\Omega_1^2,\, \Omega_2^2,\, \Omega_3^2,\, \Omega_4^2]^T\,. \tag{6.18}$$

Thus, in the absence of actuator faults (i.e., for $t_0 < T_s$), for $j = 1, \cdots, 4$, the j-th component of $\varepsilon(t)$ satisfies

$$|\varepsilon^j(t)| \leq e^{-l_j(t-t_0)}|\varepsilon^j(t_0)| + \int_0^t \left| e^{-l_j(t-\tau)}\xi^j(x,\tau) \right| d\tau\,, \tag{6.19}$$

where $\varepsilon^j(t_0)$ is the initial state estimation error, and $\xi^j(x,t)$ is the j-th components of $\xi(x,t)$ given in (6.14). Based on Assumption 1, the modeling uncertainty $\xi^j(x,t)$ is bounded. Let us denote the bound on $\xi^j(x,t)$ as $\bar{\xi}^j(x,t)$ (i.e. $\bar{\xi}^j(x,t) \geq |\xi^j(x,t)|$). Therefore, based on (6.19), the fault detection thresholds can be chosen as

$$\bar{\varepsilon}^j(t) \triangleq e^{-l_j(t-t_0)}\bar{\varepsilon}^j(t_0) + \int_{t_0}^t e^{-l_j(t-\tau)}\bar{\xi}^j(x,\tau)d\tau\,, \tag{6.20}$$

where $\bar{\varepsilon}^j(t_0) \geq |\varepsilon^j(t_0)|$ is a bound on the initial state estimation error. Thus, it is guaranteed that $|\varepsilon^j(t)| \leq \bar{\varepsilon}^j(t)$ for all $0 \leq t < T_s$. Note that the adaptive detection thresholds described by (6.20) provide improved robustness and fault sensitivity over a fixed threshold [6, 54] and can be easily implemented as the output of the following linear filters:

$$\dot{\bar{\varepsilon}}^j(t) = -l_j \bar{\varepsilon}^j(t) + \bar{\xi}^j(x,t)\,. \tag{6.21}$$

with an initial condition $\bar{\varepsilon}^j(t_0)$.

Fault Detection Decision Scheme: If any component of the diagnostic residual $|\varepsilon^j(t)|$ exceeds its corresponding threshold $\bar{\varepsilon}^j(t)$ at some finite time $t^j > T_s$, then we can conclude that a fault has occurred. The fault detection time is defined as $T_d \triangleq \min\{t^j,\, j = 1, .., 4\}$.

FAULT ISOLATION

In this section, we describe the fault isolation method using adaptive estimation techniques. Suppose an actuator fault has occurred to the s-th actuator at time T_s, and the fault is detected at time $T_d > T_s$, where $s \in \{1, .., 4\}$. Let us define the following state vector: $\zeta \triangleq [v_z, p, q, r]^T$. Therefore, based on (6.12), for $t > T_d$, we have

$$\dot{\zeta} = f(\zeta, \bar{\Omega}) + \xi(x,t) + \vartheta_s h_s(x, \bar{\Omega})\,, \tag{6.22}$$

where $\bar{\Omega}$ is defined in (6.18), $f(\zeta, \bar{\Omega}) \triangleq \varphi(x,t) + GM\bar{\Omega}$, and

$$h_s(x, \bar{\Omega}) \triangleq -GM\Lambda_s\bar{\Omega}\,, \tag{6.23}$$

is the known functional structure of the s-th actuator fault.

As shown in Figure 6.1, once an actuator fault is detected, a bank of four nonlinear adaptive FIEs are activated to determine the partially faulty rotor. Each FIE is designed based on the functional structure of a particular actuator fault under consideration. Specifically, by using (6.22), the following four FIEs are chosen: for $s = 1, \cdots, 4$,

$$\dot{\hat{\zeta}}_s \;\; = -\Gamma_s(\hat{\zeta}_s - \zeta) + f(\zeta, \bar{\Omega}) + \hat{\vartheta}_s h_s(x, \bar{\Omega})\,, \tag{6.24}$$

where $\hat{\zeta}_s$ represents the state estimate, $\Gamma_s = \mathrm{diag}\{\gamma_s^j\}$ is a positive definite design matrix ($j = 1, .., 4$), and $\hat{\vartheta}_s$ is the fault parameter estimate provided by the s-th FIE. The

adaptation in the isolation estimators arises due to the unknown fault parameter ϑ_s. The adaptive law for estimating the unknown parameters $\hat{\vartheta}_s$ is derived using Lyapunov synthesis method [45] and is chosen as

$$\dot{\hat{\vartheta}}_s = \mathcal{P}_\Theta\{\Psi_s h_s^T(x, \bar{\Omega})(\zeta - \hat{\zeta}_s)\}\,, \tag{6.25}$$

where $\Psi_s > 0$ is a design constant representing the learning rate, and the projection operator $\mathcal{P}_\Theta$ is used to constrain the parameter estimate $\hat{\vartheta}_s$ to a known compact region $\Theta \triangleq [0,\, \bar{\vartheta}]$, ensuring the stability of the learning algorithm in the presence of modeling uncertainty [45].

Denote $\tilde{\zeta}_s$ as the state estimation error (i.e., $\tilde{\zeta}_s \triangleq \zeta - \hat{\zeta}_s$) corresponding to the sth isolation estimator. Then, based on (6.22) and (6.24), for $t > T_d$, the dynamics of the j-th component of the state estimation error (i.e., $\tilde{\zeta}_s^j(t)$) is given by:

$$\dot{\tilde{\zeta}}_s^j = -\gamma_s^j \tilde{\zeta}_s^j + \vartheta_s h_s^j(x, \bar{\Omega}) - \hat{\vartheta}_s h_s^j(x, \bar{\Omega}) + \xi^j(x, t)\,. \tag{6.26}$$

The solution of the above differential equation satisfies

$$\begin{aligned} |\tilde{\zeta}_s^j| \leq & \int_{T_d}^{t} e^{-\gamma_s^j(t-\tau)} \left(|\vartheta - \hat{\vartheta}_s| \cdot |h_s^j(x, \bar{\Omega})| + |\xi^j(x, \tau)| \right) d\tau \\ & + e^{-\gamma_s^j(t-\tau)} \bar{\zeta}_s^j\,, \end{aligned} \tag{6.27}$$

where the constant $\bar{\zeta}_s^j \geq |\tilde{\zeta}_s^j(T_d)|$ is an upper bound on the initial state estimation error. Since the parameter estimate $\hat{\vartheta}_s$ belongs to a known compact set Θ, we have $|\vartheta - \hat{\vartheta}_s| \leq \kappa_s(t)$ for a suitable $\kappa_s(t)$ depending on the geometric properties of the set Θ. For instance, by choosing $\Theta \triangleq [0,\, \bar{\vartheta}]$, we have $\kappa_s(t) = \frac{\bar{\vartheta}}{2} + |\hat{\vartheta}_s - \frac{\bar{\vartheta}}{2}|$. Thus, by using (6.27) and Assumption 1, it can be shown $|\tilde{\zeta}_s^j(t)| \leq \mu_s^j(t)$ for $t > T_d$, where

$$\begin{aligned} \mu_s^j(t) \triangleq & \int_{T_d}^{t} e^{-\gamma_s^j(t-\tau)} \left[\kappa_s(\tau) |h_s^j(x, \bar{\Omega})| + \bar{\xi}^j(x, \tau) \right] d\tau \\ & + e^{-\gamma_s^j(t-\tau)} \bar{\zeta}_s^j\,. \end{aligned} \tag{6.28}$$

Note that the adaptive threshold $\mu_s^j(t)$ given by (6.28) can easily be implemented as the

outputs of a linear filter given by:

$$\dot{\mu}_s^j = -\gamma_s^j \mu_s^j + \kappa_s(t)|h_s^j(x,\bar{\Omega})| + \bar{\xi}^j(x,t)\,, \tag{6.29}$$

with an initial condition $\bar{\zeta}_s^j$.

The fault isolation procedure is designed based on the generalized observer scheme [6]. Specifically, the following intuitive principle is employed: if fault $s \in \{1,..,4\}$ occurs at time T_s, and is detected at some finite time $T_d \geq T_s$, then a set of adaptive thresholds $\{\mu_s^j, j = 1,..,4\}$ can be designed for the s-th FIE, such that all components of the state estimation error satisfy $|\tilde{\zeta}_s^j(t)| \leq \mu_s^j(t)$ for all $t > T_d$. Consequently, a set of such adaptive thresholds can be designed for each of the four FIEs. In the fault isolation procedure, for a particular isolation estimator $r \in \{1,..,4\}\backslash\{s\}$, if at least one component of its state estimation error exceeds the corresponding threshold, then the possibility of the occurrence of fault r can be excluded. Thus, we have the following:

Fault Isolation Decision Scheme: If, for each $r \in \{1,...,4\}\backslash\{s\}$, there exists some finite time $t_r > T_d$ and some $j \in \{1,..,4\}$, such that $|\tilde{\zeta}_s^j(t_r)| > \mu_r^j(t_r)$, then the occurrence of a fault in the sth actuator is concluded. The fault isolation time if defined as $T_{isol} \triangleq \max\{t_r,\, r \in \{1,..,4\}\backslash\{s\}\}$.

FAULT ISOLABILITY ANALYSIS

Intuitively (and by following the general approach given in [54]), faults are *isolable* if they are mutually different according to a certain measure quantifying the difference in the effects that different faults have on measurable outputs and on the estimated quantities in the isolation scheme. In this respect, let us define the following fault mismatch function between the sth actuator fault and the r-th actuator fault:

$$\rho_{sr}^j(x,\bar{\Omega}) \triangleq \vartheta_s h_s^j(x,\bar{\Omega}) - \hat{\vartheta}_r h_r^j(x,\bar{\Omega})\,, \tag{6.30}$$

where $s, r = 1,..,4$, $s \neq r$, and $j = 1,..,4$. From a qualitative point of view, the mismatch fault function ρ_{sr}^j can be interpreted as the difference between the actual fault function $\vartheta_s h_s^j(x,\bar{\Omega})$ and its estimate $\hat{\vartheta}_r h_r^j(x,\bar{\Omega})$ generated by the r-th isolation estimator whose structure does not match the actual fault s. The following theorem characterizes the class of isolable faults:

Theorem 6.1. *Consider the fault isolation scheme described by (6.24), (6.25) and (6.28). Suppose that a fault s, with $s \in \{1,..,4\}$, has occurred at time T_s and has been detected at time $T_d > T_s$. Then, fault s is isolable if for each $r = 1,..,4$, $r \neq s$, there exists some finite time $t_r > T_d$ and some $j \in \{1,..,4\}$, such that the fault mismatch function $\rho^j_{sr}(t_r)$ satisfies*

$$\left| \int_{T_d}^{t_r} e^{-\gamma_r^j (t_r - \tau)} \rho^j_{sr}(x, \bar{\Omega}) d\tau \right| \geq 2e^{-\gamma_r^j (t_r - T_d)} \bar{\zeta}_r^j + \int_{T_d}^{t_r} e^{-\gamma_r^j (t_r - \tau)} \left[\kappa_r(\tau) |h_r^j(x, \bar{\Omega})| + 2\bar{\xi}^j(x, \tau) \right] d\tau \,, \tag{6.31}$$

where the constant $\bar{\zeta}_r^j$ is a bound on the initial condition of the j-th component of the state estimation error associated with the r-th isolation estimator.

Proof: Define $\tilde{\zeta}_r$ as the state estimation error associated with the r-th isolation estimator (i.e. $\tilde{\zeta}_r \triangleq \zeta - \hat{\zeta}_r$). Then, in the presence of the sth fault, based on (6.22) and (6.24), the j-th component of the state error dynamics associated with the r-th isolation estimator is given by:

$$\dot{\tilde{\zeta}}_r^j = -\gamma_r^j \tilde{\zeta}_r^j + \xi^j(x,t) + \rho^j_{sr}(x, \bar{\Omega}) \,. \tag{6.32}$$

Thus, for all $t \geq T_d$, we have:

$$\tilde{\zeta}_r^j(t) = e^{-\gamma_r^j (t - T_d)} \tilde{\zeta}_r^j(T_d) + \int_{T_d}^{t} e^{-\gamma_r^j (t - \tau)} \rho^j_{sr}(x, \bar{\Omega}) d\tau + \int_{T_d}^{t} e^{-\gamma_r^j (t - \tau)} \xi^j(x, \tau) d\tau \,.$$

By using the triangle inequality, we obtain

$$|\tilde{\zeta}_r^j(t)| \geq \left| \int_{T_d}^{t} e^{-\gamma_r^j (t - \tau)} \rho^j_{sr}(x, \bar{\Omega}) d\tau \right| - e^{-\gamma_r^j (t - T_d)} |\tilde{\zeta}_r^j(T_d)| - \left| \int_{T_d}^{t} e^{-\gamma_r^j (t - \tau)} \xi^j(x, \tau) d\tau \right| .$$

From (6.28), it can seen that the j-th component of the adaptive threshold, corresponding to the r-th isolation estimator, is given by:

$$\mu_r^j(t) = \int_{T_d}^{t} e^{-\gamma_r^j (t - \tau)} \left[\kappa_r(\tau) |h_r^j(x, \bar{\Omega})| + \bar{\xi}^j(x, \tau) \right] d\tau + e^{-\gamma_r^j (t - T_d)} \bar{\zeta}_r^j \,. \tag{6.33}$$

Then, by using $\bar{\zeta}_r^j \geq |\tilde{\zeta}_r^j(T_d)|$, if inequality (6.31) is satisfied, we have $|\tilde{\zeta}_r^j(t^r)| > \mu_r^j(t^r)$, thus excluding the possibility of the occurrence of the r-th fault. The proof of Theorem 1 follows immediately. □

Remark 6.1: As can be seen from (6.30), the fault mismatch function ρ_{sr}^j is mainly determined by the difference in the functional structures of the s-th actuator fault (represented by h_s^j) and the r-th actuator fault (represented by h_r^j), which are in turn dependent on the actuator fault distribution matrices Λ_s and Λ_r (see (6.23)), respectively. Therefore, from Theorem 6.1, we can see that the fault isolability is largely dependent on the different structure through which each rotor contributes to the total thrust and moments acting on the quadrotor body (see (3.4) and (6.9)) and the level of modeling uncertainty.

ACTUATOR FAULT ACCOMMODATION

After the faulty actuator is isolated, the matched adaptive FIE provides an estimation of the unknown fault magnitude, which can possibly be used to adjust the on-board control signal for the purpose of fault accommodation. In order to obtain a reasonably good estimate of the fault parameter, the condition of persistency of excitation (PE) is required [45]. However, note that the unknown fault parameter ϑ_s in (6.22) is only a scalar. Therefore, it is not difficult to satisfy the required PE level [45].

It is worth noting that the proposed actuator fault diagnosis scheme is independent of the controller structure. The on-board baseline controller is designed based on the nominal quadrotor model given by (6.1) - (6.4) under healthy conditions (i.e. $\vartheta_s = 0$). The controller computes the required rotor velocities, which are sent to the motor servo control system to generate the forces and moments acting on the quadrotor body needed for the quadrotor to track a set of reference trajectories (e.g., attitude, altitude, position). Consequently, controller output signals are available for implementing the fault diagnosis and accommodation algorithms and can be adjusted to compensate for the effects of faults. However, the actual rotor velocities are not measured and not available for the fault diagnosis task.

Specifically, in order to accommodate for the effects of the actuator fault, the

controller commands sent to the rotors are modified as:

$$\bar{\Omega} = (I_4 - \hat{\vartheta}_s \Lambda_s)^{-1} \tilde{\Omega}\,, \tag{6.34}$$

where $\bar{\Omega}$ are the squared rotor velocities generated by the on-board baseline controller (see (6.18)), and $\tilde{\Omega} \triangleq [\tilde{\Omega}_1^2, \tilde{\Omega}_2^2, \tilde{\Omega}_3^2, \tilde{\Omega}_4^2]^T$ are squared rotor velocities adjusted to compensate for the isolated faulty rotor. Recall that the actuator fault parameter relative to the rotor square velocity is given by $\vartheta_s = 1 - \alpha_s^2$. Referring to actuator fault model (6.5), it can be seen that if $\hat{\vartheta}_s \approx \vartheta_s$, then the actual rotor velocity will approximately approach the commanded rotor velocity (i.e. $\Omega_s^* \approx \Omega_s$).

EXPERIMENTAL RESULTS

In this section, we present some real-time flight test results to illustrate the effectiveness of the proposed method. A block diagram of the experimental system setup is shown in Figure 3.2. During flight tests, quadrotor position and attitude information is obtained from the Vicon motion capture camera system.

In order to further take real-world constraints into account, the position and Euler angle measurements provided by the Vicon camera systems are intentionally corrupted by zero mean measurement noise. Using the fast rate position measurements, an estimate of the quadrotor inertial velocity can be obtained by means of linear filtering techniques. Specifically, the velocity v_z used in the FDI scheme is obtained as the output of the following velocity filter:

$$v_z = \frac{\omega_0^2 s}{s^2 + 2\omega_0 s + \omega_0^2} z, \tag{6.35}$$

where z represents the altitude measurement, and ω_0 represents the corner frequency of the velocity filter. For implementation purpose, the above filter is discretized and the corner frequency is chosen to be $\omega_0 = 20\, rad/sec$.

The FDI and FTC algorithm described in this Chapter is based on the quadrotor vertical velocity and angular rate dynamics (see (6.12)). It is worth noting that some of the modeling parameters in (6.12) are directly measurable or can be obtained experimentally (e.g. mass, moments of inertia, etc.). Conversely, motor thrust coefficients (b_F), the drag force coefficient ($c_{\mathbf{D}}$), and the additional known nonlinearities represented

by the term $\xi_0(x,t)$ are not directly measurable and need to be estimated using system identification techniques [56]. Figure 6.2 shows the actual vertical velocity and angular rate dynamics and their estimates. Specifically, referring to (6.12), the signals $\dot{v}_z$, $\dot{p}$, $\dot{q}$, and $\dot{r}$ generated using sensor measurements are depicted in dashed blue line, and their estimates generated based on the model given by the right side of (6.12) are depicted in solid red line. As can be seen, the model-based estimates closely approximate the actual signals.

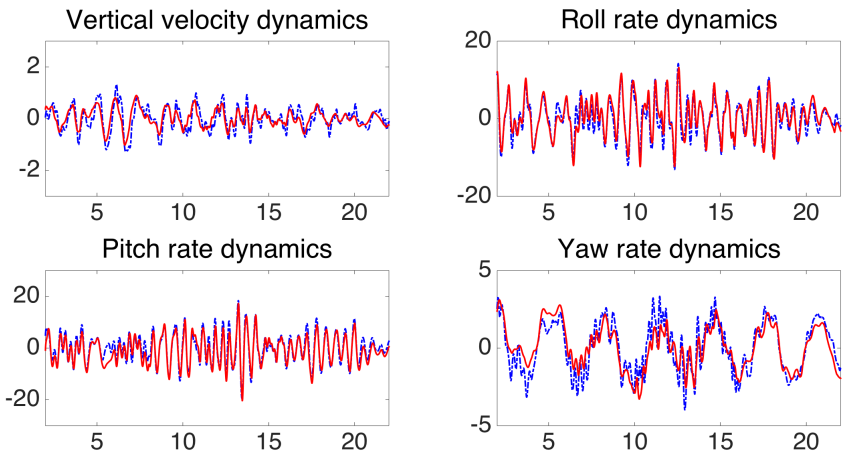

Figure 6.2: Quadrotor model system identification

The uncertainty bound $\bar{\xi}$ on the uncertainty term $\xi(x,t)$ given in (6.14) and Assumption 1 is obtained as follows. By using equation (6.22) under healthy actuator conditions (i.e. $\vartheta_s = 0$), we have

$$\xi(x,t) = \dot{\zeta} - f(\zeta,\bar{\Omega}) \leq \epsilon|\dot{\zeta} - f(\zeta,\bar{\Omega})| = \bar{\xi}(x,t,\bar{\Omega})\,, \tag{6.36}$$

where $\epsilon > 1$ is a constant chosen experimentally ($\epsilon = 1.25$ used in the results shown below). Specifically, the bound $\bar{\xi}$ is generated by using experimental data collected from several autonomous flight scenarios and standard system identification techniques using least squares [56].

EXPERIMENTAL EVALUATION RESULTS

In order to evaluate the proposed actuator fault diagnosis and accommodation method, approximately 1 minute of autonomous flight with real-time FDI and FTC is recorded. A video recording of the experiment has been posted online [57]. The quadro-

tor is commanded to perform a circular maneuver with a radius of 1 meter at a constant altitude while following a sinusoidal orientation angle. Trajectory control of the quadrotor is achieved using a double-loop architecture, as shown in Figure 6.3. Quadrotor position control is achieved by the outer loop. Specifically, the desired quadrotor roll and pitch angles are generated by the following PID control law:

$$\begin{bmatrix} \phi_d \\ \theta_d \end{bmatrix} = R(\psi) \times \left(K_P e(t) + K_I \int_0^t e(\tau)\mathrm{d}\tau + K_D \dot{e}(t) \right)$$

where $e(t) \in \mathbb{R}^{2\times 1}$ represents the position error, K_P, K_I, and K_D are the proportional, integral, and derivative gains, respectively, and

$$R(\psi) \triangleq \begin{bmatrix} \cos\psi & -\sin\psi \\ \sin\psi & \cos\psi \end{bmatrix}$$

is implemented to account for the quadrotor orientation. The *Altitude and Attitude Controller* generates the required rotor velocities needed for the quadrotor to track the desired attitude and altitude trajectories. As described above, the fault diagnosis method is independent of the structure of the controller. Therefore, for brevity, the detailed description of the control algorithm is purposely omitted.

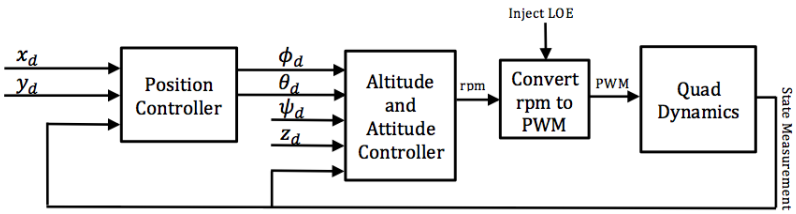

Figure 6.3: Quadrotor control architecture

Quadrotor sensor measurements are processed on-line, and real-time actuator fault diagnostic decision is provided by the diagnostic algorithm. An actuator fault is artificially injected in rotor $M1$ by purposely corrupting the controller output signal $\bar{\Omega}_1$ according to (6.5). Specifically, at approximately time $t = 42.6s$, letting $\alpha_s = 0.87$ results approximately in a 25% loss of effectiveness in the thrust generated by rotor $M1$ (i.e. $\vartheta_1 = 0.25$).

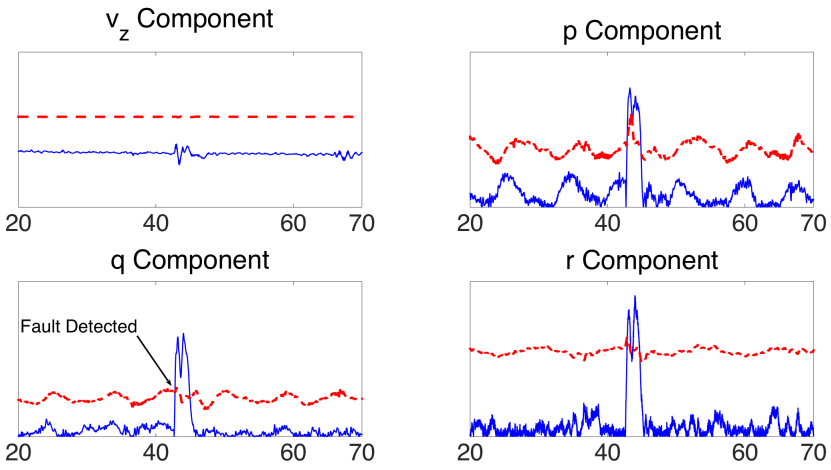

Figure 6.4: Fault detection results: detection residuals (solid blue lines) and adaptive thresholds (dashed red lines).

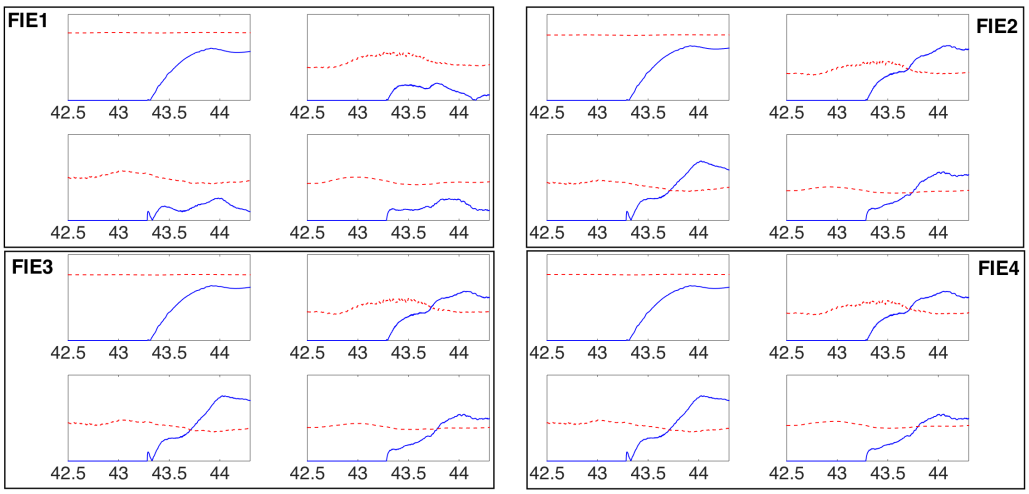

Figure 6.5: Fault isolation results: isolation residual components (solid blue lines) and adaptive thresholds (dashed red lines).

The fault detection residuals and adaptive thresholds, generated by (6.16) and (6.21), are shown in Figure 6.4. As can be seen, before the occurrence of an actuator fault, all components of the detection residuals remain below their corresponding thresholds. Shortly after the occurrence of a loss of effectiveness fault in rotor $M1$ at time $t = 42.6\,\text{sec}$, at least one residual component exceeds its corresponding detection threshold, indicating the occurrence of an actuator fault. Note that all detection residuals go back to remain below their respective thresholds after time $t \approx 45s$. This is the direct result of fault accommodation, which is detailed later in this section.

Figure 6.5 shows the isolation residuals and adaptive thresholds generated by the four FIEs, respectively. As can be seen, all components of the isolation residual generated by $FIE\,1$ always remain below their corresponding thresholds. Additionally, at least one component of the residual generated by any other FIEs exceeds the corresponding threshold shortly at approximately $t = 43.7\,\text{sec}$. Therefore, based on the fault isolation logic derived in this Chapter, we can conclude that a fault has occurred in rotor $M1$.

FAULT ACCOMMODATION

As previously described, the matched FIE provides a reasonable estimate of the fault magnitude. Figure 6.6 shows the estimated fault parameter generated by the adaptive law (6.25). As can be seen, shortly after fault detection (at approximately $t = 43.3\,\text{sec}$), the fault magnitude estimation reasonably approximates the true fault magnitude.

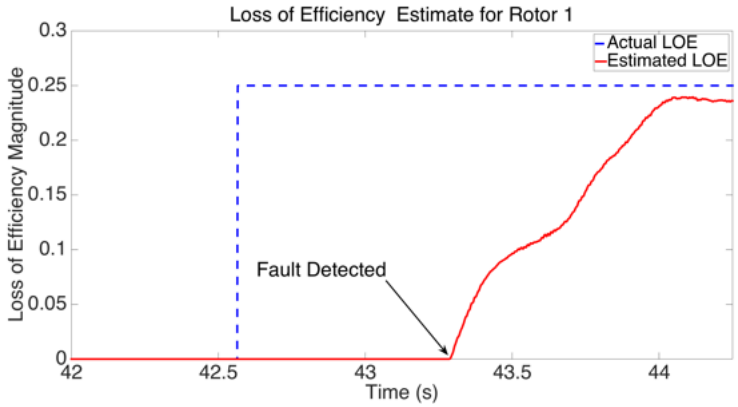

Figure 6.6: Fault parameter estimation

Figures 6.7 and 6.8 show the tracking performance of the quadrotor in the xy inertial plane, before and after the fault accommodation mechanism is employed, respectively. As can be seen from Figure 6.7, before the occurrence of the fault at time $t = 42.6s$, the quadrotor closely tracks the commanded xy position. However, after the occurrence of the fault, the quadrotor drifts away from the desired trajectory. From Figure 6.8, it can seen that shortly after the activation of the fault accommodation mechanism, the quadrotor returns to the desired trajectory and maintains good tracking performance even in the presence of the actuator fault.

Figure 6.9 and Figure 6.10 show the altitude, yaw, roll and pitch angle tracking performance of the quadrotor during the entire flight duration. As can be seen, the

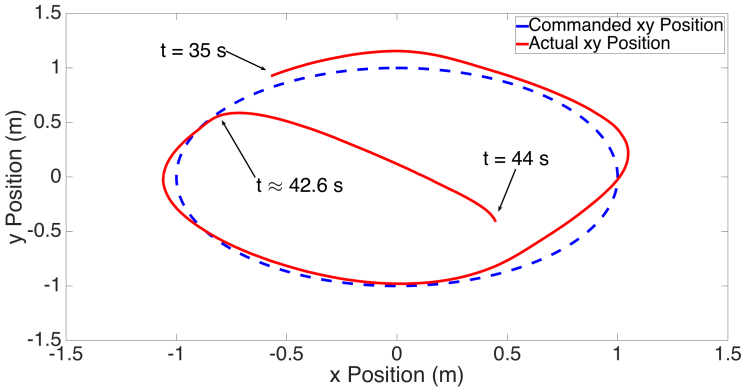

Figure 6.7: Position tracking before fault accommodation

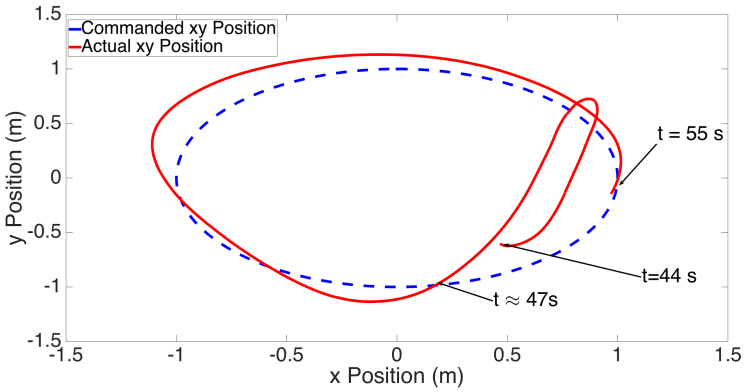

Figure 6.8: Position tracking after fault accommodation

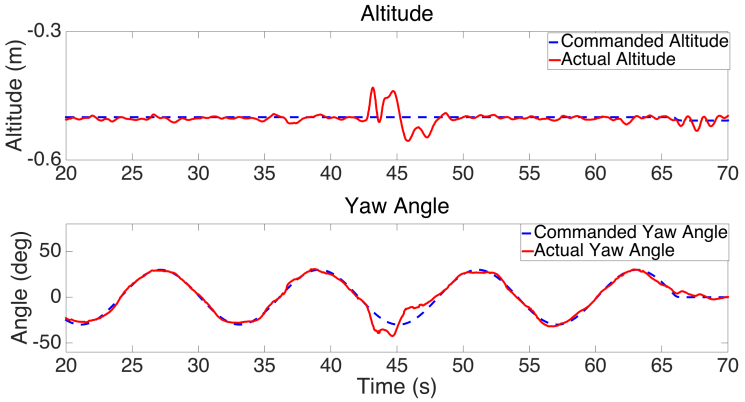

Figure 6.9: Altitude and yaw angle tracking performance

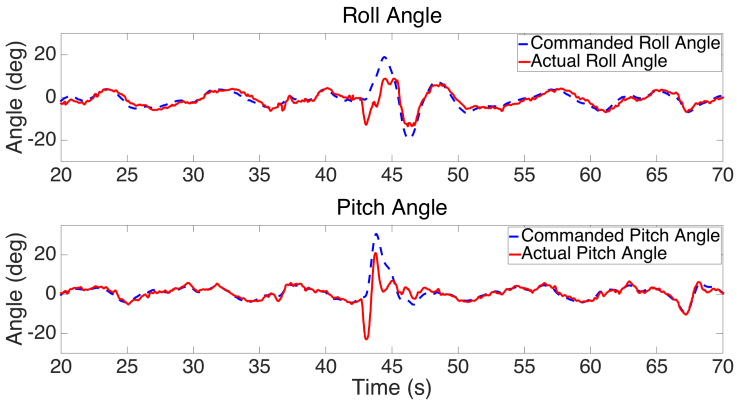

Figure 6.10: Roll and pitch angle tracking performance

traking performance significantly degrades shortly after the occurrence of the actuator fault. However, once the FDI and accommodation procedure is completed, the quadrotor is able to maintain good tracking performance even in the presence of an actuator fault.

CONCLUSIONS

This chapter presents the design and real-time experimental results of a quadrotor actuator fault diagnosis and accommodation method using adaptive estimation techniques. By following the general methodology given in [54], a bank of nonlinear adaptive estimators are designed for detecting and isolating faults in the quadrotor actuating system. Nonlinear adaptive thresholds are designed to enhance the detectability and isolability of FDI method. The diagnostic information is used to adjust the controller output signals to accommodate the fault effect. The fault diagnosis and accommodation method is implemented on a quadrotor UAV test environment and is demonstrated during real-time autonomous flight. An interesting direction for future research is to develop a unified FDI framework for both actuator faults and sensor faults in quadrotor UAVs.

VII. ROBUST FAULT-TOLERANT CONTROL OF QUADROTOR UAVS WITH MULTIPLE ACTUATOR FAULTS

INTRODUCTION

In this chapter, we present the design, analysis and implementation of a nonlinear indirect adaptive altitude and attitude fault-tolerant control algorithm for quadrotor UAVs subject to actuator faults. The adaptation in the control law arises due to the unknown fault magnitudes. A robustifying control effort is added, in order to ensure the stability of the altitude and attitude system in the presence of modeling uncertainties. Additionally, the controller guarantees asymptotic convergence of the altitude and attitude tracking error even in the presence of multiple actuator faults. The control algorithm is implemented on-board of a quadrotor built in-house with off-the-shelf components, and it is evaluated in real-time during autonomous flight. Single and multiple simultaneous faults are artificially injected while the quadrotor is performing an autonomous maneuver and real-time experimental results are shown to illustrate the effectiveness of the control law.

PROBLEM FORMULATION

Based on the quadrotor system dynamics (6.1) - (6.4), the quadrotor altitude and attitude dynamics are given by:

$$\dot{z} = v_z \tag{7.1}$$

$$\dot{\eta} = R_\eta(\phi, \theta)\omega \tag{7.2}$$

$$\dot{v}_z = g - \frac{c_D}{m} v_z - \frac{\cos\phi\cos\theta}{m} U + \xi_{v0}^z(x,t) + \xi_v^z(x,t) \tag{7.3}$$

$$\dot{\omega} = \begin{bmatrix} \frac{J_y - J_z}{J_x} qr \\ \frac{J_z - J_x}{J_y} pr \\ \frac{J_x - J_y}{J_z} pq \end{bmatrix} + J^{-1} \begin{bmatrix} \tau_\phi \\ \tau_\theta \\ \tau_\psi \end{bmatrix} + \xi_{\omega 0}(x,t) + \xi_\omega(x,t)\,, \tag{7.4}$$

where $\xi_{v0}^z(x,t)$ and $\xi_v^z(x,t)$ represent the third component of $\xi_{v0}(x,t)$ and $\xi_v(x,t)$ in (6.2), respectively. Let us define

$$\xi(x,t) \triangleq [\xi_v^z(x,t),\, \xi_\omega(x,t)^T]^T\,. \tag{7.5}$$

The following assumption is needed for the design and analysis of the adaptive FTC algorithm:

Assumption 1: Each component of the unstructured modeling uncertainties $\xi(x,t)$ is unknown but bounded by some known functions, i.e., for $i = 1,..,4$,

$$|\xi_i(x,t)| \leq \bar{\xi}_i(x,t)\,, \quad \forall t \geq 0\,, \tag{7.6}$$

where the boundary function $\bar{\xi}_i(x,t)$ is known.

Assumption 7.1 characterizes the class of modeling uncertainties under consideration. The bound on the unstructured modeling uncertainty $\xi(x,t)$ is needed to guarantee the robustness of the control algorithm to unmodeled dynamics in the altitude and attitude control design process.

As described in Chapter 6, actuator faults are represented by a partial loss of effectiveness (LOE) in the rotors and are modeled as follows for $s = 1,..,4$:

$$\Omega_s^* = \alpha_s \Omega_s\,, \tag{7.7}$$

where Ω_s represents the commanded rotor angular velocity, Ω_s^* is the actual rotor angular velocity. The relationship between the forces F_s and the reaction torques τ_s generated by each rotor and the rotor angular velocity is given by:

$$F_s = (1 - \beta_s(t - T_s)\vartheta_s) b_F \Omega_s^2 \tag{7.8}$$

$$\tau_s = -(1 - \beta_s(t - T_s)\vartheta_s) k\, \mathrm{sgn}(\Omega_s)\Omega_s^2\,, \tag{7.9}$$

where b_F and k represent rotor thrust and torque constants, respectively, and $\mathrm{sgn}(\cdot)$ represents the signum function. The fault time profile function $\beta(\cdot)$ is assumed to be a step function with unknown fault time occurrence T_s. Additionally, the unknown fault parameter relative to the the s-th rotor's square velocity is defined as:

$$\vartheta_s \triangleq 1 - \alpha_s^2 \tag{7.10}$$

Specifically, $\vartheta_s = 0$ represents a healthy rotor, and $\vartheta_s \in (0, \bar{\vartheta})$ represents the case of a rotor experiencing a partial loss of effectiveness, where $\bar{\vartheta} \triangleq 1 - \bar{\alpha}^2$. Thus, based on the quadrotor configuration shown in Figure 3.1 and by using (7.8)-(7.9), the total thrust

and moments acting on the quadrotor body can be expressed as:

$$\begin{bmatrix} U \\ \tau_\phi \\ \tau_\theta \\ \tau_\psi \end{bmatrix} = M \left(I_4 - \sum_{s=1}^{4} (\beta_s \vartheta_s \Lambda_s) \right) \begin{bmatrix} \Omega_1^2 \\ \Omega_2^2 \\ \Omega_3^2 \\ \Omega_4^2 \end{bmatrix}, \tag{7.11}$$

where I_4 is the 4×4 identity matrix, and M represents the mapping matrix relating thrust and torques to rotor angular velocities defined in (3.4). The actuator fault distribution matrix Λ_s characterizes the location of an actuator fault for $s = 1, .., 4$. Specifically, the terms Λ_s are defined as $\Lambda_1 = \text{diag}\{1, 0, 0, 0\}$, $\Lambda_2 = \text{diag}\{0, 1, 0, 0\}$, $\Lambda_3 = \text{diag}\{0, 0, 1, 0\}$, and $\Lambda_4 = \text{diag}\{0, 0, 0, 1\}$. See Chapter 6 for a detailed description of the parameters in (7.7) - (7.10).

In this research we consider the possible occurrence of multiple simultaneous actuator faults at any time. The objective is the design, analysis and experimental demonstration of a robust nonlinear fault-tolerant adaptive control law. The control law is able to stabilize the quadrotor dynamics and guarantees asymptotic altitude and attitude angles tracking performance even in the presence of possible multiple actuator faults.

Remark 7.1. Unlike approaches described in [58–60], the fault-tolerant control scheme presented in this research does not require a fault diagnosis component to detect, isolate and estimate possible actuator faults. The proposed fault-tolerant control scheme is able to automatically adapt and accommodate the occurrence of possible multiple simultaneous actuator faults.

QUADROTOR NONLINEAR ADAPTIVE FAULT-TOLERANT CONTROL METHOD

In this section, we describe the design of a nonlinear adaptive fault-tolerant controller for stabilizing the quadrotor altitude and attitude dynamics and maintain good tracking performance even when one or more rotors are subjected to a partial loss of effectiveness.

Let us define the following state variables:

$$x_1 \triangleq [z\,,\phi\,,\theta\,,\psi]^T$$
$$x_2 \triangleq [v_z\,,p\,,q\,,r]^T$$

Then, by using the thrust and torque models with actuator faults described by (7.11) and after some algebraic manipulation, the altitude and attitude dynamics given by (7.1) - (7.4) can be written in the following compact form:

$$\dot{x}_1 = g_1(x_1)x_2 \tag{7.12}$$
$$\dot{x}_2 = f_2(x_1,x_2)+g_2(x_1)M\left[\left(I_4-\sum_{s=1}^{4}\vartheta_s\Lambda_s\right)\bar{\Omega}+\xi^*(x,t)\right], \tag{7.13}$$

where

$$\bar{\Omega} \triangleq [\Omega_1^2,\,\Omega_2^2,\,\Omega_3^2,\,\Omega_4^2]^T\,,$$
$$\xi^*(x,t) \triangleq (g_2(x_1)M)^{-1}\xi(x,t)\,,$$
$$\xi_0(x,t) \triangleq [\xi_{v0}^z(x,t)^T,\;\xi_{\omega 0}^T]^T\,,$$
$$f_2(x_1,x_2) \triangleq \begin{bmatrix} g-\frac{c_D}{m}v_z \\ \frac{J_y-J_z}{J_x}qr \\ \frac{J_z-J_x}{J_y}pr \\ \frac{J_x-J_y}{J_z}pq \end{bmatrix} + \xi_0(x,t)\,,$$
$$g_1(x_1) \triangleq \left[\begin{array}{c|c} 1 & 0 \\ \hline 0 & R_\eta(\phi,\theta) \end{array}\right],$$
$$g_2(x_1) \triangleq \left[\begin{array}{c|c} -\frac{\cos\phi\cos\theta}{m} & 0 \\ \hline 0 & J^{-1} \end{array}\right].$$

From (7.12)-(7.13), it can be seen that the quadrotor altitude and attitude dynamics is susceptible to the occurrence of possible multiple actuator faults with unknown fault magnitudes and modeling uncertainties. Therefore, in the presence of multiple actuator faults and modeling uncertainties, an altitude and attitude controller with fixed gains may suffer from performance degradation or even loss of stability, leading to a fail-

ure of the overall control system. This motivates the design of a robust adaptive control law which is able to stabilize the quadrotor altitude and attitude system in the presence of possible multiple simultaneous actuator faults and modeling uncertainties. The adaptation in the control algorithm arises due to the unknown actuator fault magnitude vector ϑ. The design of the control law is is based on nonlinear adaptive backstepping techniques [61] and is described below.

Consider the following coordinate transformation:

$$z_1 = c_1(x_1 - x_{1d}) + c_2 \int_0^t (x_1 - x_{1d})d\tau \tag{7.14}$$

$$z_2 = x_2 - \alpha \tag{7.15}$$

where $x_{1d}(t) \triangleq [z_d,\, \phi_d,\, \theta_d,\, \psi_d]^T$ represents the desired altitude, roll, pitch and yaw angles, respectively, $c_1 \triangleq \text{diag}\{c_1^1,\, c_1^2,\, c_1^3,\, c_1^4\},\ c_2 \triangleq \text{diag}\{c_2^1,\, c_2^2,\, c_2^3,\, c_2^4\}$ are some design constants with $c_1^i > 0$, and $c_2^i > 0$, for $i = 1, .., 4$. The integral component is added in order to ensure tracking performance in the presence of disturbances, and the virtual control signal α is given by:

$$\alpha \triangleq (c_1 g_1(x_1))^{-1}\big(- k_1 z_1 - c_2(x_1 - x_{1d}) + c_1 \dot{x}_{1d}\big) \tag{7.16}$$

where $k_1 \triangleq \text{diag}\{k_1^1,\, k_1^2,\, k_1^3,\, k_1^4\}$ with $k_1^i > 0$, for $i = 1, .., 4$. Then, the following nonlinear robust adaptive control law is designed:

$$\bar{\Omega} = \bar{\Omega}_0 + \bar{\Omega}^* \tag{7.17}$$

$$\dot{\hat{\vartheta}}_s = \mathcal{P}_{\Theta_s}\{-\sigma_s z_2^T g_2(x_1) M \Lambda_s \bar{\Omega}\}\,, \tag{7.18}$$

where

$$\bar{\Omega}_0 \triangleq \left[g_2(x_1) M \left(I_4 - \sum_{s=1}^{4} (\hat{\vartheta}_s \Lambda_s) \right) \right]^{-1} \times \left(- f_2(x_1, x_2) + \dot{\alpha} - (c_1 g_1(x_1))^T z_1 - c_3 z_2 \right), \tag{7.19}$$

$$\bar{\Omega}^* \triangleq - \left[I_4 - \sum_{s=1}^{4} (\hat{\vartheta}_s \Lambda_s) \right]^{-1} \times \text{diag}\{\text{sgn}(H)\} \bar{\xi}^*(x, t)\,, \tag{7.20}$$

$$H \triangleq z_2^T g_2(x_1) M\,, \tag{7.21}$$

$$\bar{\xi}^*(x,t) \triangleq (g_2(x_1)M)^{-1}\bar{\xi}(x,t)\,, \tag{7.22}$$

$\sigma_s > 0$ is a constant representing the adaptive learning rate, $c_3 \triangleq \text{diag}\{c_3^1, c_3^2, c_3^3, c_3^4\}$ with $c_3^i > 0$, for $i = 1,..,4$, are some design constants, $\text{sgn}(\cdot)$ represents the signum function, and $\bar{\xi}(x,t)$ in (7.22) is defined as $\bar{\xi} \triangleq [\bar{\xi}_1\,, \bar{\xi}_2\,, \bar{\xi}_3\,, \bar{\xi}_4]^T$, representing the bound on the modeling uncertainty defined in (7.6).

In order to guarantee the stability of the adaptive algorithm in the presence of modeling uncertainties, the projection operator $\mathcal{P}$ in (7.18) restricts the parameter estimate to a predefined known compact set $\Theta_s \triangleq [0,\ \bar{\vartheta}_s]$ [45]. Specifically, the projection algorithm takes the following form

$$\mathcal{P}_{\Theta_s}\{-\sigma_s z_2^T g_2(x_1) M \Lambda_s \bar{\Omega}\} = -\sigma_s (z_2^T g_2(x_1) M \Lambda_s \bar{\Omega} - \zeta_s) \tag{7.23}$$

where

$$\zeta_s = \begin{cases} 0 & \text{if } |\hat{\vartheta}_s| = \bar{\vartheta}_s \text{ and } \hat{\vartheta}_s \sigma z_2^T g_2(x_1) M \Lambda_s \bar{\Omega} \leq 0 \\ & \text{or if } |\hat{\vartheta}_s| < \bar{\vartheta}_s \\ H\Lambda_s\bar{\Omega} & \text{otherwise}\,. \end{cases}$$

Remark 7.2 The control law given in (7.17), consists of two parts. The term $\bar{\Omega}_0$ defined by (7.19), is designed to achieve good tracking performance even in the presence of possible multiple actuator faults. The term $\bar{\Omega}^*$ given in (7.20), represents an additional control effort, designed to guarantee the controller robustness to modeling uncertainties. The following result characterizes the closed-loop system dynamics and asymptotic tracking performance:

Theorem 7.1. *Consider the quadrotor altitude and attitude system given by (7.12)-(7.13) subject to possible simultaneous actuator faults described by (7.7) and (7.11). Then, the adaptive fault-tolerant control law (7.17) with the fault parameter adaptive law (7.18) guarantee: (I) that all the signals are bounded; (II) the altitude and attitude tracking error converges asymptotically to zero, i.e.* $\lim_{t\to\infty}(x_1 - x_{1d}) = 0$.

Proof. Differentiating both sides of (7.14) and (7.15) with respect to time and by

using (7.12)-(7.13), the dynamics of the states z_1 and z_2 are given by:

$$\begin{aligned}\dot{z}_1 &= c_1\dot{x}_1 - c_1\dot{x}_{1d} + c_2(x_1 - x_{1d}) \\ &= c_1 g_1(x_1)z_2 + c_1 g_1(x_1)\alpha - c_1\dot{x}_{1d} + c_2(x_1 - x_{1d}) \\ &= c_1 g_1(x_1)z_2 - k_1 z_1 \end{aligned} \tag{7.24}$$

$$\begin{aligned}\dot{z}_2 &= \dot{x}_2 - \dot{\alpha} \\ &= f_2(x_1, x_2) - \dot{\alpha} \\ &\quad + g_2(x_1)M\Big[\Big(I_4 - \sum_{s=1}^{4}\vartheta_s\Lambda_s\Big)\bar{\Omega} + \xi^*(x,t)\Big]. \end{aligned} \tag{7.25}$$

Let us define the rotor fault magnitude parameter estimation error as $\tilde{\vartheta}_s \triangleq \hat{\vartheta}_s - \vartheta_s$. By adding and subtracting the term $g_2(x_1)M(\sum_{s=1}^{4}\hat{\vartheta}_s\Lambda_s)\bar{\Omega}$ to (7.25), it can be shown that

$$\begin{aligned}\dot{z}_2 = f_2(x_1, x_2) - \dot{\alpha} \\ + g_2(x_1)M\left[\left(I_4 - \sum_{s=1}^{4}\hat{\vartheta}_s\Lambda_s\right)\bar{\Omega} + \xi^*(x,t)\right] \\ + g_2(x_1)M\left(\sum_{s=1}^{4}\tilde{\vartheta}_s\Lambda_s\right)\bar{\Omega} \end{aligned} \tag{7.26}$$

Let us consider the following Lyapunov function candidate:

$$V = \frac{1}{2}z_1^T z_1 + \frac{1}{2}z_2^T z_2 + \sum_{s=1}^{4}\frac{1}{2\sigma_s}\tilde{\vartheta}_s^2\,. \tag{7.27}$$

Then, by using $\dot{\hat{\vartheta}} = \dot{\tilde{\vartheta}}$ and (7.17), the time derivative of V along the solutions of (7.24), (7.26), and (7.18) is given by:

$$\begin{aligned}\dot{V} &= z_1^T\dot{z}_1 + z_2^T\dot{z}_2 + \sum_{s=1}^{4}\sigma_s^{-1}\tilde{\vartheta}_s\dot{\tilde{\vartheta}}_s \\ &= z_1^T(c_1 g_1(x_1)z_2 - k_1 z_1) - \sum_{s=1}^{4}\tilde{\vartheta}_s(z_2^T g_2(x_1)M\Lambda_s\bar{\Omega} - \zeta_s) \\ &\quad + z_2^T f_2(x_1, x_2) - z_2^T\dot{\alpha} + z_2^T g_2(x_1)M(I_4 - \sum_{s=1}^{4}\hat{\vartheta}_s\Lambda_s)\bar{\Omega}_0 \\ &\quad + z_2^T g_2(x_1)M\Big[(I_4 - \sum_{s=1}^{4}\hat{\vartheta}_s\Lambda_s)\bar{\Omega}^* + \xi^*(x,t)\Big] + z_2^T g_2(x_1)M(\sum_{s=1}^{4}\tilde{\vartheta}_s\Lambda_s)\bar{\Omega}\,. \end{aligned} \tag{7.28}$$

Let us substitute the control laws (7.19) and (7.20) into (7.28). Then, by using the following identity:

$$z_2^T(c_1 g_1(x_1))^T z_1 = z_1^T\big((c_1 g_1(x_1) z_2)^T\big)^T = z_1^T c_1 g_1(x_1) z_2\,,$$

it immediately follows that:

$$\begin{aligned}\dot{V} = &-z_1^T k_1 z_1 - z_2^T c_3 z_2 - \sum_{s=1}^{4} \tilde{\vartheta}_s (z_2^T g_2(x_1) M \Lambda_s \bar{\Omega} - \zeta_s) \\ &+ z_2^T g_2(x_1) M \Big[- \operatorname{diag}\{\operatorname{sgn}(H)\} \bar{\xi}^*(x,t) + \xi^*(x,t) \Big] \\ &+ z_2^T g_2(x_1) M (\sum_{s=1}^{4} \tilde{\vartheta}_s \Lambda_s) \bar{\Omega}\,.\end{aligned}$$

Note that that the projection operator can only make the Lyapunov function more negative [45]. Thus, we have

$$\begin{aligned}\dot{V} \leq &-z_1^T k_1 z_1 - z_2^T c_3 z_2 \\ &+ \sum_{i=1}^{4} (-H_i \operatorname{sgn}(H_i) \bar{\xi}_i^*(x,t)) + \sum_{i=1}^{4} H_i \xi_i^*(x,t),\end{aligned}$$

where $H_i\,, \bar{\xi}_i^*$, and ξ_i^* represent the i-th components of H, $\bar{\xi}^*$, and ξ^*, respectively, for $i = 1, .., 4$. By noting that $H_i = |H_i| \operatorname{sgn}(H_i)$, it immediately follows that

$$\begin{aligned}\dot{V} &\leq -z_1^T k_1 z_1 - z_2^T c_3 z_2 + \sum_{i=1}^{4} \big(-|H_i| \bar{\xi}_i^*(x,t) + H_i \xi_i^*(x,t)\big) \\ &\leq -z_1^T k_1 z_1 - z_2^T c_3 z_2\,. \end{aligned} \tag{7.29}$$

Based on (7.27) and the above inequality, we have $z_1 \in \mathcal{L}_\infty$, $z_2 \in \mathcal{L}_\infty$, and $\tilde{\vartheta}_s \in \mathcal{L}_\infty$. Moreover, since ϑ_s is bounded by definition, it follows that $\hat{\vartheta}_s \in \mathcal{L}_\infty$. Thus, $\bar{\Omega} \in \mathcal{L}_\infty$, which implies that $\dot{z}_1 \in \mathcal{L}_\infty$ and $\dot{z}_2 \in \mathcal{L}_\infty$. By noting that $V(t)$ is positive semi-definite and that $\dot{V} \leq 0$, it follows that $\lim_{t\to\infty} V(t) = V_\infty$ exists and is finite. By integrating (7.29) for $t \in [t_0, \infty]$ we have:

$$\int_{t_0}^{t} (z_1^T k_1 z_1 + z_2^T c_3 z_2) dt \leq V(t_0) - V_\infty.$$

Therefore, z_1, and z_2 are square integrable, i.e. z_1, $z_2 \in \mathcal{L}_2$. Thus, by using Barbălt's

Lemma [45], we can conclude that:

$$\lim_{t\to\infty} z_1 = [0,0,0,0]^T,$$

$$\lim_{t\to\infty} z_2 = [0,0,0,0]^T.$$

Let us define the altitude and attitude tracking error $e_F \triangleq x_1 - x_{1d}$. Then, by using the above results in conjunction with (7.14)-(7.15), it follows that as $t \to \infty$, the tracking error dynamics satisfies:

$$\dot{e}_F = -\frac{c_2}{c_1} e_F \,. \tag{7.30}$$

Thus, $e_F \to 0$, hence, concluding the proof. □

Remark 7.3 The adaptive law (7.18) simultaneously provides an estimate of the four unknown fault parmeters ϑ_s, for $s = 1,..,4$. However, the convergence of parameter estimates to the actual values is guaranteed only if the special condition of persistency of excitation is satisfied [45], which is not necessarily always guaranteed during flight. As shown, in the proof of Theorem 7.1, the control law (7.17)-(7.18) does not require the PE condition. Moreover, asymptotic altitude and attitude tracking performance is guaranteed even if the parameter estimates do not converge to the actual values.

Remark 7.4 Note that the control law (7.17) is discontinuous, since each element of $\bar{\Omega}_i^*$ is discontinuous at $H_i = 0$ for $i = 1,..,4$ (see (7.20)). This discontinuity can cause undesirable chattering which can be remedied by using a smooth approximation of the sign function (for instance, the hyperbolic tangent function [62]). In this case, using a similar Lyapunov synthesis method, it can be shown that the tracking error e_F converges to an arbitrarily small region around zero.

EXPERIMENTAL RESULTS

In this section, we present some real-time experimental results in order to illustrate the effectiveness of the proposed fault-tolerant altitude an attitude control algorithm. The altitude and attitude fault-tolerant control algorithm presented in this chapter is implemented on-board, and is evaluated in real-time during autonomous flight.

Two cases are presented: (1) single actuator fault, and (2) multiple simultaneous

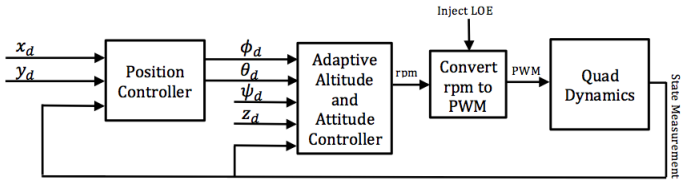

Figure 7.1: Quadrotor control architecture

actuator faults. A video recording of the experiments has been posted online [63]. In order to evaluate the proposed altitude and attitude fault-tolerant control method, real-time data of the autonomous quadrotor flight with FTC is recorded. The quadrotor is commanded to follow a circular trajectory at a constant altitude while following a sinusoidal orientation angle.

The *Adaptive Altitude and Attitude Controller* generates the required rotor velocities needed for the quadrotor to track the desired altitude and attitude trajectories even in the presence of multiple simultaneous actuator faults. Quadrotor sensor measurements are processed on-line, and real-time actuator fault tolerance is provided by the adaptive altitude and attitude control algorithm. As previously described, the control algorithm is based on the quadrotor vertical velocity and angular rate dynamics (see (7.1)-(7.4)) and requires measurements of the states x_1 and x_2. Altitude and Euler angle measurements are directly obtained from the Vicon camera system. An estimate of the quadrotor inertial velocity is obtained from position measurements by means of linear filtering and angular rate measurements are obtained from an on-board gyroscope.

Actuator faults are artificially injected in the rotors by purposely corrupting the controller output signal $\bar{\Omega}$ according to (7.7). Note, that the controller output $\bar{\Omega}$ represents the square velocities of each rotor. A conversion block, accounting for battery drainage is used to convert the commanded square velocities to pulse-width modulated signals according to the formula:

$$\delta_s = l\Omega_s^2 + mB + n, \text{ for } s = 1, .., 4,$$

where $\delta_.$ represents the PWM signal sent to the rotors, B is the measured battery voltage, and the constants l, m, and n are known and determined experimentally.

SINGLE ACTUATOR FAULT

In this scenario, an actuator fault is artificially injected by purposely corrupting the PWM signal corresponding to rotor $M1$. Specifically, at time $t \approx 25s$, a 20% loss of efficiency is introduced in the thrust generated by rotor $M1$.

Figure 7.2 and Figure 7.3 show the quadrotor altitude, attitude and position tracking, respectively. As can be seen, prior to the occurrence of the fault, the quadrotor closely tracks the desired trajectories. Immediately after time $t \approx 25s$, small tracking errors can be observed due to the loss of efficency in rotor $M1$. However, after a short transient time, the adaptive controller quickly adapts and is capable of maintaining satisfactory altitude, attitude and position tracking performance, even in the presence of an actuator fault.

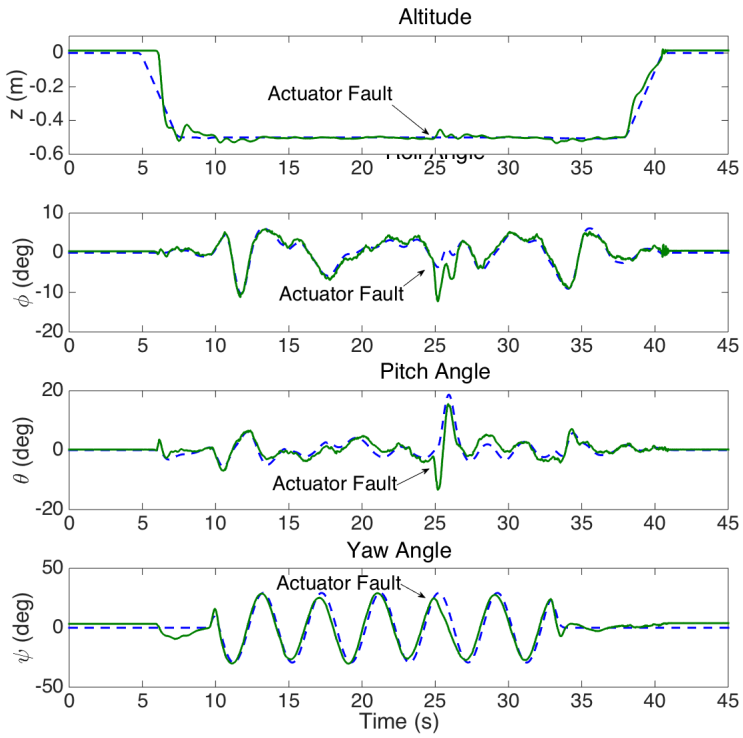

Figure 7.2: Altitude and attitude tracking with single actuator fault: desired trajectories are depicted in dashed blue line and actual quadrotor altitude and attitude angles are depicted in solid green line.

Figure 7.4 shows the controller commands generated by (7.17). As can be seen, shortly after $t = 25s$, the controller command corresponding to rotor $M1$ increases in an effort to compensate for the occurrence of a fault.

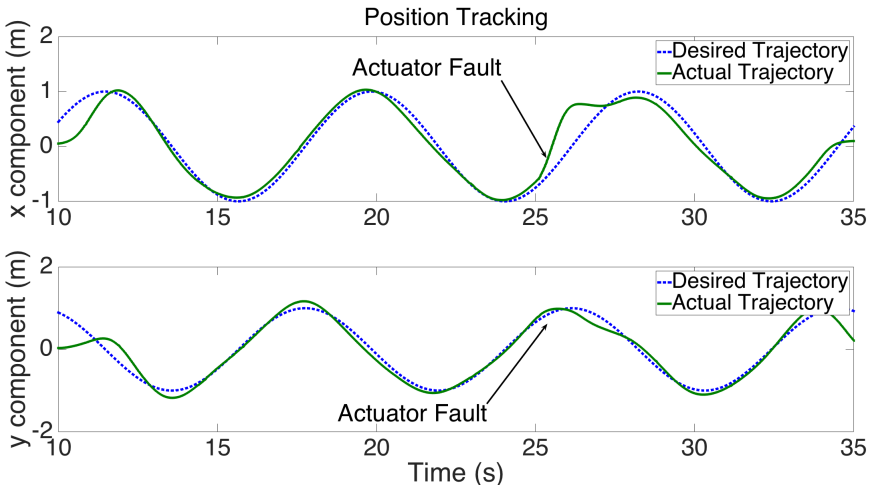

Figure 7.3: Position tracking with single actuator fault

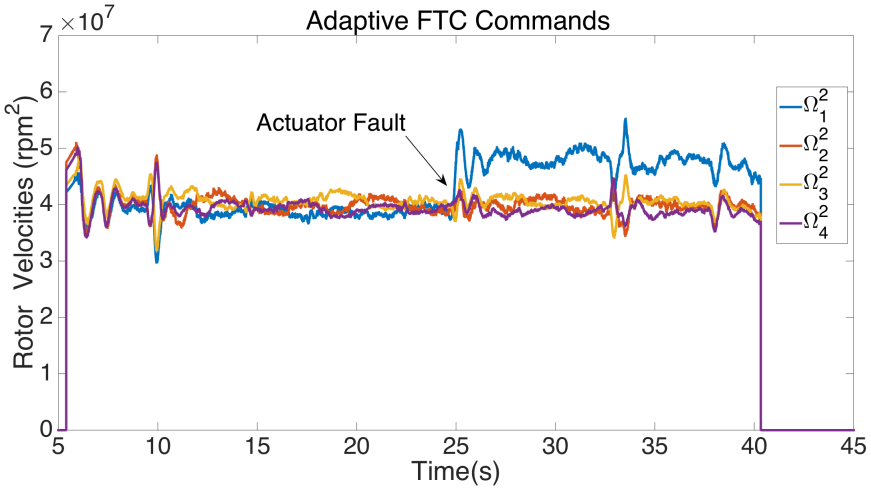

Figure 7.4: Adaptive fault-tolerant controller commands.

MULTIPLE SIMULTANEOUS ACTUATOR FAULTS

In this experiment we perform a longer run and sequentially inject simultaneous multiple faults. Specifically, Table 8.1, shows the time profiles and magnitude of the faults injected in the actuators. As can be seen, between times $t = 22s$ and $t = 35$, rotors $M1$ and $M2$ suffer from a 20% loss of efficiency in the thrust. Between times $t = 55s$ and $t = 72s$, simultaneous faults are introduced in rotors $M1$, $M2$, and $M3$ with 20%, 15%, and 12% loss of efficiency, respectively. Finally, at time $t = 90s$, four simultaneous faults are introduced for the remainder of the flight. Specifically, rotors $M1$, $M2$, $M3$, and $M4$ suffer from 15%, 10%, 15%, and 10% loss of efficiency, respectively.

Figure 7.5 shows the altitude and attitude tracking performance of the quadrotor for the case with 2 simultaneous actuator faults. As can be seen, the quadrotor alti-

t(s)	22 - 35	55 - 72	90 - 110
$M1$	20%	20%	15%
$M2$	20%	15%	10%
$M4$	-	12%	15%
$M3$	-	-	10%

Table 8.1: Quadrotor actuator fault magnitudes

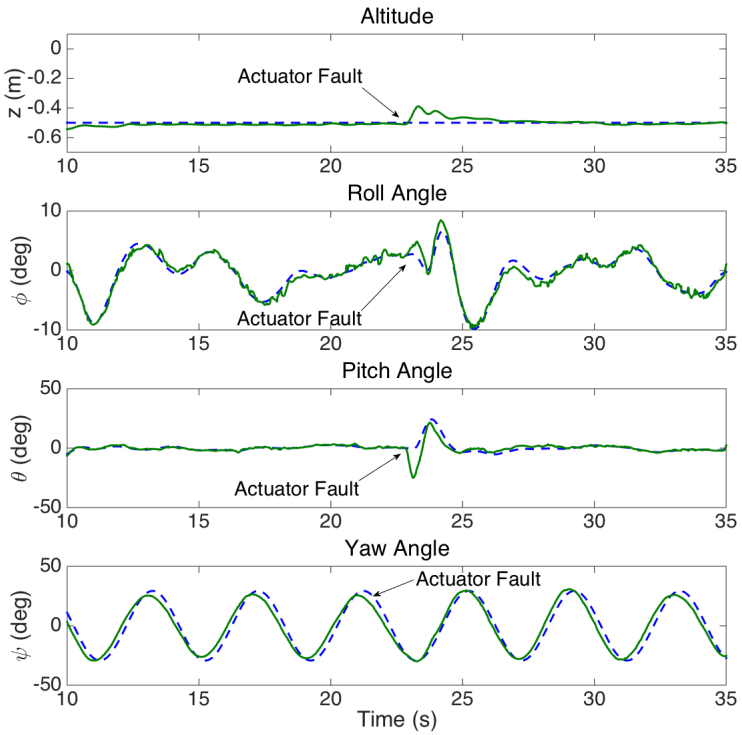

Figure 7.5: Altitude and attitude tracking with 2 simultaneous actuator faults: desired trajectories are depicted in dashed blue line and actual quadrotor altitude and attitude angles are depicted in solid green line.

tude and attitude tracking performance is recovered shortly after the occurrence of two simultaneous actuator faults. Note that only on the pitch angle and quadrotor altitude are significantly affected over a short duration of time by the loss of efficiency in the two rotors. This can intuitively be explained as follows. Referring to Figure 3.1, it can be seen that a loss of efficiency in rotors $M1$ and $M2$ would result in a loss of efficiency in the pitching torque and a loss of total thrust, which coincide with the pitch angle and altitude errors shown in Figure 7.5. Additionally, note that due to their physical location and opposing direction of spinning, a loss of equal magnitude in rotors $M1$ and $M2$ would have canceling effects on the rolling and yawing torque produced by the two rotors. Thus, a 20% in the rotors $M1$ and $M2$ has a negligible effect on the quadrotor

roll and yaw angles.

Figure 7.6 shows the altitude and attitude tracking performance of the quadrotor in the presence of three simultaneous faults. As can be seen, shortly after time $t = 55s$ a small tracking error can be observed. However, after a short transient period, the quadrotor resumes to closely track the desired trajectories.

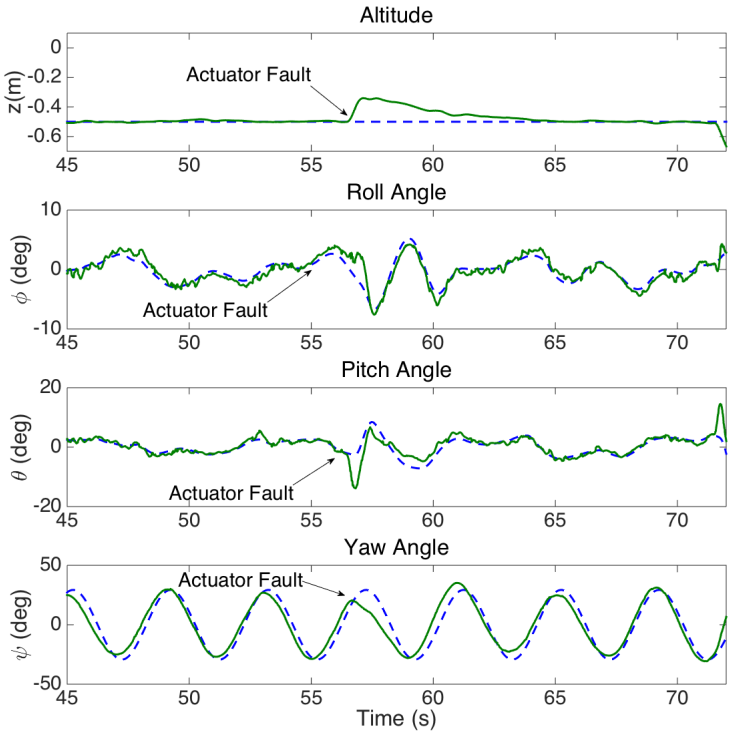

Figure 7.6: Altitude and attitude tracking with 3 simultaneous actuator faults: desired trajectories are depicted in dashed blue line and actual quadrotor altitude and attitude angles are depicted in solid green line.

Figure 7.6 shows the altitude and attitude tracking performance of the quadrotor when all rotors suffer from a loss of efficiency, as shown in Table 8.1. As can be seen, after time $t = 90s$, the most significant tracking errors can be observed in the quadrotor altitude, and only small errors are visible in the attitude angles. The sudden loss of efficiency in all four rotors results in a sudden loss of efficiency in the collective thrust which explains the large error in the altitude immediately after the occurrence of the faults. Given that all four rotor faults are relatively close to each other in magnitude, the small resulting attitude errors can be explained by following similar intuitive reasoning as in the case of two simultaneous faults considered earlier.

Figure 7.9 shows the commanded square velocities generated by (7.17). As can be

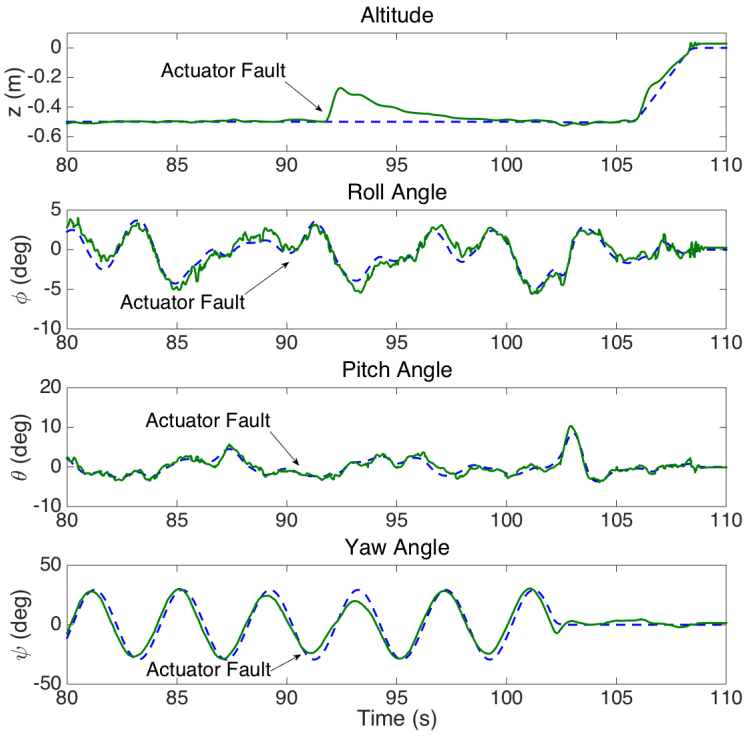

Figure 7.7: Altitude and attitude tracking with 4 simultaneous actuator faults: desired trajectories are depicted in dashed blue line and actual quadrotor altitude and attitude angles are depicted in solid green line.

seen, between time $t = 22s$ and $t = 35s$, the commanded rotor velocities corresponding to rotors $M1$ and $M2$ increase in an effort to compensate for the loss of effectiveness, while the commanded rotor velocities corresponding to rotors $M3$ and $M4$ are virtually unaffected by the occurrence of the faults. Similarly, between time $t = 55s$ and $t = 72s$, the commanded rotor velocities corresponding to rotors $M1$, $M2$, and $M3$ immediately respond to the presence of the three simultaneous faults, while the controller command corresponding to rotor $M4$ remains affected. Finally, after time $t = 90s$ all four rotor commands exhibit a increase in an effort to compensate for the sudden loss of thrust.

Figure 7.8 shows the position tracking performance of the quadrotor for the entire flight duration. As can be seen, in each case, shortly after the occurrence of the faults, the quadrotor is capable to maintain satisfactory position tracking performance even in the presence of actuator faults. In order to test the occurrence of simultaneous actuator faults, the loss of efficiency parameters are reset to zero in each case. Resetting the actual values of the actuator faults back to the nominal case (i.e. $\vartheta = [0, 0, 0, 0]^T$) has the reverse effect and appears as an additive fault (i.e. gain of efficiency) to the

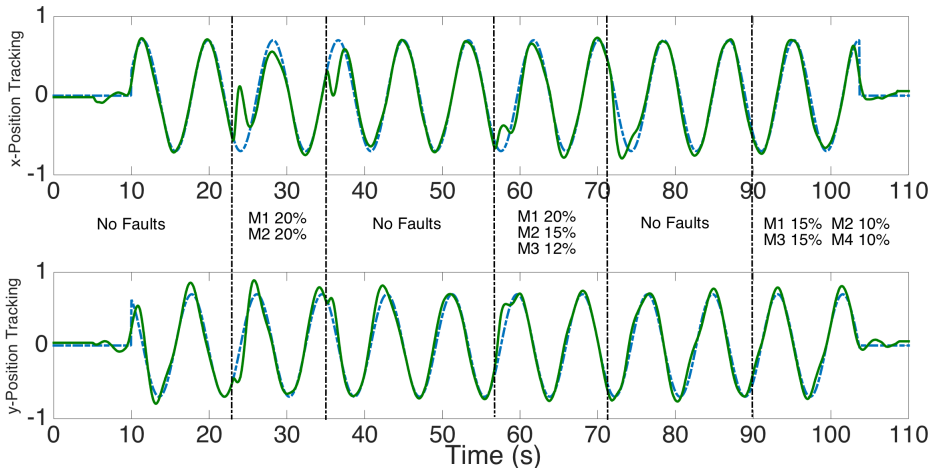

Figure 7.8: Position tracking with simultaneous multiple actuator faults

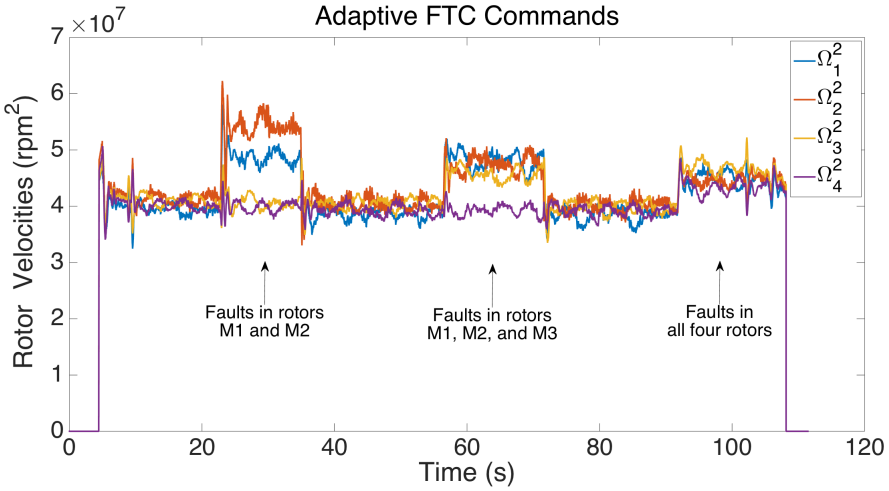

Figure 7.9: Adaptive fault-tolerant controller commands in the case of multiple simultaneous actuator faults.

adaptive altitude and attitude controller. This explains the small tracking errors after times $t = 35s$ and $t = 72s$ in Figure 7.8.

CONCLUSIONS

This chapter presents the design and experimental results of a fault-tolerant altitude and attitude control algorithm for quadrotor UAVs subject to actuator faults. By using a nonlinear adaptive back-stepping procedure, a new robust altitude and attitude controller is designed for accommodating possible multiple simultaneous actuator faults. The adaptation in the control algorithm arises due to the unknown fault magnitude, modeled as a loss of efficiency in the rotors. A robustifying control effort is added to account for unknown nonlinearities in the quadrotor dynamics. The control law guar-

antees the quadrotor altitude and attitude asymptotic stability even in the presence of multiple actuator faults. Experimental results are shown to illustrate the effectiveness of the proposed method. An interesting direction of future research is the extension of the proposed method to distributed systems consisting of multiple quadrotors.

VIII. ADAPTIVE FAULT-TOLERANT CONTROLLER INTEGRITY MONITORING FOR QUADROTOR UAVS

In order to enhance the reliability, safety, and survivability of UAVs, advanced adaptive control systems have attracted significant attention because of the potential to achieve superior control performance in the presence uncertainty or faults. Before such adaptive control systems can be adopted for use in safety-critical aerospace applications, it must be certified that the adaptive controller meet certain reliability and safety requirements. There have been significant research activities with exciting results in the research fields of software verification and validation (V&V) assuring satisfactory functionalities of software systems [32]. However, with the increasing levels of adaptation and autonomy in complex unmanned aerospace systems, the traditional notion that such systems can be fully tested and validated offline is becoming an impossible task [64, 65]. Run-time assurance (RTA) architectures provide a promising framework that can potentially maximize the use of advanced adaptive controllers with high performance capabilities, while ensuring the safety of the overall system in a run-time fashion [33, 66–68]. An important factor of RTAs is the online monitoring component that offers early detection of software faults and potential malfunctions of the adaptive controller, therefore allowing the timely activation of a fully certified simpler baseline controller to maintain system safety or to conduct degraded degradation.

In this chapter, we investigate the problem of run-time assurance (RTA) design for adaptive control of quadrotor UAVs using the general methodology described in [33]. Specifically, the adaptive altitude and attitude fault-tolerant controller described in Chapter 7 is considered. The adaptive algorithm guarantees closed-loop system stability and asymptotic tracking performance even in the presence of actuator faults. However, the occurrence of faults in the embedded adaptive control software may lead to unstable adaptation behaviors and malfunctions of the control algorithm. Based on Lyapunov stability criterion, an online controller integrity monitoring method is developed to detect the presence of such controller software faults. The fault detectability condition is rigorously analyzed, characterizing the class of software faults that are detectable by the proposed method. Real-time flight test results are shown to illustrate the effectiveness of the proposed RTA method for advanced quadrotor adaptive control systems.

PROBLEM FORMULATION: CONTROLLER SOFTWARE FAULT MODEL

In Chapter 7, a robust nonlinear fault-tolerant adaptive control law was designed for the quadrotor altitude and attitude system. The control objective was to design a control law for the quadrotor altitude and attitude dynamics given by (7.1) - (7.4), such that the quadrotor altitude z and attitude angles η track a desired differentiable reference trajectory even in the presence of actuator faults described by (7.7) and (7.11). Let us define the quadrotor altitude and attitude states as $x \triangleq [x_1^T,\, x_2^T]^T$ with

$$x_1 \triangleq [z,\, \phi,\, \theta,\, \psi]^T\,, \quad x_2 \triangleq [v_z,\, p,\, q,\, r]^T \tag{8.1}$$

where z and v_z represent the altitude and vertical inertial velocity, respectively. Then, the controller incorporating adaptive algorithms considered in this chapter takes the following general structure:

$$\dot{\hat{\vartheta}} = g_0(\hat{\vartheta}, x, x_{1d}, \bar{\Omega}) + \beta_1^c(t - T_1^c)\rho_1(\hat{\vartheta}, x, x_{1d}, \bar{\Omega}) \tag{8.2}$$

$$\bar{\Omega} = \Omega_0(\hat{\vartheta}, x, x_{1d}) + \beta_2^c(t - T_2^c)\rho_2(\hat{\vartheta}, x, x_{1d}) \tag{8.3}$$

where $\hat{\vartheta}$ is the state vector of the adaptive controller, $x_{1d} \triangleq [z_d,\, \phi_d,\, \theta_d,\, \psi_d]^T$ represents the desired altitude and attitude angles, $\bar{\Omega} \triangleq [\Omega_1^2,\, \Omega_2^2,\, \Omega_3^2,\, \Omega_4^2]^T$ (see (7.11)) represents squares of the commanded rotor velocities sent to the four rotors, g_0 and Ω_0 are nonlinear functions properly designed to satisfy the above control objective in the absence of controller software faults, and $\beta_1^c(t - T_1^c)\rho_1(\hat{\vartheta}, x, x_{1d}, \bar{\Omega})$ and $\beta_2^c(t - T_2^c)\rho_2(\hat{\vartheta}, x, x_{1d})$ represent the effects of faults in the real-time adaptive control software algorithm in the controller state and output equations, respectively. Specifically, the terms $\beta_1^c(\cdot)$ and $\beta_2^c(\cdot)$ are step functions with unknown fault occurrence times T_c^1 and T_c^2, respectively, and are defined as:

$$\beta_1^c(t - T_1^c) = \begin{cases} 0\,, & \text{when } t < T_1^c \\ 1\,, & \text{when } t \geq T_1^c \end{cases} \tag{8.4}$$

$$\beta_2^c(t - T_2^c) = \begin{cases} 0\,, & \text{when } t < T_2^c \\ 1\,, & \text{when } t \geq T_2^c\,. \end{cases} \tag{8.5}$$

The terms ρ_1 and ρ_2 represent the unknown software fault functions, possibly arising

from software bugs, bad design, or violation of assumptions made during the offline controller design and analysis process [33].

The aim of this chapter is to develop a controller integrity monitoring scheme for detecting controller software faults in the adaptive control software/algorithm described by (8.2) and (8.3).

CONTROLLER SOFTWARE FAULT DETECTION

In this section, we develop a controller integrity monitoring scheme to detect the occurrence of controller software faults (represented by ρ_1 in (8.2) and ρ_2 in (8.3)), which may lead to unstable adaptation behaviors and malfunctions of the adaptive controller described by (7.17) and (7.18).

Let us define the following residual signal for controller software fault detection:

$$\varepsilon(t) \triangleq ||z_1||^2 + ||z_2||^2 \,. \tag{8.6}$$

Recall, in the proof of Theorem 7.1, we showed that the Lyapunov function candidate:

$$V = \frac{1}{2} z_1^T z_1 + \frac{1}{2} z_2^T z_2 + \sum_{s=1}^{4} \frac{1}{2\sigma_s} \tilde{\vartheta}_s^2 \,, \tag{8.7}$$

satisfies

$$\dot{V} \leq -z_1^T k_1 z_1 - z_2^T c_3 z_2 \,. \tag{8.8}$$

Then, based on (8.6), in the absence of controller software faults (i.e. for $t < \min\{T_1^c, T_2^c\}$), it follows that:

$$\varepsilon(t) \leq 2V(t) \,. \tag{8.9}$$

Let us define $\bar{k}_1 \triangleq ||k_1||$ and $\bar{c}_3 \triangleq ||c_3||$, where $||\cdot||$ represents the vector norm operator. By integrating (8.8) over some time interval $[t_0, t]$, we obtain:

$$V(t) = V(t_0) - \int_{t_0}^{t} (\bar{k}_1 ||z_1||^2 + \bar{c}_3 ||z_2||^2) d\tau \,, \tag{8.10}$$

Therefore, by using (7.27), (8.9), and (8.10), we have:

$$\begin{aligned}\varepsilon(t) &\leq 2V(t_0) - 2\int_{t_0}^{t}(\bar{k}_1||z_1||^2 + \bar{c}_3||z_2||^2)d\tau \\ &\leq ||z_1(t_0)||^2 + ||z_2(t_0)||^2 + \sum_{s=1}^{4}\sigma_s^{-1}\tilde{\vartheta}_s^{\,2}(t_0) - 2\int_{t_0}^{t}(\bar{k}_1||z_1||^2 + \bar{c}_3||z_2||^2)d\tau\,,\end{aligned}$$

where $z_1(t_0)$, $z_2(t_0)$, and $\tilde{\vartheta}_s^{\,2}(t_0)$ represent initial conditions at t_0. Note that the above threshold cannot be implemented due to the unknown initial parameters estimation error $\tilde{\vartheta}_s(t_0)$, for $s = 1, .., 4$. However, based on the actuator fault model presented in Chapter 7, the parameter estimate $\hat{\vartheta}_s(t)$ belongs to a known compact set $\Theta = [0,\, \bar{\vartheta}_s]$, we have $|\vartheta_s - \hat{\vartheta}_s| < \kappa_s(t)$. Based on the geometric properties of the set Θ, we have

$$\kappa_s(t) = \frac{\bar{\vartheta}_s}{2} + |\hat{\vartheta}_s - \frac{\bar{\vartheta}_s}{2}|\,. \tag{8.11}$$

Thus, the detection threshold for controller software faults can be chosen as:

$$\mu \triangleq \sum_{s=1}^{4}\sigma^{-1}\kappa_s^2(t_0) + ||z_1(t_0)||^2 + ||z_2(t_0)||^2 - 2\int_{t_0}^{t}(\bar{k}_1||z_1||_2^2 + \bar{c}_3||z_2||_2^2)d\tau\,. \tag{8.12}$$

Then, we have the following:

Fault detection decision scheme: *The decision for the occurrence of unstable adaptation behaviors caused by a controller software fault is made when the residual signal $\varepsilon(t)$ exceeds its corresponding threshold $\mu(t)$. More precisely, the controller malfunction detection time T_d is defined as the first instant of time such that $\epsilon(t) \geq \mu(t)$; that is $T_d \triangleq \min\{t > 0 : \epsilon(t) > \mu(t)\}$.*

CONTROLLER SOFTWARE FAULT DETECTABILITY ANALYSIS

In the fault detection process, there is always an inherent tradeoff between robustness and fault sensitivity. In this section, we investigate the detectability property of the proposed controller software fault detection method. Suppose that a software fault occurs at some time $T_0 = \min\{T_1^c,\, T_2^c\}$. The following theorem characterizes implicitly the class of software/controller faults that are detectable by the proposed method:

Theorem 8.1. *Consider the quadrotor altitude and attitude system dynamics with*

the adaptive controller described by (7.18) and (7.17) subject to software faults ρ_1 and and ρ_2 in (8.2) and (8.3). The software fault detection scheme guarantees that, if there exists some time interval $[T_1, T_d]$ with $T_d > T_1 \geq T_0$, such that

$$\int_{T_1}^{T_d} \Big(\sum_{s=1}^{4} (\sigma_s^{-1} \tilde{\vartheta}_s \beta_1^c \rho_1) + z_2^T \varphi \beta_2^c \rho_2 \Big) d\tau \geq \int_{T_1}^{T_d} \sum_{s=1}^{4} \kappa_s(t) |\zeta_s| d\tau + \frac{1}{2} \sum_{s=1}^{4} \sigma_s^{-1} \Big(\kappa_s^2(T_1) + \kappa_s^2(t) \Big) \tag{8.13}$$

where

$$\varphi(x_1, \hat{\vartheta}) \triangleq g_2(x_1) M (I_4 - \hat{\vartheta} \Lambda_s)\,, \tag{8.14}$$

then the fault will be detected at time $t = T_d$, i.e. $\varepsilon(T_d) > \mu(T_d)$.

Proof. In the presence of a controller software fault (i.e., for $t \geq T_0$), we can rewrite the adaptive control law given in Theorem 7.1 under the general structure of (8.2) and (8.3) as

$$\dot{\hat{\vartheta}}_s = \mathcal{P}_\Theta \{ -\sigma_s z_2^T g_2(x_1) M \Lambda_s \bar{\Omega} \} + \beta_1^c (t - T_1^c) \rho_1(\hat{\vartheta}, x, x_{1d}, \bar{\Omega}) \tag{8.15}$$

$$\begin{aligned} \bar{\Omega} = & \left[g_2(x_1) M \left(I_4 - \sum_{s=1}^{4} (\hat{\vartheta}_s \Lambda_s) \right) \right]^{-1} \times \left(- f_2(x_1, x_2) + \dot{\alpha} - (c_1 g_1(x_1))^T z_1 - c_3 z_2 \right) \\ & - \left[I_4 - \sum_{s=1}^{4} (\hat{\vartheta}_s \Lambda_s) \right]^{-1} \times \operatorname{diag}\{\operatorname{sgn}(H)\} \bar{\xi}^*(x, t) \\ & + \beta_2^c (t - T_1^c) \rho_2(\hat{\vartheta}_s, x, x_{1d})\,. \end{aligned} \tag{8.16}$$

See Chapter 7 for the description of the parameters in the above adaptive control law. Let us recall the dynamics of the new states z_1 and z_2 described in (7.24) and (7.26), respectively:

$$\dot{z}_1 = c_1 g_1(x_1) z_2 - k_1 z_1 \tag{8.17}$$

$$\begin{aligned} \dot{z}_2 = & f_2(x_1, x_2) - \dot{\alpha} \\ & + g_2(x_1) M \left[\left(I_4 - \sum_{s=1}^{4} \hat{\vartheta}_s \Lambda_s \right) \bar{\Omega} + \xi^*(x, t) \right] \\ & + g_2(x_1) M \left(\sum_{s=1}^{4} \tilde{\vartheta}_s \Lambda_s \right) \bar{\Omega} \end{aligned} \tag{8.18}$$

By substituting the control law (8.16) into (8.18), we have

$$\begin{aligned}\dot{z}_2 = &-(c_1 g_1(x_1))^T z_1 - c_3 z_2 \\ &+ g_2(x_2) M \left(-\text{diag}\{\text{sgn}(H)\}\bar{\xi^*}(x,t) + \xi^*(x,t)\right) \\ &+ g_2(x_2) M (\sum_{s=1}^{4} \tilde{\vartheta}_s \Lambda_s)\bar{\Omega} + \varphi(x_1, \hat{\vartheta})\beta_2^c(t - T_2^c)\rho_2(\hat{\vartheta}, x, x_{1d})\,, \end{aligned} \tag{8.19}$$

where $\varphi(x_1, \hat{\vartheta})$ is defined in (8.14) and H is defined in (7.21). Now, consider the Lyapunov function given by (7.27). Then, the time derivative of V along the solutions of (8.17), (8.19), and (8.15) is given by:

$$\begin{aligned}\dot{V} &= z_1^T(c_1 g_1 z_2 - k_1 z_1) + \sum_{s=1}^{4} \sigma_s^{-1} \tilde{\vartheta}_s \dot{\hat{\vartheta}}_s \\ &\quad + z_2^T\Big(- (c_1 g_1)^T z_1 - c_3 z_2\Big) + H\Big(- \text{diag}\{\text{sgn}(H)\}\bar{\xi^*}(x,t) + \xi^*(x,t)\Big) \\ &\quad + z_2^T g_2 M (\sum_{s=1}^{4} \tilde{\vartheta}_s \Lambda_s)\bar{\Omega} + z_2^T \varphi \beta_2^c \rho_2 \\ &= -z_1^T k_1 z_1 - z_2^T c_3 z_2 - H\Big(\text{diag}\{\text{sgn}(H)\}\bar{\xi^*}(x,t) + \xi^*(x,t)\Big) + z_2^T \varphi \beta_2^c \rho_2 \\ &\quad + z_2^T g_2 M (\sum_{s=1}^{4} \tilde{\vartheta}_s \Lambda_s)\bar{\Omega} - \sum_{s=1^4} \Big[\tilde{\vartheta}_s\Big(z_2^T g_2(x_2) M \Lambda_s \bar{\Omega} - \zeta_s\Big) + \tilde{\vartheta}_s \beta_1^c \rho_1\Big] \\ &= -z_1^T k_1 z_1 - z_2^T c_3 z_2 + H\Big(- \text{diag}\{\text{sgn}(H)\}\bar{\xi^*}(x,t) + \xi^*(x,t)\Big) + \sum_{s=1}^{4} \tilde{\vartheta}_s \zeta_s \\ &\quad + \sum_{s=1}^{4} \sigma_s^{-1} \tilde{\vartheta}_s \beta_1^c \rho_1 + z_2^T \varphi \beta_2^c \rho_2\,. \end{aligned} \tag{8.20}$$

Integrating (8.20) from time T_1 to t and by applying the vector norm operator, we obtain:

$$\begin{aligned}V(t) = V(T_1) &- \int_{T_1}^{t} (\bar{k}_1 ||z_1||^2 + \bar{c}_3 ||z_2||^2) d\tau + \int_{T_1}^{t} H\Big(- \text{diag}\{\text{sgn}(H)\}\bar{\xi^*}(x,\tau) + \xi^*(x,\tau)\Big) d\tau \\ &+ \int_{T_1}^{t} \sum_{s=1}^{4} (\tilde{\vartheta}_s \zeta_s) d\tau + \int_{T_1}^{t} \left(\sum_{s=1}^{4} \sigma_s^{-1} \tilde{\vartheta}_s \beta_1^c \rho_1 + z_2^T \varphi \beta_2^c \rho_2\right) d\tau\,. \end{aligned} \tag{8.21}$$

Based on the bound on the parameter estimation error (8.11) and the definition of the Lyapunov function (7.27), we have:

$$||z_1||_2^2 + ||z_2||_2^2 + \sum_{s=1}^{4} \sigma_s^{-1} \kappa_s^2(t) \geq 2V(t)\,. \tag{8.22}$$

Then, by using (8.6), (8.21), and (8.22), we obtain

$$\begin{aligned}\varepsilon(t) &\geq 2V(t) - \sum_{s=1}^{4} \sigma_s^{-1}\kappa_s^2(t) \\ &\geq 2V(T_1) - \sum_{s=1}^{4} \sigma_s^{-1}\kappa_s^2(t) - 2\int_{T_1}^{t} (\bar{k}_1||z_1||^2 + \bar{c}_3||z_2||^2)d\tau \\ &\quad + 2\int_{T_1}^{t} H\Big(- \mathrm{diag}\{\mathrm{sgn}(H)\}\bar{\xi^*}(x,\tau) + \xi^*(x,\tau)\Big)d\tau \\ &\quad + 2\int_{T_1}^{t} \sum_{s=1}^{4} (\tilde{\vartheta}_s\zeta_s)d\tau + 2\int_{T_1}^{t} \left(\sum_{s=1}^{4} (\sigma_s^{-1}\tilde{\vartheta}_s\beta_1^c\rho_1) + z_2^T\varphi\beta_2^c\rho_2\right) d\tau\,. \end{aligned} \tag{8.23}$$

By recalling the model uncertainty bound described by (7.6) and by using similar techniques as in the proof of Theorem 7.1 it can be verified that:

$$H\Big(- \mathrm{diag}\{\mathrm{sgn}(H)\}\bar{\xi^*}(x,\tau) + \xi^*(x,\tau)\Big) \leq 0\,. \tag{8.24}$$

Additionally, note that the threshold $\mu(t)$ in (8.12) can be rewritten as:

$$\mu(t) = \sum_{s=1}^{4} \sigma_s^{-1}\kappa_s^2(T_1) + ||z_1(T_1)||^2 + ||z_2(T_1)||^2 - 2\int_{T_1}^{t} (\bar{k}_1||z_1||^2 + \bar{c}_3||z_2||^2)d\tau\,. \tag{8.25}$$

By making use of (8.22) and (8.25), and after some algebraic manipulations, it can be shown that

$$\begin{aligned}\varepsilon(t) \geq &\mu(t) + 2\int_{T_1}^{t} \sum_{s=1}^{4} (\tilde{\vartheta}_s\zeta_s)d\tau - \sum_{s=1}^{4} \sigma_s^{-1}\Big(\kappa_s^2(T_1) + \kappa_s^2(t)\Big) \\ &+ 2\int_{T_1}^{t} \left(\sum_{s=1}^{4} (\sigma_s^{-1}\tilde{\vartheta}_s\beta_1^c\rho_1) + z_2^T\varphi\beta_2^c\rho_2\right) d\tau \end{aligned}$$

Therefore, if there exists some $T_d \geq T_1$ such that condition (8.13) is satisfied, then we can conclude that $\varepsilon(T_d) \geq \mu(T_d)$, i.e. the controller software fault is detected at time $t = T_d$. □

Remark 8.1 . Note that the term on the left-hand side of (8.13) represents the overall effect of software faults on system stability, while the right-hand side represents the effect of uncertainties in the controller monitoring problem (for instance, the parameter estimation error represented by $\kappa(t)$). In qualitative terms, the fault detectability theorem implies that, if during a certain time window $[T_1, T_d]$, the effect of the software

faults becomes sufficiently large with respect to the uncertainties, then the fault can be detected.

EXPERIMENTAL RESULTS

In this section, we present some experimental results in order to illustrate the effectiveness of the online controller monitoring scheme. The fault-tolerant altitude and attitude control algorithm described in Chapter 7 and the controller monitoring algorithm described in this chapter are implemented and execute on-board of the quadrotor.

Figure 8.1 shows the run-time assurance architecture for quadrotor adaptive control. Two controllers are designed to execute on-board: *(1) Advanced Adaptive Controller*, and *(2) Baseline Controller*. The *advanced adaptive controller* presented in Chapter 7 is deployed on-board of the quadrotor and acts as the primary controller in order to provide improved overall tracking performance and actuator fault-tolerance. The *baseline controller* is designed using linear control design techniques (e.g. PID) and is tuned to provide satisfactory stabilization capability at certain flight conditions. Due to its controller architecture limitations (e.g. fixed gains), the baseline controller has inferior tracking performance when compared to the adaptive controller. However, in the presence of software faults in the advanced adaptive controller, the baseline controller can be used to quickly stabilize and safely land the quadrotor. Specifically, adaptive controller outputs and sensor measurements are used by the real-time adaptive controller integrity monitoring algorithm for detecting possible faults in the advanced control software. Once a software fault is detected, a switching mechanism is engaged, and the baseline controller signals are selected for the remainder of quadrotor flight time.

In order to evaluate the presented nonlinear adaptive control algorithm and controller integrity monitoring scheme, real-time flight tests for the following two cases are conducted: actuator fault only and simultaneous actuator and controller software fault. In both experiments the quadrotor is commanded to perform a circular maneuver with a radius of 1 meter at a constant altitude while following a sinusoidal orientation. Trajectory control of the quadrotor is achieved using a double-loop architecture. Specifically, the outer loop controls the p_x and p_y positions by generating desired roll and pitch angles. The *altitude and attitude control loop*, employing the run-time assurance architecture shown in Figure 8.1, generates the required rotor velocities needed for the

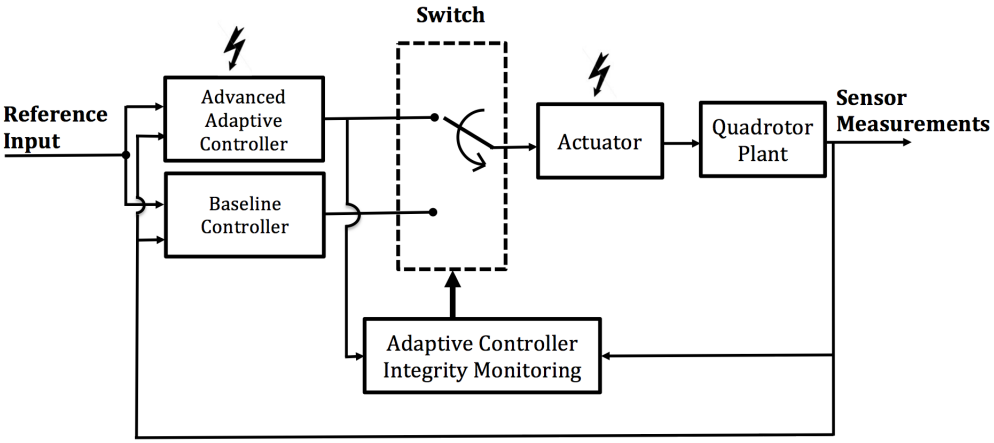

Figure 8.1: Run-time assurance architecture for quadrotor adaptive control.

quadrotor to track the desired attitude and altitude trajectories.

The experimental results are presented in the following two sections. A video recording of the experiments is posted online [69].

EXPERIMENTAL RESULTS WITH ONLY ACTUATOR FAULT

In the first experiment, a 20% loss of effectiveness is artificially injected at time $T_s^a \approx 25\,\text{sec}$, by purposely corrupting the PWM input corresponding to rotor $M1$. Figure 8.2 shows the residuals generated by (8.6). As can be seen, the controller fault detection residual always remains below the detection threshold. Additionally, Figure 8.3 and Figure 8.4 show the quadrotor altitude, attitude and position tracking, respectively. For simplicity a fixed detection threshold is chosen. As can be seen shortly after the occurrence of the fault, the adaptive controller quickly adapts and is capable to maintain good tracking performance even in the presence of an actuator fault.

EXPERIMENTAL RESULTS WITH SIMULTANEOUS ACTUATOR AND CONTROLLER SOFTWARE FAULTS

In the second experiment, the advanced adaptive control law is purposely corrupted with a software bug. Additionally, at time $T_s^a \approx 23.5\,\text{s}$, an actuator fault is injected in rotor $M1$. Once a controller software fault is detected, the quadrotor switches to the baseline controller and is commanded to land for safety assurance. Specifically, the software fault is represented by a sign bug [70] in the adaptive law (7.18) and is present in the controller for the entire flight duration. In other words, the fault function ρ_1 in

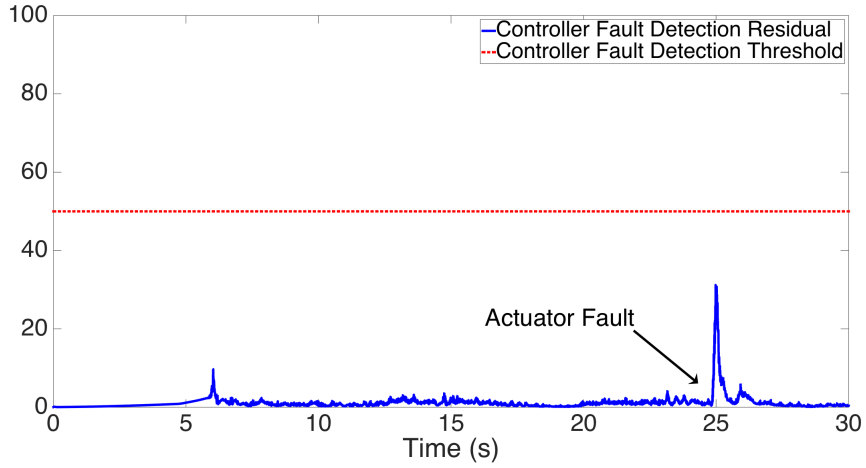

Figure 8.2: Adaptive controller software fault monitoring: case of only actuator faults.

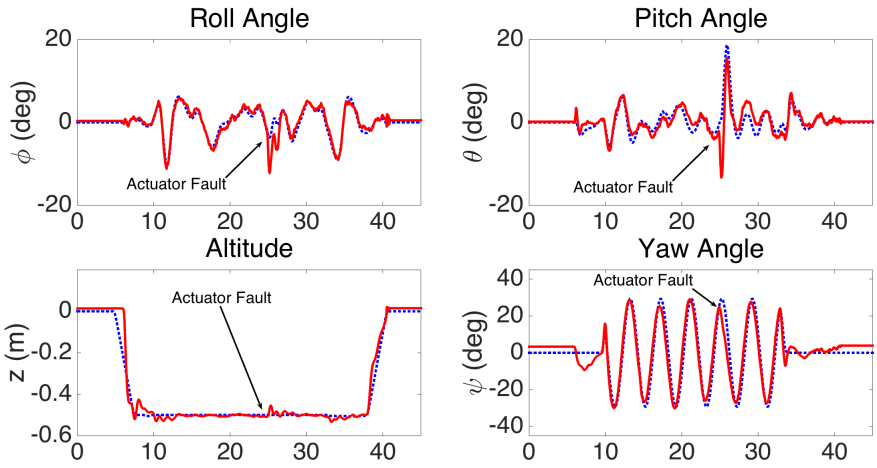

Figure 8.3: Quadrotor altitude and attitude with actuator faults only: desired trajectories (dashed blue line) and actual altitude and attitude angles (solid red line).

(8.15) is given by:

$$\rho_2(x, \hat{\vartheta}, \bar{\Omega}, t) = 2\mathcal{P}_\Theta\{\sigma z_2^T g_2(x_1) M \Lambda_s \bar{\Omega}\}\,.$$

Note that in the presence of actuator faults, the unanticipated software fault is beyond the handling capability of the adaptive controller and would lead the quadrotor to crash if unattended.

Figure 8.5 shows the results of controller software fault detection. As can be seen, shortly after the occurrence of the fault, the residual signal generated by (8.6) exceeds the detection threshold at time $T_d \approx 25\,\text{sec}$, indicating the occurrence of a fault in the advanced control algorithm. As a result, the baseline controller is activated to safely land the quadrotor. It is worth noting that the software detection residual is computed based

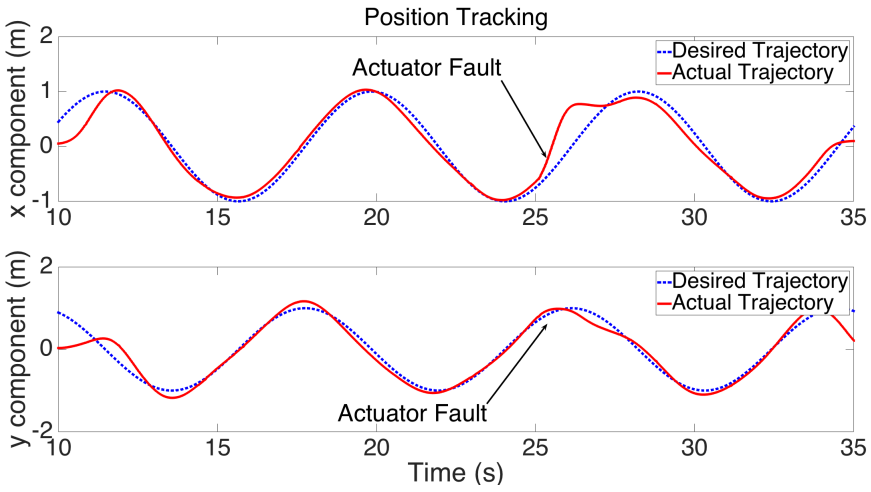

Figure 8.4: Quadrotor position tracking: case of actuator faults only.

on the signals z_1 and z_2 which are used in the adaptive FTC law (see (8.15) and (8.16)). Therefore, once the baseline controller is activated, (i.e. for $t > T_d$), the software faults in the adaptive controller (which is not active at this time) are not detectable anymore by the residual $\epsilon(t)$.

Figure 8.6 shows the quadrotor altitude and attitude tracking performance. As can be seen, the quadrotor altitude and attitude tracking performance quickly degrades shortly after the occurrence of the simultaneous actuator and controller faults. However, with the run-time assurance method, the quadrotor is able to safely land albeit with degraded tracking performance.

Figure 8.7 shows the position tracking of the quadrotor. As can be seen, shortly after the occurrence of the faults the quadrotor position drifts away along the positive

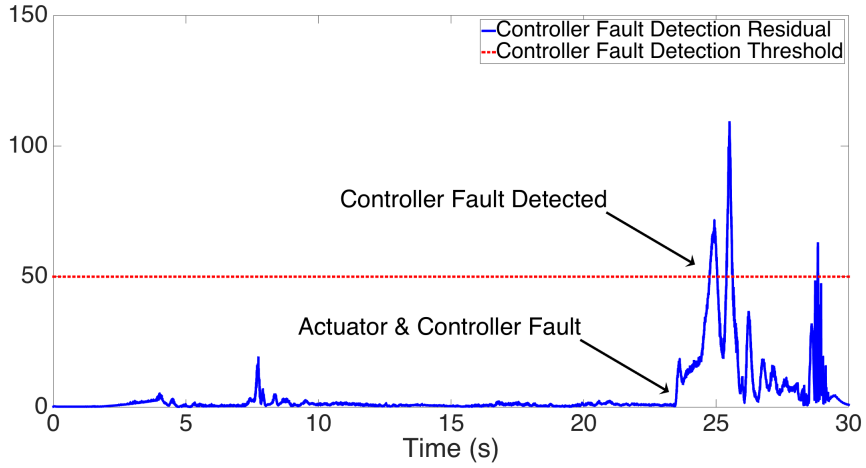

Figure 8.5: Quadrotor controller fault monitoring: case of simultaneous actuator controller fault.

p_x and negative p_y direction. This is a direct result of the wrong adaptation direction in the adaptive law (7.18). Note that a gross error in the quadrotor p_y position persists, even after the quadrotor switches to the baseline controller, illustrating the limitations of the fixed gain baseline controller.

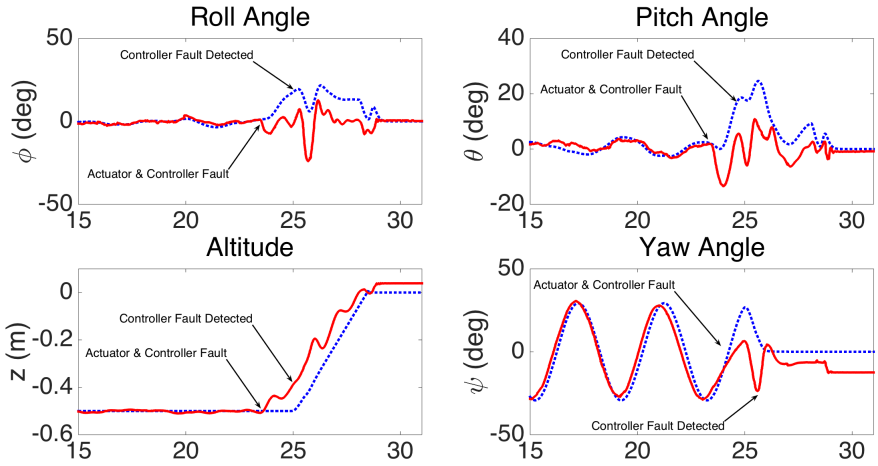

Figure 8.6: Quadrotor attitude tracking: case of simultaneous actuator controller fault. Desired trajectories are depicted in dashed blue line. Actual altitude and attitude angles are depicted in solid red line.

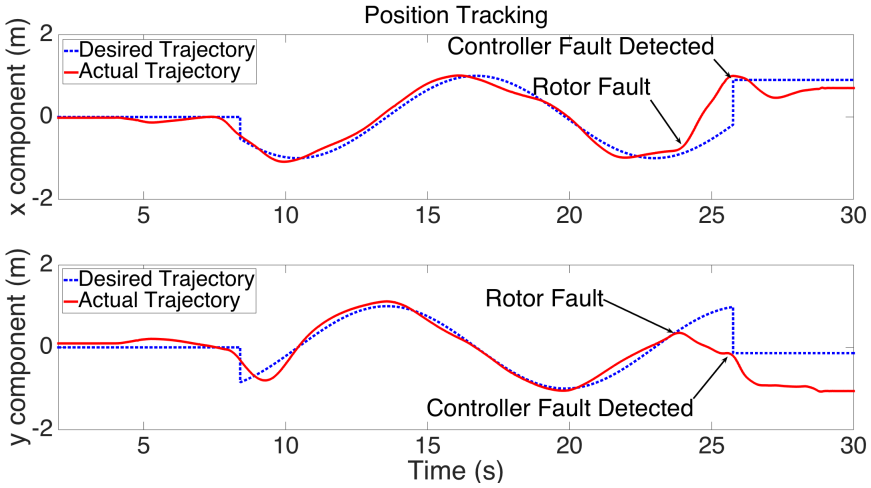

Figure 8.7: Quadrotor position tracking: case of simultaneous actuator controller fault.

CONCLUSIONS

In this section, a run-time assurance method for nonlinear adaptive control of quadrotor UAVs is investigated. A controller integrity monitoring algorithm is designed to detect faults in the advanced controller software, which is a key component of the RTA architecture for trusted autonomy. The fault detectability property of the controller in-

tegrity monitoring algorithm is rigorously established. Fault detection information from the controller integrity monitoring algorithm is used to activate controller switching and conduct graceful degradation for safety assurance. Experimental results are shown to illustrate the effectiveness of the proposed algorithms. An interesting direction for future research is the extension of the proposed methods to distributed systems consisting of multiple quadrotors.

IX. CONCLUSION AND FUTURE RESEARCH

Due to their potentials in military and commercial applications, quadrotor UAVs have experienced a continuous growth in recent years. However, as a result of the intrinsic fabrication process and component damage, quadrotors are prone to various sensor and actuator faults which can lead to failed missions and potential catastrophic outcomes. The research presented in this dissertation aims to enhance the reliability, survivability and autonomy of quadrotor UAVs. Specifically, using nonlinear adaptive techniques, sensor and actuator fault diagnosis and fault-tolerant controllers are developed. The algorithms are presented with a rigorous analytical framework aimed at characterizing their performance properties and are implemented and evaluated using a real-time indoor quadrotor test environment.

First, the issue of IMU sensor faults is investigated. Simultaneous accelerometer and gyroscope sensor faults are diagnosed using structured residuals. A nonlinear sensor IMU fault diagnosis is developed for the case when all attitude angles are measurable. The robustness of the diagnosis algorithm is analyzed in the presence of sensor measurement noise. Then, the critical assumption that roll and pitch angles are measurable is removed. By employing sliding-mode theory a robust roll and pitch angle estimation algorithm is developed. Based on the estimated roll and pitch angles, a nonlinear sensor fault diagnosis algorithm is designed to detect, isolate, and estimate possible simultaneous biases in accelerometer and gyroscope measurements. The stability properties of the roll and pitch estimator and of the proposed sensor fault estimation algorithms are rigorously established.

Second, the issue of actuator faults is investigated. In Chapter 6, a fully nonlinear framework for integrated quadrotor actuator fault diagnosis and fault accommodation is formulated. A robust actuator fault detection algorithm is implemented and adaptive fault detection thresholds are systematically designed to achieve enhanced robustness and fault sensitivity properties. Additionally, adaptive matched FIEs are designed for fault isolation. After fault isolation, the fault magnitude estimate provided by the matched FIE is used for accommodating the effect of the faults. Then, In Chapter 7, a nonlinear adaptive fault-tolerant altitude and attitude controller is developed to automatically stabilize and recover tracking performance of the quadrotor, even in the presence of possible multiple simultaneous actuator faults. Compared with the approach

in Chapter 6, the adaptive control framework can automatically accommodate the effects of actuator faults without the need of a fault diagnosis mechanism. The controller guarantees asymptotic tracking performance even in the presence of multiple simultaneous faults.

Finally, in Chapter 8, based on the general methodology in [33], a monitoring algorithm is implemented for detecting software faults in the advanced adaptive controller. Adaptive thresholds are derived for improved robustness. A run-time assurance architecture is implemented for assuring the safety of the adaptive controller in the presence of software faults.

In this dissertation, it is assumed that the quadrotor system is only subject to a particular type of fault. Specifically, in the design and analysis process of sensor fault diagnosis algorithms, actuator faults are not considered. Similarly, in the design and analysis process of actuator fault diagnosis and FTC algorithms, it is assumed that IMU sensor measurements are not subject to faults. The coupling between on-board sensor measurements and forces acting on the quadrotor body in the quadrotor dynamics makes the isolation problem between different fault types more challenging. As a result, an interesting direction for future research is the development of a fault diagnosis and fault-tolerant control system, which is capable to detect, isolate, estimate, and accommodate sensor and actuator faults under a unified framework.

Additionally, the development of advanced formation control of quadrotor UAVs has received considerable interests in recent years due to its broad potential applications in civilian and military areas, such as surveillance and reconnaissance [71], localization [72], telecommunication relay [73], etc. Compared with a single platform, cooperative autonomous unmanned aerial vehicles (UAVs) offer a wider area of operation with improved efficiency in performing more complex tasks. In most centralized and decentralized formation control architectures another layer of communication is added, linking some or all quadrotors in the swarm. However, sensor or actuator faults in one or more quadrotors as well as faults in the communication layer can lead to loss of formation and degrade the overall control architecture. As a result, the investigation of distributed fault diagnosis and fault-tolerant control with application to a multiple agent systems consisting of multiple quadrotors is of great interest.

BIBLIOGRAPHY

[1] Teal Group. (2013, June) Teal group predicts worldwide UAV market will total $89 billion in its 2013 UAV market profile and forecast. [Online]. Available: http://tealgroup.com/index.php/about-teal-group-corporation/press-releases/94-2013-uav-press-release

[2] US Dept. of Defense, "Unmanned systems integrated roadmap FY2011-2036," Secretary of Defense, Washington, D.C., Tech. Rep., 2012.

[3] T. Shima and S. Rasmussen, "UAVreppa:cra2006 cooperative decision and control," T. Shima and S. Rasmussen, Eds. Society for Industrial and Applied Mathematics, 2009. [Online]. Available: http://epubs.siam.org/doi/abs/10.1137/1.9780898718584

[4] US Dept. of Defense, "Unmanned systems integrated roadmap, FY2000-2025," Secretary of Defense, Washington, D.C., Washington, D.C., Tech. Rep., 2000.

[5] R. Isermann, *Fault-Diagnosis Systems.* Berlin-Heidelberg: Springer, 2006.

[6] M. Blanke, M. Kinnaert, J. Lunze, and M. Staroswiecki, *Diagnosis and Fault-Tolerant Control.* Berlin-Heidelberg: Springer, 2006.

[7] R. J. Patton and J. Chen, *Model-Based Fault Diagnosis for Dynamic Systems.* New York, USA: Kluwer Academic Publishers, 1999.

[8] V. Reppa and A. Tzes, "Application of set memebership identification for fault detection of MEMS," in *IEEE International Conference on Robots and Automation*, Orlando, FL, 2006, pp. 643–648.

[9] F. López-Estrada, J.-C. Ponsart, D. Theilliol, Y. Zhang, and C.-M. Astorga-Zaragoza, "LPV model-based tracking control and robust sensor fault diagnosis for a quadrotor UAV," *Journal of Intelligent & Robotic Systems*, pp. 1–15, 2015.

[10] Y. Zhang, A. Chamseddine, C. Rabbath, B. Gordon, C. Su, S. Rakheja, C. Fulford, J. Apkaraian, and P. Gosselin, "Development of advanced FDD and FTC techniques with application to an unmanned quadrotor helicopter testbed," *Journal of the Franklin Institue*, vol. 350, no. 9, pp. 2396–2422, 2013.

[11] A. Freddi, S. Longhi, and A. Monteriu, "A diagnostic Thau observer for a class of unmanned vehicles," *Journal of Intelligent & Robotic Systems*, pp. 61–73, 2012.

[12] H. V. Nguyen, C. Berbra, S. Lesecq, S. Gentil, A. Barraud, and C. Godin, "Diagnosis of an inertial measurement unit based on set membership estimation," in *Control and Automation, 2009. MED '09. 17th Mediterranean Conference on*, June 2009, pp. 211–216.

[13] Y. Younes, H. Noura, A. Rabhi, H. A.E., and N. Hussien, "Sensor fault detection and isolation in the quadrotor vehicle using nonlinear identity observer approach," in *2013 Conference on Control and Fault-Tolerant Systems*, Nice, France, 2013, pp. 486–491.

[14] H. Rafaralahy, E. Richard, M. Boutayeb, and M. Zasadzinski, "Simultaneous observer based sensor diagnosis and speed estimation of unmanned aerial vehicle," in *IEEE Conference on Decision and Control*, Cancun, 2008, pp. 2938–2943.

[15] C. Berba, S. Lesecq, and J. Maritinez, "A multi-observer switching strategy for fault-tolerant control of a quadrotor helicopter," in *16th Mediterranean Conference on Control and Automation*, 2008, pp. 1094–1099.

[16] C. Berbra, S. Gentil, and S. Lesecq, "Identification of multiple faults in an inertial measurment unit," in *7th Workshop on Advanced Control and Diagnosis, ACD*, 2009.

[17] J. Macdonald, R. Leishman, R. Beard, and T. McLain, "Analysis of an improved IMU-based observer for multirotor helicopters," *Journal of Intelligent Robotic Systems*, vol. 64, pp. 1049–1061, 2014.

[18] M. Ireland and D. Anderson, "Development of navigation algorithms for NAP-of-the-earth UAV flight in a constrained urban environment," in *28th International Congress of the Aeronautical Sciences*, 2012.

[19] G. Heredia and A. Ollero, "Sensor fault detection in small autonomous helicpoters using observer/Kalman filter identification," in *Proceedings of the 2009 IEEE International Conference on Mechatronics*, Malaga, Spain, April 2009, pp. 1–6.

[20] P. Lu, L. Van Eykeren, E.-J. van Kampen, and Q. Chu, "Sensor fault detection and estimation for quadrotors using kinematic equations," in *Advances in Aerospace Guidance, Navigation and Control*, J. Bordeneuve-Guibé, A. Drouin, and C. Roos, Eds. Springer International Publishing, 2015, pp. 363–379.

[21] A. Tayebi and S. McGilvray, "Attitude stabilization of a VTOL quadrotor aircraft," *IEEE Transactions on Control Systems Technology*, vol. 14, no. 3, pp. 562–571, May 2006.

[22] T. Madani and A. Benallegue, "Control of a quadrotor mimi-helicopter via full state backsteeping technique," in *The 45th IEEE Conference on Decision and Control*, 2006, pp. 1515–1520.

[23] L. Wang and J. Su, "Robust disturbance rejection control for attitude tracking of an aircraft," *IEEE Transactions on Control Systems Technology*, vol. 23, no. 6, pp. 2361–2368, Nov 2015.

[24] T. Lee, "Robust adaptive attitude tracking on SO(3) with an application to a quadrotor UAV," *IEEE Transactions on Control Systems Technology*, vol. 21, no. 5, pp. 1924–1930, Sept 2013.

[25] K. P. B. Chandra, H. Alwi, and C. Edwards, "Fault reconstruction for a quadrotor using an LPV sliding mode observer," in *9th IFAC Symposium on Fault Detection, Supervision and Safety for Technical Processes SAFEPROCESS 2015*, vol. 48, no. 21, Paris, France, 2015, pp. 374–379.

[26] M. H. Amoozgar, A. Chamseddine, and Y. M. Zhang, "Experimental test of a two-stage Kalman filter for actuator fault detection and diagnosis of an unmanned quadrotor helicopter," *Journal of Intelligent & Robotic Systems*, vol. 70, no. 1, pp. 107–117, August 2013.

[27] Z. Cen, H. Noura, T. B. Susilo, and Y. A. Younes, "Robust fault diagnosis for quadrotor UAVs using adaptive Thau observer," *Journal of Intelligent Robotic Systems*, vol. 73, no. 1, pp. 573–588, January 2013.

[28] M. Saied, H. Shraim, C. Francis, I. Fantoni, and B. Lussier, "Actuator fault diagnosis in an octorotor UAV using sliding modes technique: Theory and experimentation," in *2015 European Control Conference (ECC)*, July 2015, pp. 1639–1644.

[29] Z. T. Dydek, A. M. Annaswamy, and E. Lavretsky, "Adaptive control of quadrotors UAVs: A design trade study with flight evaluations," *IEEE Transactions on Control Systems Technology*, vol. 21, no. 4, pp. 1400–1406, 2013.

[30] I. Sadeghzadeh, A. Mehta, Y. Zhang, and C.-A. Rabbath, "Fault-tolerant trajectory tracking control of a quadrotor helicopter using gain-scheduled PID and model reference adaptive control," in *Annual Conference of the Prognostics and Health Management Society*, Montreal, Quebec, Canada, 2011.

[31] Q. Shen, D. Wang, S. Zhu, and E. K. Poh, "Fault-tolerant attitude tracking control for quadrotor aircraft," in *53rd IEEE Conference on Decision and Control*, Los Angeles, CA, USA, 2015.

[32] P. Bourque and R. Dupuis, *Guide to the Software Engineering Body of Knowledge (SWEBOK)*. IEEE Computer Society, 2005.

[33] X. Zhang, M. Clark, K. Rattan, and J. Muse, "Controller verification in adaptive learning systems towards trusted autonomy," in *Proceedings of the ACM/IEEE Sixth International Conference on Cyber-Physical Systems*, ser. ICCPS '15. New York, NY, USA: ACM, 2015, pp. 31–40.

[34] P. Pounds, R. Mahony, and J. Gresham, "Towards dynamically-favourable quadrotor aerial robots," in *Australasian Conference on Robotics and Automation, ACRA*, 2004.

[35] A. Bramwell, G. Done, and D. Balmford, *Bramwell's Helicopter Dynamics*. Oxford: Butterworth-Heinemann, 2001.

[36] P. Castillo, R. Lozano, and A. Dzul, *Modelling and Control of Mini-Flying Machines*. Berlin: Springer-Verlag, 2005.

[37] M. Bangura and R. Mahony, "Nonlinear dynamic modelling for high performance control of a quadrotor," in *Proceedings of Austrasian Conference on Robotics and Automation*, 2012.

[38] X. Zhang, M. Polycarpou, and T. Parsini, "Robust fault isolation for a class of non-linear input-output systems," *International Journal Control*, vol. 74, no. 13, pp. 1295–1310, 2001.

[39] G. Bastin and M. Gevers, "Stable adaptive observers for non-linear time-varying systems," *IEEE Transaction on Automatic Control*, vol. 33, no. 7, pp. 650–658, 1988.

[40] B. Lantos and L. Marton, *Nonlinear Control of Vehicles and Robots.* Springer-London, 2011, ch. Nonlinear Control of Airplanes and Helicopters.

[41] R. C. Leishman, J. C. MacDonald, R. W. Beard, and T. McLain, "Quadrotors and accelerometers. State estimation with an improved dynamic model," *IEEE Control Systems Magazine*, vol. 34, no. 1, 2014.

[42] N. Guenard, T. Hamel, and R. Mahony, "A practical visual servo control for an unmanned aerial vehicle," *IEEE Transaction on Robotics*, vol. 24, no. 2, 2008.

[43] N. M. Barbour, "Inertial navigation sensors. NATO report," Draper Laboratory, Tech. Rep., 2013.

[44] X. Zhang, "Sensor bias fault detection and isolation in a class of nonlinear uncertain systems using adaptive estimation," *IEEE Transaction on Automatic Control*, vol. 56, no. 5, pp. 370–376, 2011.

[45] P. A. Ioannou and J. Sun, *Robust Adaptive Control.* Mineola, New York: Dover Publications, Inc., 1996.

[46] B. Anderson, R. Bitmead, C. R. Johnson, Jr, P. V. Kokotovic, R. L. Kosut, I. M. Y. Mareels, L. Praly, and B. D. Riedle, *Stability of Adaptive Systems: Passivity and Averaging Analysis.* Cambridge, Massachusettes: The MIT Press, 1986.

[47] F. Gustafsson, *Adaptive Filtering and Change Detection.* Wiley, West Sussex, England, 2000.

[48] C. Edwards and X.-G. Yan, "Nonlinear robust fault reconstruction and estimation using a sliding mode observer," *Automatica*, vol. 43, no. 9, pp. 1605–1614, September 2007.

[49] X. Zhang, M. M. Polycarpou, and T. Parisini, "A robust detection and isolation scheme for abrupt and incipient faults in nonlinear systems," *IEEE Transactions on Automatic Control*, pp. 576–593, 2002.

[50] R. Avram, X. Zhang, and J. Muse, "Quadrotor accelerometer and gyroscope sensor fault diagnosis with experimental results," in *Annual Conference of the Prognostics and Health Management Society*, vol. 8, San Diego, CA, 2015, pp. 625–623.

[51] V. I. Utkin, *Sliding Modes in Control and Optimization*. Springer Verlag, 1992.

[52] P. Martin and E. Salaün, "The true role of accelerometer feedback in quadrotor control," in *IEEE International Conference on Robotics and Automtation*, Anchorage, AK, 2010, pp. 1623–1629.

[53] L. Ascorti, "An application of the extended Kalman filter to the attitude control of a quadrotor," Politecnico di Milano, Tech. Rep., 2013.

[54] X. Zhang, M. Polycarpou, and T. Parisini, "A robust detection and isolation scheme for abrupt and incipient faults in nonlinear systems," *Automatic Control, IEEE Transactions on*, vol. 47, no. 4, pp. 576–593, Apr 2002.

[55] Z. Dydek, A. Annaswamy, and E. Lavretsky, "Adaptive control of quadrotor UAVs: A design trade study with flight evaluations," *IEEE Transactions on Control Systems Technology*, vol. 21, no. 4, pp. 1400–1406, July 2013.

[56] V. Klein and E. A. Morelli, *Aircraft System Identification: Theory and Practice*, 1st ed. American Institute of Aeronautics & Astronautics, Reston, VA, 2006.

[57] Wright State University UAV Laboratory. (2016) Real-time actuator fault diagnosis and accommodation for quadrotor UAVs. [Online]. Available: https://www.youtube.com/watch?v=Tk1d8hj0Hus

[58] A. Chamseddine, D. Theilliol, Y. Zhang, C. Join, and C. Rabbath, "Active fault-tolerant control system design with trajectory re-planning against actuator faults and saturation: Application to a quadrotor unmanned aerial vehicle," *International Journal of Adaptive Control and Signal Processing*, vol. 29, no. 1, pp. 1–23, 2015.

[59] M. Ranjbaran and K. Khorasani, "Fault recovery of an under-actuated quadrotor aerial vehicle," in *IEEE Conference on Decision and Control*, Dec 2010, pp. 4385–4392.

[60] R. Avram, X. Zhang, and J. Muse, "Quadrotor actuator fault diagnosis and accommodation using nonlinear adaptive estimators," *IEEE Transactions on Control Systems Technology*, submitted-2015.

[61] M. Krstic, I. Kanellakopoulos, and P. Kokotovic, *Nonlinear and Adaptive Control Design*. New York, NY: Wiley, 1995.

[62] J. A. Farrell and M. M. Polycarpou, *Adaptive Approximation Based Control: Unifying Neural, Fuzzy and Traditional Adaptive Approximation Approaches*. Wiley-Interscience, NJ, USA, 2006.

[63] Wright State University UAV Laboratory. (2016) Experimental demonstration of a real-time quad rotor fault-tolerant altitude and attitude controller. [Online]. Available: https://www.youtube.com/watch?v=Acz4ZZiq5ek&feature=youtu.be

[64] U. S. Air Force, *Technology Horizons: a Vision for Air Force Science and Technology during 2010-2030*. Maxwell AFB, AL: Air University Press, 2010.

[65] C. Wilkinson, J. Lynch, and R. Bharadwaj, "Final Report: Regulatory Considerations for Adaptive Systems," NASA, Tech. Rep. NASA/CR-2013-218010, June 2013.

[66] M. Aiello, J. F. Berryman, J. R. Grohs, and J. D. Schierman, "Run-time assurance for advanced fight-critical control systems," in *Proc. AIAA Guidance, Navigation, and Control Conference*, Toronto, Ontario, Canada, 2010.

[67] M. Clark, X. Koutsoukos, R. Kumar, I. Lee, G. Pappas, L. Pike, J. Porter, and O. Sokolsky, "A study on run time assurance for complex cyber physical systems," U.S. Air Force Research Laboratory, Tech. Rep. 88ABW-2013–1876, 2013.

[68] D. Seto, B. Krogh, L. Sha, and A. Chutinan, "The simplex architecture for safe on-line control system upgrades," in *Proc. 2008 American Control Conference*, Philadelphia, PA, 1998.

[69] Wright State University UAV Laboratory. (2016) Experimental validation of an adaptive control integrity monitoring algorithm for quadrotor UAVs. [Online]. Available: https://www.youtube.com/watch?v=V5v4ezbUJmc

[70] K. Hameed, R. Williams, and J. Smith, "Analytically redundant controllers for fault tolerance: Implementation with separation of concerns," in *American Control Conference (ACC), 2010*, June 2010, pp. 6216–6221.

[71] T. Kopfstedt, M. Mukai, M. Fujita, and C. Ament, "Control of formations of UAVs for surveillance and reconnaissance missions," in *Proceedings of the 17th World Congress. The International Federation of Automatic Control*, 2008, pp. 6–11.

[72] D. J. Pack, P. DeLima, G. J. Toussaint, and G. York, "Cooperative control of UAVs for localization of intermittently emitting mobile targets," *IEEE Transactions on Systems, Man, and Cybernetics, Part B (Cybernetics)*, vol. 39, no. 4, pp. 959–970, Aug 2009.

[73] A. Sivakumar and C. K.-Y. Tan, "UAV swarm coordination using cooperative control for establishing a wireless communications backbone," in *Proceedings of the 9th International Conference on Autonomous Agents and Multiagent Systems: Volume 3 - Volume 3*, ser. AAMAS '10. Richland, SC: International Foundation for Autonomous Agents and Multiagent Systems, 2010, pp. 1157–1164.